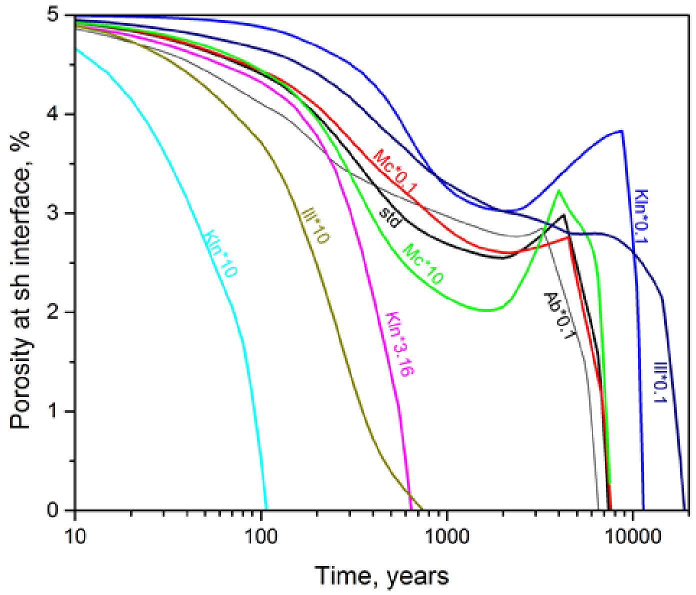

Predictive Modeling of CO_2 Sequestration and Storage in Deep Saline Sandstone Reservoirs: Sensitivity Analysis of Mineral Rates in Reactive Transport

---

21 March 2017

Office of Fossil Energy

NETL-TRS-5-2017

Disclaimer

Cover Illustration: Figure illustrating how changes in the mineral kinetic constants impact prediction of shale porosity evolution over time.

Suggested Citation: Balashov, V. N.; Brantley, S. L.; Guthrie, G. D.; Lopano, C. L.; Hakala, J. A.; Rimstidt, J. D. *Predictive Modeling of* CO_2 *Sequestration and Storage in Deep Saline Sandstone Reservoirs: Sensitivity Analysis of Mineral Rates in Reactive Transport*; NETL-TRS-5-2017; NETL Technical Report Series; U.S. Department of Energy, National Energy Technology Laboratory: Morgantown, WV, 2017; p 84.

Predictive Modeling of CO_2 Sequestration and Storage in Deep Saline Sandstone Reservoirs: Sensitivity Analysis of Mineral Rates in Reactive Transport

Victor N. Balashov[1], Susan L. Brantley[1], George D. Guthrie[2], Christina L. Lopano[2], J. Alexandra Hakala[2], J. Donald Rimstidt[3]

[1] Earth and Environmental Systems Institute, 2217 EES Building, Pennsylvania State University, University Park, PA 16802

[2] U.S. Department of Energy, National Energy and Technology Laboratory, 626 Cochrans Mill Road, Pittsburgh, PA 15236

[3] Department of Geosciences, Derring Hall, RM4044, Virginia Tech, 1405 Perry Street, Blacksburg, VA 24061

NETL-TRS-5-2017

21 March 2017

NETL Contacts:
Christina Lopano, Principal Investigator
Angela Goodman, Technical Portfolio Lead
Cynthia Powell, Executive Director, Research & Innovation Center

Table of Contents

This page intentionally left blank.

List of Figures

List of Figures (cont.)

List of Tables

Acronyms, Abbreviations, and Symbols

Term	Description
BDF	Backward differentiation formula
CO_2	Carbon dioxide
DAE	Differential/algebraic equations
IAF	Inverse Archie factor
LCE	Local chemical equilibrium
MSA	mean spherical approximation
PDE	Partial differential equations
REV	Representative elemental volume
SC	Supercritical
ss/sh	Sandstone/shale
STT	Standard termination time
Symbols	
a	year (365 days)
A_m	chemical affinity of reaction mineral/fluid
a_i	activity of i^{th} aqueous species in molal scale
α	coefficient in the Archie law
D	effective diffusion coefficient through porous medium (m^2s^{-1})
D_{aq}	diffusion coefficient in pore solution (m^2s^{-1})
$E_{H,m}$, $E_{W,m}$, and $E_{OH,m}$	three activation energies for dissolution by the acidic, neutral and basic mechanisms, respectively (J mol^{-1})
F_{inv}	inverse of the Archie formation factor
ϕ	rock porosity
ϕ_m	volume fraction of mineral *m*
γ_i	activity coefficient of i^{th} aqueous species for the 1 mol kg^{-1} molal standard state
I_m	reaction rate for m^{th} mineral (mol m^{-2} s^{-1})
k_m	kinetic constant for mineral m (mol m^{-2} s^{-1})

Acronyms, Abbreviations, Symbols (cont.)

Term	Description
k_{sand}	sandstone permeability (m^2)
K_G	number of electrically neutral Gibbs components of the system
MNL_m	m^{th} mineral
m_i	molality of i^{th} aqueous species
M_k	total molality of k^{th} independent component
N_m	number of minerals
N_{aq}	number of aqueous solutes
N_p	number of the primary aqueous species
N_s	number of secondary aqueous species
n_m	constant number of m^{th} mineral grains per unit volume of a porous medium (m^{-3})
η_{brine}	brine viscosity (Pa s)
PR_k	k^{th} primary species
$r_{m,n}$	radii of ion complexes and associates
ρ^*	mass of water per unit volume of aqueous solution (kg m^{-3})
SC_i	i^{th} secondary species
s_m	specific surface area of mineral m (m^2 m^{-3})
$\bar{S}_{CO_2,tot}$	dimensionless quantity of stored CO_2
V_m^0	molar volume of mineral m
v_c^D	Darcy velocity for convection
y_i	activity coefficient of i^{th} aqueous species for the 1 mol dm^{-3} standard state of MSA
$[CO_2]$	amount of stored CO_2 per m^3 of rock

Acknowledgments

This work was completed as part of National Energy Technology Laboratory (NETL) research for the U.S. Department of Energy's (DOE) Carbon Storage Program. The authors wish acknowledge Cindy Powell and Traci Rodosta (NETL Research & Innovation Center) as well as Angela Goodman (NETL Technical Portfolio Manager Carbon Storage) for guidance, direction, support, and for helpful discussions and presentation of our achievements.

This page intentionally left blank.

EXECUTIVE SUMMARY

One idea for mitigating the increase in fossil-fuel generated carbon dioxide (CO_2) in the atmosphere is to inject CO_2 into subsurface saline sandstone reservoirs, thereby storing it in those geologic formations and out of the atmosphere. To decide whether safe and effective geologic storage can be implemented at a globally significant scale will require the ability to reliably predict the fate of injected CO_2. Thus, models are needed to predict the rates and extents of subsurface rock-water-gas interactions related to dissolution and mineral trapping of injected CO_2, and to the geochemical alteration of storage reservoir and sealing-interval rock. Several reactive transport models for CO_2 sequestration created in the last decade predicted sequestration in sandstone reservoirs of ~17 to ~90 kg CO_2 m^{-3}. To build confidence in such models, a baseline problem including rock + water chemistry is proposed as the basis for future modeling so that both the models and the parameterizations can be compared systematically. In addition, a reactive diffusion model is used to investigate the fate of injected supercritical CO_2 fluid in the proposed baseline reservoir + brine system. In the baseline problem, injected CO_2 is redistributed from the supercritical (SC) free phase by dissolution into pore brine and by formation of carbonates in the sandstone. The numerical transport model incorporates a full kinetic description of mineral-water reactions under the assumption that transport is by diffusion only. Sensitivity tests were also run to understand which mineral kinetics reactions are important for CO_2 trapping.

A reactive diffusion model was expanded for use in an investigation of the reactions and transport of CO_2 and aqueous solutes during CO_2 injection into a subsurface geological reservoir. The simulation focused on the sandstone/shale (ss/sh) interface that represents the boundary between the storage interval and caprock seal. A series of reactive diffusion calculations was run to simulate reaction and transport of SC CO_2 in a hypothetical reservoir at the ss/sh interface at 348.15 K and 30 MPa for up to 20,000 years. During the first period (up to 2,000 years) the shale functioned as a low-permeable barrier (caprock), and the chemical reactions mostly occurred in the sandstone. However, at the ss/sh interface, the precipitation of microcline, kaolinite and dolomite were observed. In the second period (2,000–4,000 years), the CO_2 reactive transport begins to initiate the replacement of Mg-Fe chlorite by ankerite, dolomite, and illite at the ss/sh interface. In the third period (4,000–7,500 years), this carbonation reaction in the shale led to complete closure of the porosity at the interface, further sealing the reservoir and terminating further reaction.

The sensitivity of the reactive system to the mineral kinetic constants and to the shale transport properties (i.e., the Archie formation factor) was quantitatively determined and analyzed. It was found that the time sequence described above is extremely sensitive to the kinetic constants of clay minerals. For example, an increase in the kaolinite kinetic constant by 0.25 and 0.5 logarithmic units resulted in earlier porosity closure by 4,300 and 650 years, respectively. The modeling output is useful in understanding issues around the long-term effectiveness of CO_2 storage in sandstone reservoirs beneath shale caprock.

1. INTRODUCTION

Climate change is beginning to impact human systems on Earth. One of the most important boundary conditions on maintenance of the Earth system (Rockström et al., 2009) is the content of greenhouse gas carbon dioxide (CO_2) in the atmosphere. A potential solution to mitigate increases in atmospheric CO_2 is to capture CO_2 and inject it into deep geologic storage formations consisting of porous units capped by impermeable barriers.

CO_2 storage in deep saline reservoirs is one option for mitigation of CO_2 emissions, which are projected to reach 6,300 million metric tons of CO_2 equivalent by 2035 (NETL ATLAS, 2010). Deep saline reservoirs in the United States have been estimated by the U.S. Regional Carbon Sequestration Partnerships to provide the capacity for roughly 20,000 billion metric tons of CO_2 storage (NETL ATLAS, 2010). This storage volume is roughly two orders of magnitude greater than potential CO_2 storage in depleted oil and gas reservoirs. Thus, deep saline reservoirs are a primary long-term focus for geologic CO_2 storage in the U.S. In the near term, geological storage of CO_2 in conjunction with CO_2-enhanced oil recovery is increasingly being recognized as an important commercial option for CO_2 capture, utilization, and storage.

Geological CO_2 storage requires an ability to predict the behavior of the geologic system over both the near- and long-term. Near-term behavior includes changes that occur during injection and in the period post-closure when the storage system may be relatively more dynamic, while long-term behavior includes changes during the stewardship phase that lasts from decades to hundreds of years. Many aspects of CO_2 behavior during injection can be predicted based on historical experience from oil and gas operations, but many of the longer-term effects may require additional investigation. Furthermore, because storage lifetimes must exceed the duration of present-day field tests of CO_2 storage by orders of magnitude, conceptual and numerical models are needed that represent the important geochemical processes. Specifically, models are needed to understand whether injection will effectively sequester the CO_2 for time periods that are long enough to warrant the economic investment, to meet regulations, and to convince the public that storage reservoirs are safe.

Geochemical calculations are needed to predict reactions that range from dissolution of CO_2 in brines to precipitation of storage-reservoir minerals. Such calculations rely on thermodynamic and kinetic databases. There are many sources of uncertainty in data on mineral/fluid kinetics. First, there are experimental errors. Second, it is common to discover differences between reaction rates measured at the laboratory and field scales (White and Brantley, 2003). Often under experimental conditions the reactions take place at large fluid/rock ratios at the free fluid/mineral interface. In contrast, the same reactions take place in nature at the mineral/pore fluid interface at a small fluid/rock ratio. Consequently, reactions in rock porous media generally are closer to equilibrium in natural systems than in the laboratory. The kinetic mechanisms of these mineral/fluid reactions in natural systems can therefore be different (Arvidson and Lüttge, 2010). The next source of uncertainty is in upscaling from the pore-grain scale to the level of the representative elemental volume (REV) of the rock (Li et al., 2007; Kang et al., 2010). Uncertainty is also entailed in describing the reactive surface area of minerals (Rimstidt et al., 2012). Therefore, sensitivity tests must be run to understand how uncertainties in kinetic data, in mechanisms, in upscaling and in mineral active surface area affect model output. A better understanding of model variability induced by differences in kinetics is of importance to confidently predict CO_2 storage permanence.

A simple approach was applied to probe the impact of uncertainties in both kinetic constants and the Archie formation factor. A simple general kinetic law was used for mineral/fluid interaction supported by experimental kinetic constants to explore the uncertainties in mineral/fluid kinetics by systematically varying kinetic constants within ± 1 order of magnitude. The uncertainties of shale diffusivity were also evaluated by varying the Archie formation factor.

In the first part of the work (Balashov et al., 2013), a case study consisting of a baseline reservoir + brine is defined. Ninety percent of sequestration reservoirs in the U.S. are likely to be clastic (Wildgust et al., 2011). The temperature (T), pressure (P), mineralogy, and chemistry of the baseline reservoir were chosen to represent a rough average of the characteristics of sandstone-hosted reservoirs currently proposed in the U.S. for sequestration. Modeling the reactivity of a clastic reservoir is a particular challenge because of the variety of minerals that can be present.

In the second part of the work (Balashov et al., 2015) the earlier model was extended by incorporating the shale caprock into the model system. Porous sandstone reservoirs capped by shale constitute one important type of storage formation. This simulation required the addition of four new chemical components to the previously modelled sandstone system (i.e., MgO, FeO, O_2, H_2SO_4). This model allows us to simulate diffusion and chemical alteration at the interface of the sandstone/shale (ss/sh). Diffusion is the main transport process at the caprock interface because of the low porosity and high tortuosity of the shale.

The third part of this work begins to address the influence of organic matter on the system. This approach is to develop a simple model that incorporates acetic acid in the pore water in the shale.

2. METHODS

2.1 GEOPHYSICAL AND GEOCHEMICAL CONDITIONS

Mineral reactivity is strongly influenced by temperature, which affects solubility and reaction kinetics, and by the confining pressure, which determines the maximum CO_2 pressure attainable. If storage is targeted for depths below ~0.8 km, CO_2 will exist as a supercritical fluid and will, therefore, require less storage volume. Furthermore, as noted by Stauffer et al. (2009), changes in depth-related properties such as viscosity, density, and injection pressures may favor deeper wells both economically and with respect to risk. However, depth must also be considered in terms of drilling costs (Stauffer et al., 2009). Recognizing such trade-offs, it is assumed that reservoir storage depth will most likely be between 1 and 3 km. Given that the average continental geothermal gradient is ~25°C/km, temperatures will likely range between ~50 and 100°C. It might be reasonable to extend this temperature range up to 125°C because sediments are good insulators and the geothermal gradient in some sedimentary basins might be as high as 35°C/km. Thus, at 3 km depth, T = 130°C. Here, 2 km is chosen as a prototypical depth for the storage reservoir and a temperature of 75°C.

Solutions with a density near 1g/cm^3 are consistent with a hydrostatic pressure gradient of 10 MPa/km (100 bar/km). Likewise, sedimentary rocks with a density of ~2.3 g/cm^3 are consistent with a lithostatic pressure gradient of ~23 MPa/km. However, it is unlikely that storage reservoir pressures will exceed about 65% of lithostatic pressure because rock units tend to hydrofracture if pressurized above this value (Dickinson and Suczek, 1979). This bounds the envelope of CO_2 pressure that could be present in a storage reservoir by an upper limit of 14.5 MPa/km. The upper limit of P_{CO2} in a storage reservoir at a depth of 2 km, 30 MPa (Figure 1), is, therefore, chosen for the baseline model. Thus, temperature (T) and pressure (P) for the baseline sandstone reservoir were set for a system at a prototypical depth of 2 km (Balashov et al., 2013). Temperature, T was set at 75°C and pressure, P, at 30 MPa.

The saline pore fluids in sandstone reservoirs are typically dominated by NaCl with significant $CaCl_2$ and additional K_2SO_4 and $MgCl_2$. Values from the most comprehensive compilation of North American oil-field brine compositions were averaged to obtain the concentrations used for the modeled brine shown in Table 1 (Collins, 1975). In Table 1, N = the number of published analyses used to calculate the average.

Table 1: Average composition of North American oil field brines based on published compositions (Collins, 1975)

Species	mg/L	molality	N
Cl^-	74,803	2.1071	3397
Na^+	37,262	1.6201	3397
Ca^{2+}	7,858	0.1960	3392
Mg^{2+}	1,514	0.0623	3364
SO_4^{2-}	535	0.0056	2673
K^+	519	0.0132	429
HCO_3^-	246	0.0040	3143

N = the number of published analyses used to calculate the average

2.2 MINERALOGY, THERMODYNAMICS, AND KINETICS

In the first part of this work (Balashov et al., 2013) the chemistry and mineralogy was restricted to the eight-component system, SiO_2-Al_2O_3-CaO-Na_2O-K_2O-HCl-CO_2-H_2O and a relatively simple baseline mineralogy (Table 2). To choose the mineralogy, sandstones derived from continental block lithologies were emphasized to avoid complications associated with lithic fragments (Dickinson and Suczek, 1979). The feldspar content of such sandstones has been observed to range up to 50% (Dickinson and Suczek, 1979). The baseline sandstone was, therefore, assumed to contain a total feldspar content of 26% (18% K-feldspar, 8% plagioclase). These values are higher than the previously reported average value of 15% for sandstones (Pettijohn et al., 1987). However, the higher feldspar value is not dissimilar from many observed values. Although plagioclase compositions vary up to An_{70} (Trevena and Nash, 1979), an average value of An_{20} (oligoclase) was chosen because oligoclase is the most common feldspar mineral in surface systems. The average feldspar grain diameter was set to 0.125 mm based on published results (Odom, 1976). Geometric specific surface areas were assumed for all minerals. Based upon these considerations, the baseline sandstone was set to the mineralogy summarized in Table 2.

In the second part (Balashov et al., 2015), the 12-component system was extended to, SiO_2-Al_2O_3-CaO-MgO-FeO-Na_2O-K_2O-HCl-H_2SO_4-CO_2-O_2-H_2O. A relatively simple baseline ss/sh mineralogy was chosen (Table 2). The shale mineralogy (Hosterman and Whitlow, 1983) was chosen to be close to that of a black shale like that of the Marcellus formation (Table 2), which is of interest for shale gas research, but is also considered a secondary caprock for the Oriskany formation (a formation under consideration for geologic storage of CO_2; Kostelnik and Carter, 2009).

The apparent Gibbs free energies of minerals and aqueous species are represented in Table 3. These data were compiled from published data (Holland and Powell, 1998, 2011) for the minerals, and from Supcrt92 (Johnson et al., 1992) and another compilation (Pokrovskii and Helgeson, 1995) for the aqueous species. The smectite and chlorite Gibbs free energies of formation from elements was calculated through the sum of polyhedral contributions by a published method (Chermak and Rimstidt, 1989, 1990a).

The water density, dielectric constant and compressibility are from published values (Wagner and Pruss, 2002). The viscosity is derived also from published values (Sengers and Watson, 1986), as is the ionization constant (Johnson et al., 1992).

Table 2: Mineral compositions of sandstone and shale

Minerals	Formula	Sandstone		Marcellus Shale: Chevron	
		mass %	volume %	mass %	volume %
Primary					
Quartz	SiO_2	65	48.75	38	38.41
Microcline	$KAlSi_3O_8$	18	13.5	2	2.10
Oligoclase	$Ca_{0.2}Na_{0.8}Al_{1.2}Si_{2.8}O_8$	8	6	0	0
Calcite	$CaCO_3$	5	3.75	5	4.93
Smectite[a]	$K_{0.03}Ca_{0.39}Al_{1.77}Si_{3.97}O_{10}(OH)_2$	3	2.25	0	0
Smectite	$K_{0.05}Ca_{0.5}Al_{2.8}(Fe_{0.5}Mg_{0.7})Si_{7.65}Al_{0.35}O_{20}(OH)_4$	3	2.25	0	0
Illite (+mica)	$KAl_3Si_3O_{10}(OH)_2$	1	0.75	35	33.13
Pyrite	FeS_2	0	0	5	2.67
Chlorite	$Mg_{2.7}Fe_{1.8}Fe^{III}_{0.12}Al_{1.38}[Al_{1.5}Si_{2.5}O_{10}(OH)_8]$[b]	0	0	15	13.76
Porosity	volume %	25		5	
Secondary minerals that may form					
Albite	$NaAlSi_3O_8$	0		0	
Kaolinite	$Al_2Si_2O_5(OH)_4$	0		0	
Ankerite	$CaFe_{0.6}Mg_{0.4}(CO_3)_2$	0		0	
Siderite	$FeCO_3$	0		0	
Dolomite	$CaMg(CO_3)_2$	0		0	
Goethite	$FeOOH$	0		0	
Magnetite	Fe_3O_4	0		0	
[a] Smectite composition for baseline sandstone					
[b] Lowson et al. (2005)					

Table 3: Thermodynamic parameters of minerals and aqueous species at T = 75°C (348.15 K) and P = 30 MPa

Chemical Entity	$G^0_{348\ K}$ / kJ mole$^{-1\ a}$	$V^0_{348\ K}$ / cm^3 mole$^{-1\ b}$	Ionic radii /Å of Aqueous Species
Quartz [c]	-857.81	22.688	NA
Albite	-3720.27	100.06	NA
Microcline	-3758.57	108.92	NA
Oligoclase, An_{20} [d]	-3779.43	100.206	NA
Calcite	-1133.05	36.89	NA
Smectite [e, j]	-5361.55	140.	NA
Smectite [e]	-10585.	280.	NA
Illite	-5615.43	140.83	NA
Kaolinite	-3809.86	99.34	NA
Pyrite	-162.41	23.94	NA
MgFe-chlorite [e]	-7770.	211.4	NA
Dolomite	-2169.76	64.34	NA
Ankerite	-1966.36	65.37	NA
Siderite	-692.62	29.43	NA
Magnetite	-1018.36	44.52	NA
Goethite	-498.42	20.82	NA
SC CO_2 [f]	-391.12	57.908	NA
H^+	0	0	1.40
$O_{2(aq)}$	11.222	33.2	1.40
Na^+	-264.96	1.1	0.95
K^+	-287.25	10.7	1.33
Mg^{++}	-447.705	-21.	0.65
Ca^{++}	-550.38	-16.6	0.99
Fe^{++}	-86.801	-21.8	0.75
$Al(OH)_{3(aq)}$ [g]	-1107.47	14.6	2.03
$SiO_{2(aq)}$	-836.03	13.7	2.23
$SO_4^=$	-744.053	15.7	2.30
Cl-	-133.168	17.3	1.81
$CO_{2(aq)}$	-391.69	34.3	1.87
H_2O	-240.429	18.24	NA

Table 3: Thermodynamic parameters of minerals and aqueous species at T = 75ºC (348.15 K) and P = 30 MPa (continued)

Chemical Entity	$G^{0}_{348\ K}$ / kJ mole^{-1} [a]	$V^{0}_{348\ K}$ / cm^3 mole^{-1} [b]	Ionic radii /Å of Aqueous Species
OH^-	-156.42	-3.2	1.40
$H_{2(aq)}$	15.033	26.9	1.40
H_3SiO_4-	-1255.55	10.2	2.23
$NaCl_{(aq)}$	-393.97	25.7	1.89
$KCl_{(aq)}$	-412.72	38.5	2.02
$MgCl^+$	-580.81	2.1	1.84
$CaCl^+$	-679.95	6.3	1.90
$CaCl_{2(aq)}$	-812.49	33.4	2.34
$FeCl_{2(aq)}$	-338.85	28.2	2.31
Fe^{+++}	-4.234	-43.4	0.60
$NaOH_{(aq)}$ [g]	-416.38	2	1.53
$KOH_{(aq)}$ [g]	-440.16	15.8	1.72
Al^{+++} [g]	-471.64	-45.7	0.50
$Al(OH)^{++}$ [g]	-687.57	-18.7	1.42
$Al(OH)_2^+$ [g]	-898.36	7.1	1.78
$Al(OH)_4^-$ [g]	-1310.29	11.3	2.23
HCO_3^-	-590.99	26.	1.56
$CO_3^{=}$	-524.70	-6.3	1.85
HSO_4^- [h]	-761.98	35.5	2.46
$NaHSO_{4(aq)}$ [h]	-1029.59	40.	2.51
$Na_2SO_{4(aq)}$ [h]	-1286.52	40.	2.40
$NaSO_4^-$ [h]	-1015.75	30.	2.35
$K_2SO_{4(aq)}$ [i]	-1315.31	40.	2.56
KSO_4^- [i]	-1037.79	29.2	2.44

[a] Apparent standard Gibbs free energy
[b] Standard molar volume
[c] SUPCRT92
[d] Calculated by Holland and Powell (1992) model #1
[e] Calculated by Chermak and Rimstidt (1990a) algorithm
[f] Duan and Sun (2003)
[g] Pokrovskii and Helgeson (1995)
[h] Gibbs apparent free energy Hnedkovsky et al. (2005)
[i] Gibbs apparent free energy Sharygin et al. (2006)
[j] Smectite for the baseline sandstone

The mean spherical approximation (MSA) was used (Blum and Høye, 1977) to calculate activity coefficients in aqueous brine solution with dissolved CO_2. The MSA equation is more accurate than the Debye–Hückel equation because it is consistent with both the Debye–Hückel limiting law at low concentrations and the correct hard sphere ion repulsion model in very concentrated solution. The extended Debye–Hückel equation was not used for concentrated electrolyte solutions because it requires the special adjustment of two empirical parameters for the ion size and ion-ion interaction (Oelkers and Helgeson, 1990; Helgeson et al., 1981).

The activity coefficients for the 1 mol dm^{-3} standard state of MSA can be expressed in the form of electrostatic (el) and hard sphere (hs) contributions

$$\ln y_i = \ln y_i^{el} + \ln y_i^{hs} \tag{1}$$

The MSA expressions (Blum and Høye, 1977) for the electrostatic and hard sphere parts were previously discussed (Sharygin et al., 2002). The practice of MSA for electrolyte solutions (Sharygin et al., 2002, 2006; Hnedkovsky et al., 2005) showed that a good choice for the hard sphere ionic radii is to use the crystallographic radii (Marcus, 1985) in the equations so that there are no adjustable parameters. The radii of ion complexes and associates $A_m B_n$ were calculated (Table 3) as

$$r_{m,n} = \sqrt[3]{m r_A^3 + n r_B^3} \tag{2}$$

where r_a are the crystallographic radii of the corresponding ions. The MSA activity coefficients were calculated for an aqueous solution of average brine composition (Table 1), with the addition of dissolved 0.74 mol kg^{-1} CO_2. These activity coefficients have been used in all the reactive diffusion transport calculations as constant values.

The rate laws describing mineral dissolution/precipitation (Equation 15) were formulated following a published approach (Marini, 2007; Palandri and Kharaka, 2004; Lowson et al., 2005, 2007; Brantley, 2008; Köhler et al., 2003). The kinetic function for mineral m is expressed as the sum of three contributions

$$k_m = k_{H,m} + k_{W,m} + k_{OH,m} \tag{3}$$

where

$$k_{H,m} = a_{H^+}^{n_{H,m}} A_{H,m} \exp\left(-\frac{E_{H,m}}{RT}\right) \tag{4}$$

$$k_{W,m} = A_{W,m} \exp\left(-\frac{E_{W,m}}{RT}\right) \tag{5}$$

$$k_{OH,m} = (b_{H,m} a_{H^+}^{n_{OH,m}} + b_{OH,m} a_{OH^-}^{n_{OH,m}}) A_{OH,m} \exp\left(-\frac{E_{OH,m}}{RT}\right) \tag{6}$$

This approach relies on the use of three activation energies $E_{H,m}$, $E_{W,m}$, and $E_{OH,m}$ for dissolution by the acidic, neutral and basic mechanisms, respectively. In some cases (Palandri and Kharaka, 2004), the basic mechanism is expressed using the term $a_{H^+}^{n_{OH}}$, while in other cases (Brantley, 2008; Köhler et al., 2003) by the term $a_{OH^-}^{n_{OH}}$. For this reason, in Equation 6 the coefficients b_H and b_{OH} (which equal 0 or 1) have been introduced. In other words, either term can be used (but not both) depending upon how the original authors parameterized their model. The parameters used in Equations 3–6 for the model are represented in Table 4. These kinetic constants were varied over suitable ranges in sensitivity tests to assess how the uncertainties in kinetics affected the CO_2 storage in sandstone under shale capstone.

Table 4: Dissolution rate parameters for minerals[1]

Mineral		**Acidic Mechanism**			**Neutral Mechanism**			**Basic Mechanism**		
	E_H	A_H	n_H	E_W	A_W	E_{OH}	A_{OH}	n_{OH}	b_H	b_{OH}
	kJ mol^{-1}	mol $m^{-2}s^{-1}$		kJ mol^{-1}	mol $m^{-2}s^{-1}$	kJ mol^{-1}	mol $m^{-2}s^{-1}$			
Quartz	-	-	-	87.6	22.91	108.37	10	-0.5	1	0
Albite	65	33.11	0.46	69.8	1.55	71	2.88×10^{-5}	-0.572	1	0
Microcline	51.7	0.1	0.5	38	1.78×10^{-6}	94.1	1.95×10^{-5}	-0.823	1	0
Oligoclase	65	52.48	0.46	69.8	2.45	-	-	-	-	-
Calcite	14.4	165.96	1	23.5	0.02	-	-	-	-	-
Smectite	23.6	1.41×10^{-7}	0.34	35	2.24×10^{-7}	58.9	6.31×10^{-7}	-0.4	1	0
Illite[2]	46	2.2×10^{-4}	0.6	14	2.5×10^{-13}	67	0.27	0.6	0	1
Kaolinite	65.9	1.74	0.78	22.2	5.13×10^{-10}	17.9	1.23×10^{-14}	-0.472	1	0
Chlorite[3]	60	5.27	0.49	60	3.25×10^{-3}	60	5.27×10^{-7}	-0.43	1	0
Dolomite	36.1	1.36×10^{3}	0.5	52.2	4.12×10^{1}	-	-	-	-	-
Ankerite[4]	36.1	1.36×10^{3}	0.5	52.2	4.12×10^{1}	-	-	-	-	-
Siderite[5]	14.4	1.39×10^{-4}	1	23.5	5.98×10^{-6}	-	-	-	-	-
Magnetite	18.6	4.66×10^{-6}	0.28	18.6	3.01×10^{-8}	-	-	-	-	-
Goethite	-	-	-	86.5	1.64×10^{7}	-	-	-	-	-
SC CO_2[6]	-	-	-	-	2×10^{-2}	-	-	-	-	-

[1] If it is not shown otherwise all data from Palandri and Kharaka (2004)
[2] Köhler et al. (2003)
[3] Lowson et al. (2005, 2007)
[4] The accepted parameters are identical to dolomite (Palandri and Kharaka, 2004)
[5] The accepted parameters are identical to magnesite (Palandri and Kharaka, 2004)
[6] On the basis of Shindo et al. (1995)

The baseline model presented in the first part of this work was designed to simulate the most important geochemical reactions that will occur in a deep saline CO_2 reservoir. However, the simplicity and power of the model comes at the cost of ignoring less abundant minerals. Under assumption of the activation energy for all the dissolution reactions is 65 kJ/mol, reducing the temperature to 50°C will lower the reaction rates by about 0.75 log units. Raising the temperature to 100°C will increase the reaction rates by about 0.65 log units and raising the temperature to 125°C will increase the reaction rates by about 1.22 log units over the 75°C rates.

In the case of chlorite, the 25°C data was used as standard (Lowson et al., 2005) for iron-rich chlorite. The activation energy of iron-rich chlorite dissolution was estimated as 60 kJ mol^{-1} (Table 4) on the basis of data (Lowson et al., 2007) for the temperature range 25–95°C. The recent data for dissolution of magnesium-rich chlorite (Black and Haese, 2014) from 50 to 120°C and 120 to 200 bar CO_2 demonstrated a lower apparent activation energy of 16 ± 0.5 kJ mol^{-1}. This new activation energy results in a decrease in the chlorite kinetic constant by one order of magnitude at 75°C in comparison with its "standard" value (Table 4). However, the test simulation of reaction + diffusion at the ss/sh contact showed that a decrease in the chlorite kinetic constant by a factor of 10 does not change the model results to a significant extent because chlorite remains close to local equilibrium (see below).

Accurate kinetic laws for pyrite dissolution could be formulated as functions of pH and the activities of aqueous ferric ion and dissolved oxygen (Rimstidt and Newcomb, 1993; McKibben and Barnes, 1986; Williamson and Rimstidt, 1994). The calculations showed that under the conditions used in the simulations, these activities were always too small (Table 5) to produce significant pyrite dissolution even though the brine in the shale was always undersaturated with respect to pyrite. On this basis, the pyrite was treated in the simulation as an inert mineral.

Dawsonite was not included in this model (Balashov et al., 2013). Many studies in the past have predicted the formation of dawsonite at CO_2 sequestration conditions; however, as discussed in more detail previously (Kaszuba et al., 2011), dawsonite has rarely been found as a precipitate in natural analog sites or in laboratory studies. In addition, researchers have noted that the largely undetermined growth and nucleation parameters for dawsonite (Pham et al., 2011) result in much of the uncertainty in model simulations related to dawsonite. Given the on-going debate as to whether or not to include dawsonite in modeling of CO_2 storage systems, it was decided to not include it in the secondary mineral assemblage.

2.3 REACTIVE TRANSPORT MODELING

The fluid phase is water that contains N_{aq} aqueous solutes. The master variables of the problem are the N_p molalities of the primary (independent) aqueous species, plus N_m mineral volume fractions and porosity. Thus, there are $N_p + N_m + 1$ variables. The independent chemical components of the system are identical to the primary species. It is assumed that homogeneous aqueous reactions are fast and chemical equilibrium is, therefore, maintained in solution. The secondary species (SC_i) are generated from primary species (PR_k) from mass balance and mass action equations.

For the description of reactive transport equations for porous media a published notation was followed (Lichtner, 1996). Implicitly, the choice of primary (p) and secondary (s) species maintains charge balance; thus,

$$\begin{aligned} N_p &= K_G + 1 \\ N_s &= N_{aq} - N_p \end{aligned} \qquad (7)$$

Here, K_G is the number of electrically neutral Gibbs components of the system, and N_s is the number of secondary species in aqueous pore solution. The mass balance reaction for the secondary species are written in the set of reactions

$$\begin{gathered} SC_i \rightleftarrows \sum_{k=1}^{k=N_p} v_{ik}^{aq} PR_k\,, \\ i = 1, 2, \ldots, N_s \end{gathered} \qquad (8)$$

The activities of secondary species are determined by the chemical equilibria (8) as

$$\begin{aligned} &\ln a_{i,s} = \sum_{k=1}^{k=N_p} v_{ik}^{aq} \ln a_{k,p} - \ln K_i^{aq} \\ &i = 1, 2, \ldots, N_s \end{aligned} \qquad (9)$$

where K_i^{aq} are thermodynamic equilibrium constants for reactions in (8), p stands for primary species, and s for secondary. The activities of aqueous species are determined from their molalities by

$$\begin{aligned} &a_{i,\alpha} = \gamma_{i,\alpha} m_{i,\alpha} \\ &\alpha = p, s;\ i = 1, 2, \ldots, N_\alpha \end{aligned} \qquad (10)$$

where $\gamma_{i,\alpha}$ are activity coefficients.

The total molalities M_k of the independent components are determined by equations

$$\begin{aligned} &\mathrm{M}_k = m_k + \sum_{i=1}^{i=N_s} v_{ki}^{aqT} m_i \\ &k = 1, 2, \ldots, N_p \end{aligned} \qquad (11)$$

The equations of reactive mass transfer for independent components take the form

$$\begin{aligned} &\rho^* \phi \frac{\partial \mathrm{M}_k}{\partial t} = \rho^* \frac{\partial}{\partial x}\left(D \frac{\partial \mathrm{M}_k}{\partial x} \right) + \sum_{m=1}^{m=N_m} v_{km}^{mT} I_m \\ &k = 1, 2, \ldots, N_p \end{aligned} \qquad (12)$$

where ρ^* is the mass of water per unit volume of aqueous solution (kg m^{-3}). In addition, the equations for the volume fractions of minerals are

$$\frac{1}{V_m^0}\frac{\partial \phi_m}{\partial t} = -I_m \tag{13}$$

where V_m^0 is the molar volume of mineral *m*.

I_m is the reaction rate of mineral MNL_m (the rate is written as positive for mineral dissolution),

$$MNL_m \rightleftarrows \textstyle\sum_{k=1}^{k-N_p} v_{mk}^m PR_k$$

$$m = 1, 2, \ldots, N_m \tag{14}$$

The rate I_m of a heterogeneous reaction is written following transition state theory according to the following equation which has been reviewed many times in the literature (e.g., Brantley, 2008):

$$\begin{aligned} &I_m = s_m k_m (a_{aq}; \exp(-E_{A,m} / RT))(1 - \exp(-A_m / RT)) \\ &m = 1, 2, \ldots, N_m \end{aligned} \tag{15}$$

In this equation s_m is the specific surface area of mineral *m (*$m^2\ m^{-3}$). A_m in Equation 15 is the chemical affinity of Reaction 14 which is included so that rate Law 15 describes mineral dissolution if $A_m > 0$ and mineral precipitation if $A_m < 0$. The reaction kinetic constant k_m is written as $k_m(a_{aq}; \exp(-E_{A,m}/RT))$ because it is a function of a_{aq}, the activity of any species influencing the rate, and $E_{A,m}$, the activation energy of the reaction.

Variable surface areas were calculated assuming a uniform fine-grained rock medium. It was calculated per unit volume of rock as

$$s_m = 6 n_m^{1/3} \phi_m^{2/3} \tag{16}$$

where n_m (m^{-3}) is the constant number of mineral grains per unit volume of a porous medium (Table 5) and ϕ_m is the mineral volume fraction. Taking into account that average mineral grain diameter, $d_{g,m}$, is expressed as $d_{g,m} = \left(\frac{\phi_m}{n_m}\right)^{1/3}$, the last Equation 16 can be rewritten as a function of grain diameter

$$s_m = 6 n_m \left(\frac{\phi_m}{n_m}\right)^{2/3} = 6 n_m \left(d_{g,m}\right)^2 \tag{17}$$

Equation 16 was used under the assumption that the concentration of mineral grains (n_m) is constant. This constant n_m was defined by assuming an average mineral grain size for the mineral volume fraction (Table 5).

Table 5: Mineral grain sizes at a given volume fractions and mineral specific surface areas

Mineral	Vol.% (100 φ_m)	Size (mm)	SSA_{geom}[a] (m^2/g)	n_m [b] (m^{-3})
Quartz	48.75[c]	1.00	2.3×10^{-3}	4.9×10^{8}
Albite	10.00	0.125	1.8×10^{-2}	5.1×10^{10}
Microcline	13.50[c]	0.125	1.9×10^{-2}	6.9×10^{10}
Oligoclase	6.00[c]	0.125	1.8×10^{-2}	3.1×10^{10}
Calcite	3.75[c]	0.500	4.4×10^{-3}	3×10^{8}
Smectite	2.25[c]	0.001	2.23	2.3×10^{16}
Illite	0.75[c]	0.001	2.12	7.5×10^{15}
Kaolinite	1.00	0.001	2.31	10^{16}
Chlorite	13.76[d]	0.008	2.6×10^{-1}	2.6×10^{14}
Dolomite	1.00	0.5	4.2×10^{-3}	8×10^{7}
Ankerite	1.00	0.5	4.2×10^{-3}	8×10^{7}
Siderite	1.00	0.5	3.0×10^{-3}	8×10^{7}
Magnetite	1.00	0.1	1.2×10^{-2}	10^{10}
Goethite	1.00	0.06	2.3×10^{-2}	5.2×10^{10}
SC CO_2	5.00[c]	0.01	7.9×10^{-1}	5×10^{13}

[a] Geometric surface area per gram of mineral

[b] Number of mineral grains per unit volume of porous medium

[c] Initial volume fraction in sandstone

[d] Initial volume fraction in shale

The average grain size varies with time. To initiate the appearance of a mineral which was not originally present in the system it was pre-seeded by a 1 ppm volume fraction. To use Equation 16 for mineral volume fractions less than 10^{-6} (i.e. to solve the problem of mineral *m* appearance/disappearance), Equation 16 was modified as

$$s_m = 6 n_m^{1/3} \phi_m^{1-SF(\phi_m^*;\phi_m)} \phi_m^{2/3} \tag{18}$$

where $SF(\phi_m^*;\phi_m)$ refers to Heaviside step-function of ϕ_m at $\phi_m^* = 10^{-6}$. Step-function is defined by relation: at $\phi_m \geq \phi_m^*$, $SF(\phi_m^*;\phi_m) = 1$; at $\phi_m < \phi_m^*$, $SF(\phi_m^*;\phi_m) = 0$.

The system of partial differential equations (PDE), Equations 12 and 13, as formulated in the main text along with the initial and boundary conditions was solved by the Method of Lines in the program MK76. In MK76, the PDE system was discretized (Lebedeva et al., 2007) by means of spatial finite differences and integrated in time by the implicit method for differential/algebraic equations (DAE) using the k^{th}-order backward differentiation formula (BDF) method. In that method k ranges from one to five to optimize the time stepsize and to maximize the accuracy of computations (Petzold, 1982; Brenan et al., 1995). The number of equidistant spatial nodes of discretization was set equal to 601.

3. SIMULATION OF CO_2 INDUCED REACTIVE PROCESS IN BASELINE SANDSTONE

3.1 SETUP OF THE REACTIVE DIFFUSION PROBLEM

The reactive diffusion process was investigated because it is the slowest of all transport processes. Thus, if the kinetics of mineral reactions are important during reactive diffusion, kinetics will also be important for a system with advective transport (for example, convection due to variable brine density). The general setup of the reactive diffusion model is represented in Figure 1. The content of water in the supercritical CO_2 (SC CO_2) phase was assumed to be negligible. Specifically, at 75°C and 30 MPa, the CO_2 fluid is calculated to contain ~0.6 mass % H_2O at equilibrium with the brine (Duan and Sun, 2003). The solubilities of minerals in this SC CO_2 phase are extremely low. Therefore, the transfer of H_2O, rock, and salt components through interface (A) was disregarded and only diffusion of CO_2 was allowed.

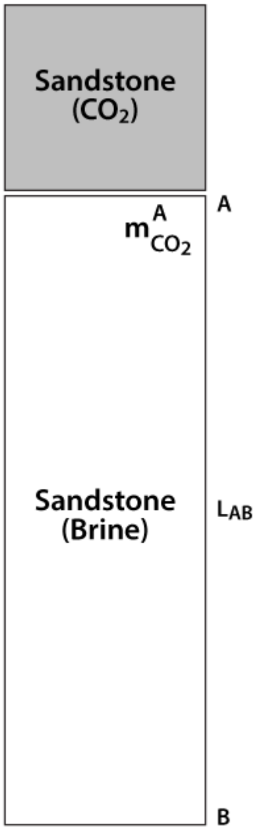

Figure 1: Schematic diagram of the one-dimensional reactive diffusion model. Upon initiation of the simulation, the sandstone contains a brine of composition shown in Table 2. A represents the interface between the CO_2 SC fluid and the brine, and is impermeable to salt. B represents the no-flow boundary. Models were run as described in text with different values for the distance between A and B (LAB). The system diagrammed here is a small piece of the entire plume-rock system as shown in Figure 2.

Although the buoyancy of SC CO_2 and its small viscosity will generate a highly dynamic response that includes convection, these are not included in the model. The focus instead is on simulating reactive diffusion which must occur in every situation at certain boundaries as shown in Figure 2. The model, therefore, simulates an element common to all CO_2-injected systems and allows focus on the importance of the kinetics of fluid-rock interactions.

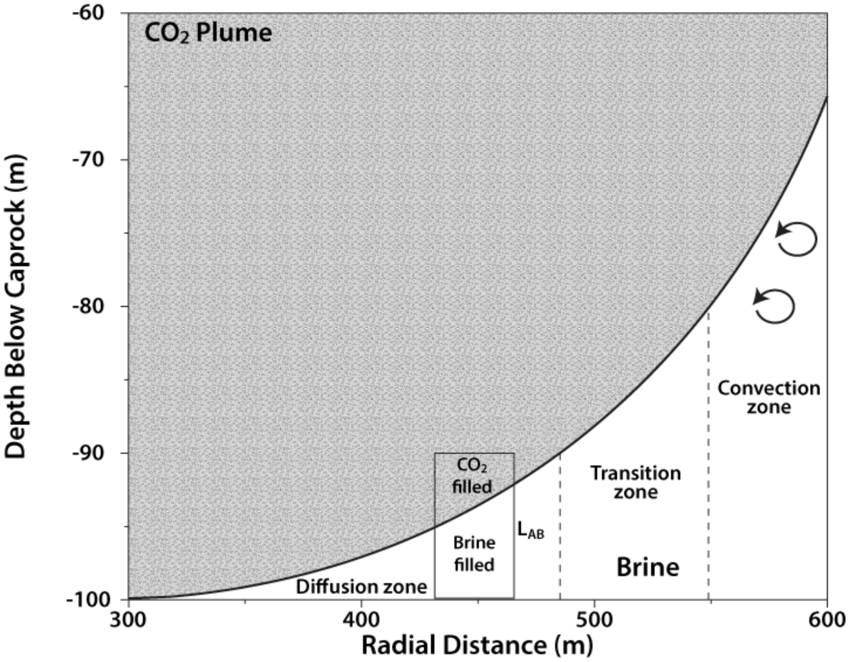

Figure 2: A schematic diagram of relative depth showing geometry of a CO_2 plume within a sandstone sandwiched between two shales. The overlying shale caprock is located at a depth of 0 in the diagram; the lower-lying shale lies at a depth of -100 m. The interface between the plume (grey) and the brine (white) within the sandstone forms a curved interface, as shown, relatively soon after injection. The rectangular box is the system of study, expanded in Figure 3: LAB is the distance from the underlying shale (depth = -100 m) to the CO_2 plume-brine interface. Figure redrawn following Figure 5.7 in Benson and Cook (2005).

In general, it is assumed that CO_2 will be injected into a horizontal layer of sandstone sandwiched between two layers of low-permeability shale (Benson and Cook, 2005). After injection, the supercritical CO_2 plume will be stabilized physically, forming a plume entirely within the sandstone. Computations show that under favorable conditions, such immobilization of SC CO_2 can occur within 25 a (year, 365 days) of CO_2 injection (Doughty, 2010). The immobilized SC CO_2 is mostly residually trapped, filling relatively disconnected clusters of pores. In principle, under these conditions the plume consists of a heterogeneous region comprised of pores containing the two immiscible phases, SC CO_2 and CO_2–saturated brine. The filling of the pores might have a complex geometry. For example, aqueous and CO_2 fluids will coexist within neighboring pores or even within the same pores in a homogeneous porous medium (Liu et al., 2010; Lu et al., 2009). The details and special features of this heterogeneous region with complex geometry were neglected in the model.

The plume is likely to be shaped somewhat like a funnel with its stem at the injection well within the sandstone reservoir (Benson and Cook, 2005; Lu et al., 2009; Dentz and Tartakovsky, 2009). The plume widens upward to its truncation at the upper caprock. Within the upper part of the plume, the CO_2 diffuses into the shale caprock (Gaus et al., 2005), but this process is not modeled here. At the bottom of the plume, CO_2 diffuses into the brine-saturated sandstone as represented in Figure 4, a schematic which was redrawn after Figure 5.7 (Benson and Cook, 2005). Interface (*A*) in Figure 3 defines the sub-horizontal interface of the plume at time 0 between the supercritical CO_2 fluid and the aqueous brine in the sandstone. Interface *A* is positioned at some distance L_{AB} from the impermeable shale, located at subhorizontal interface *B* (Figure 3).

The reactive diffusion of CO_2 down into the brine will change brine density and promote convection (Ennis-King and Paterson, 2007). The onset of convection is defined by the Peclet number which describes the balance between diffusion and convection,

$$Pe = \frac{v_c^D L_{AB}}{D} \tag{19}$$

where v_c^D is Darcy velocity for convection, D is the effective diffusion coefficient through porous sandstone, $D = 6\ 10^{-10}$ m^2 s^{-1}, and L_{AB} is the vertical distance from the plume bottom to the lower shale layer (Figure 2). v_c^D is determined by

$$v_c^D = \frac{k_{sand}\Delta\rho g}{\eta_{brine}} \tag{20}$$

where k_{sand} is sandstone permeability (10^{-15}–10^{-13} m^2), estimated as 10^{-14} m^2; $\Delta\rho$ (kg m^{-3}) is the brine density increment, $\Delta\rho \propto 0.1$ kg m^{-3}, g is acceleration due to gravity, g=9.8 m s^{-2}, and the brine viscosity, $\eta_{brine} = 5.2\ 10^{-4}$ Pa s.

Using these data and L_{AB}= 30 m, from Equation 19 it is calculated that $Pe = 0.93 \approx 1$; and at L_{AB} = 10 m, $Pe = 0.31 < 1$. On the basis of this estimation, the lower part of the sandstone which is saturated by brine (see Figure 4) can be thought of as divided into three regions controlled by different transport mechanisms: diffusion, diffusion + convection (labeled in Figure 4 as the transition zone), and convection. In this paper the zone dominated by diffusion is modeled. Again, the rationale for the focus on diffusion is to be able to determine the importance of the kinetics of fluid-rock interactions. It is likely that reactions that are kinetically limited in the simulation are also kinetically limited in systems that have advective as well as diffusive transport.

3.2 MODELING RESULTS ASSUMING STANDARD KINETICS

In discussing the results of the diffusion-reaction calculation, the solution for the problem in Figure 3 with L_{AB} = 3 m is first discussed. Interface A (Figure 3) was closed for all components except CO_2. The concentration of CO_2 at the boundary was maintained at a constant dissolved $CO_{2,aq}$ value set close to the equilibrium value determined for the supercritical CO_2 phase at 75°C and 30 MPa ($m^A_{CO2,aq}$= 0.65 mole kg^{-1}). The lower sandstone–shale interface at B was modeled as a no-flow boundary for all species. The diffusion problem was solved for 348.15 K and 30 MPa. The transient solutions were calculated over the interval from 0 to 25 ka at which time the system reached equilibrium.

Initially the pore fluid was assumed to be in chemical equilibrium with the sandstone mineral assemblage and was calculated to have the composition summarized in Table 6. For the 8-component system at the given P-T conditions, the baseline sandstone assemblage of 7 phases (six minerals + one brine), is thermodynamically invariant according to the Gibbs phase rule. Namely, there are 7 phases and 7 mineral components plus one additional component (Cl^-) that does not enter any mineral phase. Its concentration was assumed to be externally determined: Cl^- concentration was set to 2.146 mole kg^{-1} (Table 6). The invariance of this sandstone assemblage means that the initial concentration of dissolved CO_2 is buffered at a small concentration, ~10^{-4} mole kg^{-1}, as summarized in Table 6.

Table 6: Baseline brine composition[1] based on average oil-field brine compositions

	Average Brine (molality) [2]	Theoretical Brine (molality)[3]
pH	-	7.81
Cl^-	2.146	2.146
Na^+	1.620	1.712
Ca^{2+}	0.258	0.217
K^+	0.012	1.1×10^{-3}
Al^{3+}	-	9.9×10^{-8}
SiO_2	-	3.0×10^{-4}
HCO_3^-	0.0040	9.5×10^{-5}

[1] The molalities are given as component molalities, i.e, as the sum over all species containing the component

[2] Composition is based on North American oil-field brines as summarized in the Supp Material, Table S1, where data were from Collins (1975)

[3] This column shows the initial composition of aqueous brine in equilibrium with the mineral assemblage Qtz+Mc+Ill+Cc+Olg+Smct. The ionic strength of this solution is 2.41. This is the brine composition used for the baseline model.

At time zero, the supercritical CO_2 phase was emplaced at boundary A. The profiles of propagation of reacting $CO_{2,aq}$ into the brine in the sandstone and the resultant pH values are shown in Figure 5 where depth down into the sandstone appears as horizontal distance. In the model with L_{AB} = 3 m, ~ 100 a are required for $CO_{2,aq}$ to reach the underlying shale. In other words, 100 a is the time needed to attain 2/3 of the $CO_{2,aq}$ value maintained constant at boundary A. (Note that 2/3 was chosen as an arbitrary value because any value could have been chosen such as 95%, 99%, etc.)

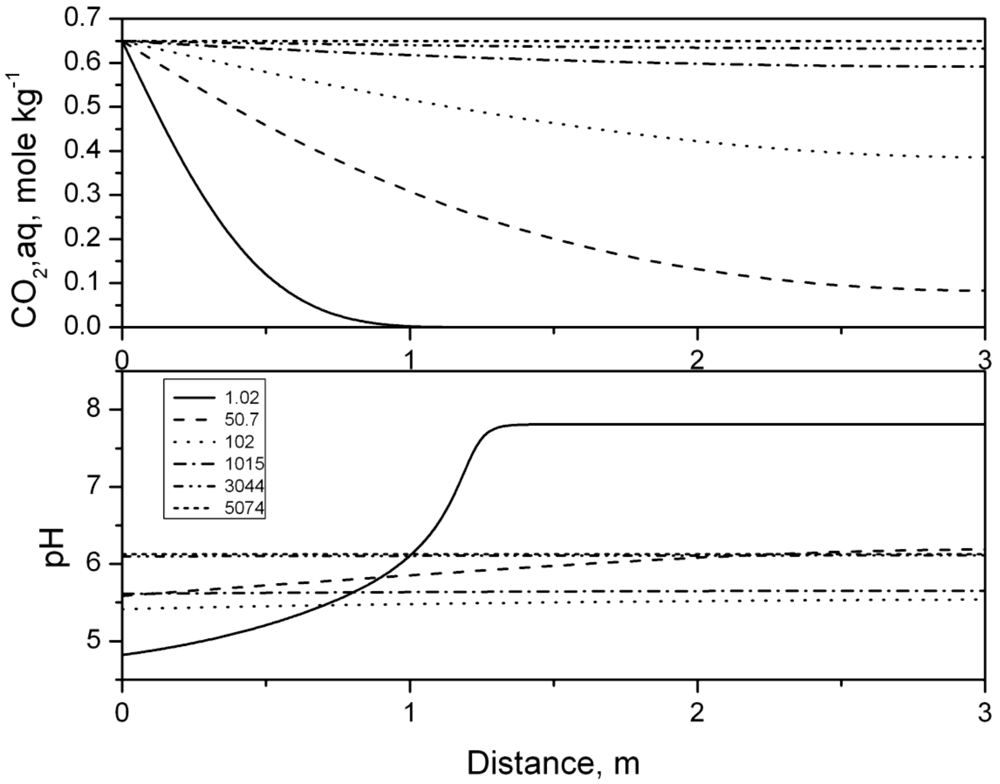

Figure 3: The calculated concentrations of $CO_{2,aq}$ (top) and pH (bottom) plotted as a function of distance inside the sandstone layer at different times (years) as noted for the reactive diffusion model with L_{AB} = 3m. Note that here, distance is the distance downward away from the buoyant CO_2 plume, toward the lower shale caprock (compare with Figures 1 and 2).

So far, the choice of the length of sandstone simulated, L_{AB} (see Figure 1), has not been discussed. By analogy with metamorphic systems (Balashov and Lebedeva, 1989), it is clear that a critical length, L^*_{AB}, exists such that for values $L_{AB} > L^*_{AB}$ (Figure 1), redistribution of CO_2 from the supercritical phase into the brine and mineral phases will proceed by formation of distinct mineral reaction fronts that approach the limit of local chemical equilibrium, LCE, for reactive diffusion. Here, LCE is the hypothetical case such that the reaction kinetics are fast and chemical equilibrium is everywhere achieved. Theoretically, if $L_{AB} >> L^*_{AB}$, LCE will be attained if diffusion is allowed to proceed for a long-enough period of time. The characteristic time needed to attain the maximum extent of CO_2 sequestration at equilibrium, τ, is a function of L_{AB} and D. It can be shown that $\tau \propto L^2_{AB}/D$ (Balashov and Lebedeva, 1989). For time > τ, the amount of CO_2 stored will not vary with the rate constants of mineral reactions. In contrast, for time < τ, the total amount of CO_2 stored will vary with the rate constants for mineral reactions.

For example, the computations represented in Figure 6 show that for $L_{AB} \leq 3$ m, diffusion-driven redistribution of CO_2 from the plume into the sandstone + brine is controlled by the kinetics of mineral/fluid reactions until the final equilibrium mineral assemblage. Using the results of these computations in combination with data on kinetics and diffusion and the LCE solution for reactive diffusion, it has been shown in the Supplementary Material that $L^*_{AB} \approx 20$ m. Above this critical length, the redistribution (sequestration) of CO_2 into the sandstone will be slowed due to slow rates of diffusion. In contrast, the distribution of phases for all values of $L_{AB} \leq 20$ m are identical (Figure 6).

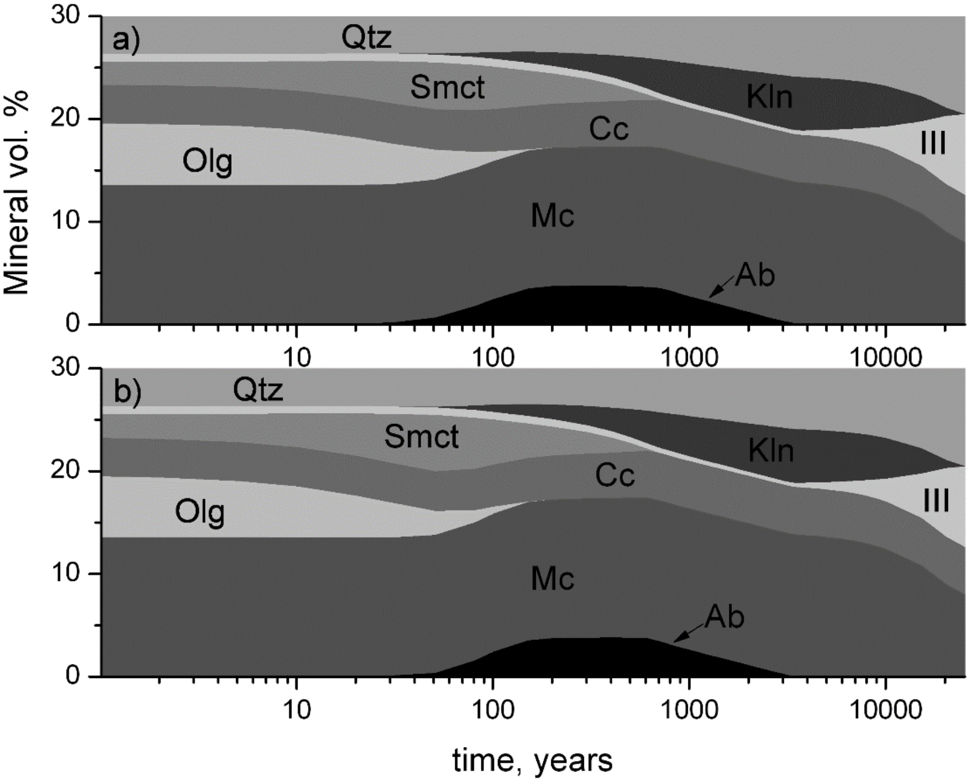

Figure 4: The calculated mineral composition plotted versus time for a) LAB = 3 m, b) LAB = 1 m. The composition was averaged across the entire layer of sandstone (i.e. across LAB in Figure 3). The figure documents that mineral evolution is the same for two small values of LAB, i.e., as long as LAB < L^*_{AB} **where this latter value is about 20 m (see text).**

A pH gradient forms inside the sandstone only during the first years. This pH gradient is eliminated as the cations—K^+, Ca^{++}, and especially Na^+—are released due to feldspar dissolution and the brine is charge-balanced by formation of HCO_3^-. After 50 a, the pH of the brine is buffered primarily by H_2CO_3 + $NaHCO_3$ (Figure 3 bottom). The average mineral volume fractions for the 3-m layer are shown as a function of time in Figure 5a. On the left side of the figure the mineral assemblage, Mc + Olg + Cc + Smct + Ill + Qz, is not yet equilibrated with brine + CO_2 and on the right side the assemblage, Mc + Ill + Qtz + Cc is entirely equilibrated with CO_2 + brine.

From a theoretical point of view, reactive diffusion into the sandstone is identical to a classic metamorphic system that is closed with respect to all components except CO_2 which diffuses in through boundary A (Figure 1). Using published terminology (Korzhinskii, 1936, 1970; Thompson, 1970), CO_2 can be considered a *perfect mobile component*. Given sufficient time, this system reaches a new equilibrium state where the chemical potential of CO_2 (μ^s_{CO2}) in the sandstone equals the chemical potential of CO_2 in the supercritical phase (μ^v_{CO2}) maintained at the interface A.

As shown later (Figure 6), CO_2 sequestration occurs throughout the reacting system as long as μ^s_{CO2} is changing (see Figure 3). Nonetheless, the sequestration (redistribution) of CO_2 at ~ 4 ka is very close to its maximum value. At this time, at a position 3 m from the plume, the CO_2 chemical potential in the sandstone is approximately equal to the value externally applied at interface A, μ^v_{CO2} . After 4 ka, the sluggish reactive process continues in the sandstone under SC CO_2 buffered conditions until complete equilibrium is attained at ~25 ka. The duration of time from 4 to 25 ka is necessary for illite to completely replace kaolinite (Chermak and Rimstidt, 1990b).

After a short induction time (<50 a), concentration of $CO_{2,aq}$ is significant across the entire simulation volume (Figure 3). After 1,000 a, very little change in this concentration is observed; however, as shown in Figure 5, the concentration of HCO_3^- increases significantly as albite dissolves to increase dissolved Na^+. However, the pH does not change significantly during this latter alteration process because the system is strongly buffered: from the initial value $\approx$ 7.2, pH decreases to 5 after 200 a, but increases again to 6 after that (Figure 5). The saturation indices, log (Q/K_{eq}), for minerals also vary significantly over time (Figure 5, bottom). Here Q and K_{eq} are the ion activity product and equilibrium constant for each mineral dissolution reaction. Figure 5 (bottom panel) shows that calcite and microcline are always at or near chemical equilibrium because of the fast kinetics of calcite and the relatively low microcline solubility in comparison with Na feldspars. For the simulations, quartz is in equilibrium with the initial brine and with the final brine + CO_2 fluid. However, between ~ 50 and 5,000 a, the pore fluid is supersaturated with respect to quartz as shown in Figure 5.

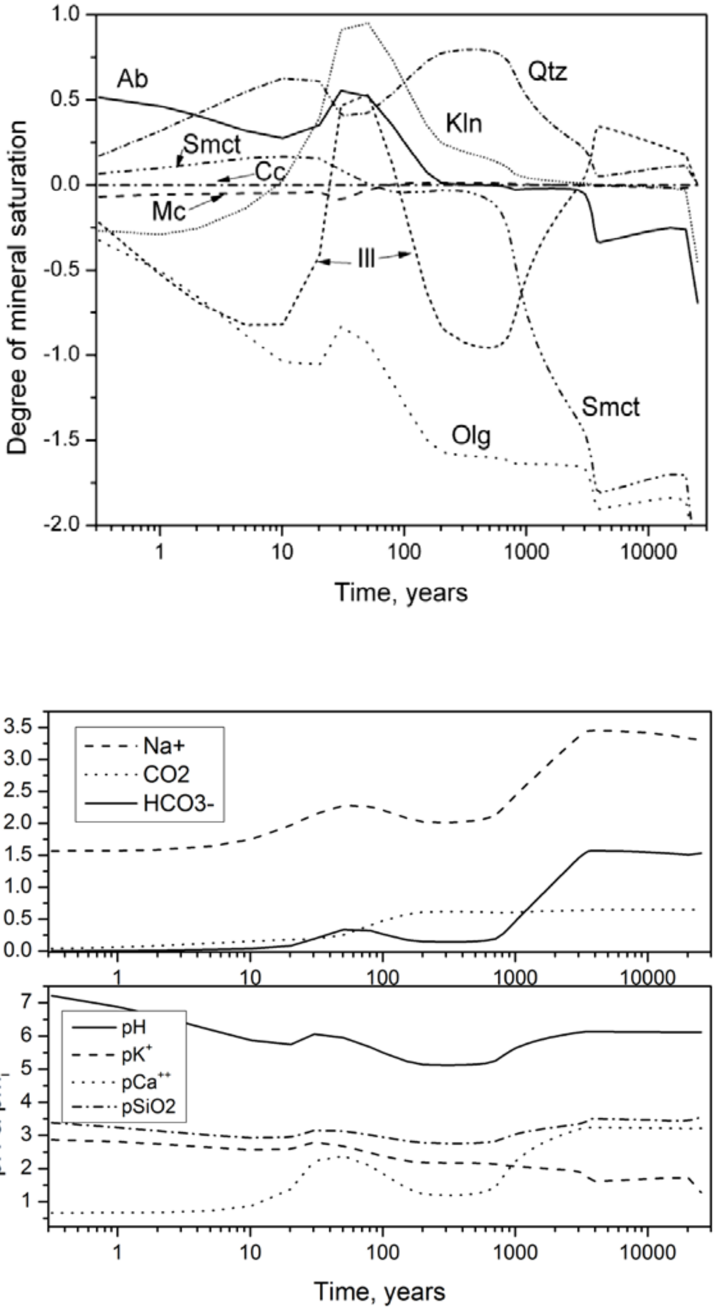

Figure 5: Plot of average molalities of Na^+, $CO_{2(aq)}$ and HCO_3^- versus time (top). Plot of average pH and -log $m_{i,aq}$ versus time (middle). Here "pm_i" refers to –log(m_i). All simulations for L_{AB} = 3 m. Average saturation indices, log (Q/K_{eq}), for minerals plotted versus time for the sandstone model with L_{AB} = 3 m (bottom).

The remarkable feature of Figure 5 (bottom) (in conjunction with Figure 4) is that three minerals (smectite, albite and kaolinite) are dissolved close to LCE within the time spans 60–800, 200–3,500, and 3,000–20,000 a, respectively. Immediately after complete dissolution, the saturation indices of these minerals decrease precipitously. This feature means that the reactive system evolves through a series of steps, termed kinetic stationary states.

Observations from Figures 4 and 5 are summarized in Table 7. Reactive diffusion of $CO_{2,aq}$ dissolves oligoclase until dissolution is complete by ~ 100 a. As Ca is released from oligoclase, two other Ca-containing minerals—calcite and, especially, smectite, precipitate. The smectite precipitation is promoted by supersaturation due to silica release during oligoclase dissolution. After ~50 a, the precipitation of albite and kaolinite become significant; at that point, smectite begins to dissolve close to LCE. Smectite disappears by 800 a. After 4,000 a, illite begins to grow at the expense of kaolinite and microcline.

Table 7: Summary of mineral/fluid reactions[1] due to CO_2 invasion into sandstone

Reaction Progress	0–10 a	10–50 a	50–100 a	100–1,000 a	1,000–5,000 a	5,000–10,000 a
< 0.1	Mc↓ Cc ↑	Mc↓ Ab ↑	Mc↓ Kln ↑	Mc↑ Ab ↑	Mc↑	
0.1–0.9	Olg ↓	Smct ↑ Olg ↓ Cc ↑	Ab ↑ Smct ↓ Olg ↓	Kln ↑ Smct ↓	Kln ↑ Ab ↓	Ill ↑ Kln ↓ Mc ↓
> 0.9	Smct ↑		Cc ↑	Cc↑		

[1]The symbols M ↓ and M ↑ correspond to mineral dissolution and precipitation, respectively

With respect to mineral or solubility trapping of CO_2, the system is controlled most directly by the reactions of oligoclase, smectite, and albite. Specifically, trapping of CO_2 is determined by dissolution of oligoclase, by the replacement of smectite by calcite, and by the transformation of albite to kaolinite. The first two reactions control concentrations of Ca in solution (which controls mineral trapping) and the latter reaction controls the conversion of $CO_{2,aq}$ into $HCO_3^{-}{}_{,aq}$ (solubility trapping). By ~ 3,500 a, the albite disappears and CO_2 mineral trapping reaches its maximum. Although mineral trapping of CO_2 stops by 1,000 a and $HCO_3^{-}{}_{,aq}$ trapping essentially stops by 3,500 a, the very slow kinetics of kaolinite + microcline replacement by illite determines the rate of final equilibration to Mc+Ill+Cc+Qtz, which is achieved only by 25,000 a. During this process there is additional small HCO_3^- trapping because of the growth in aqueous $KHCO_3$ concentration (Figure 6).

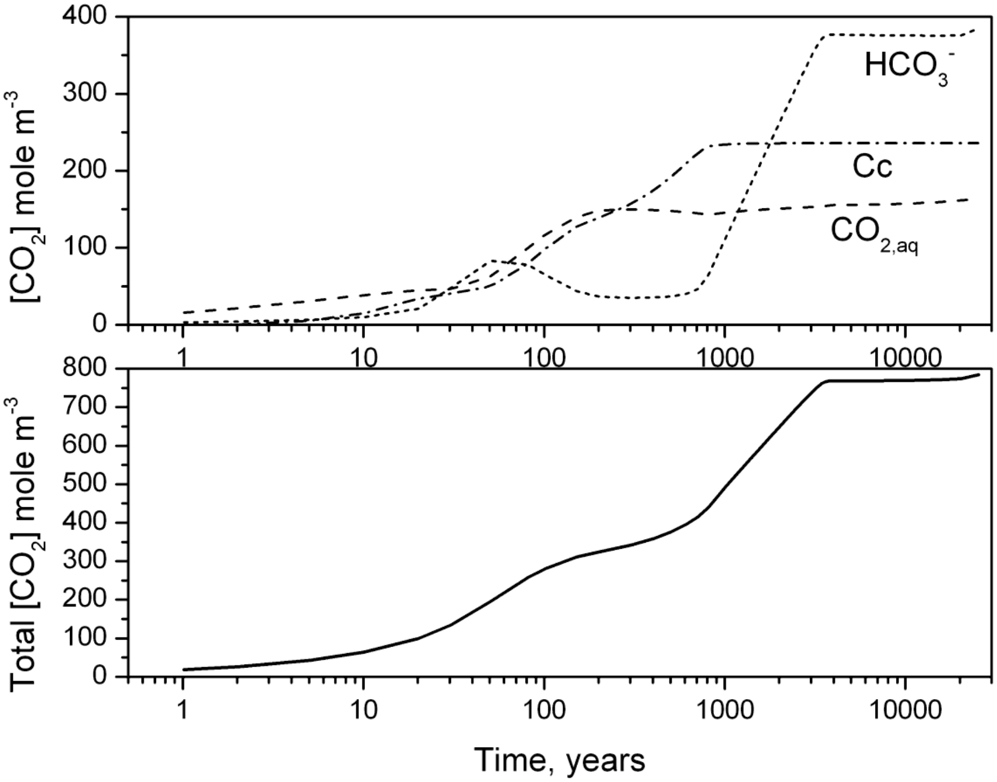

Figure 6: The average CO_2 stored per m^3 of a sandstone layer of 3-m thickness. Top: the dashed line shows the direct CO_2 dissolution in aqueous brine by plotting the concentration of $CO_{2(aq)}$; the short-dashed line corresponds to CO_2 dissolution with conversion into HCO_3^-; the dot-dashed line corresponds to mineral trapping due to calcite precipitation. Bottom: the total sum of stored CO_2 by the three mechanisms. The maximum stored CO_2 equals 784 mole per m^3 sandstone, or 34.5 kg CO_2 per m^3.

3.3 EVOLUTION OF CO_2 SEQUESTRATION

Carbon dioxide diffusion into the brine-saturated sandstone is essentially an acid-base titration: the acid is the H_2CO_3 formed as CO_2 gas dissolves in the aqueous fluid and the base is the rock itself. Therefore, during the reactive diffusion, CO_2 is stored by three mechanisms: 1) dissolution of CO_2 into aqueous brine ($CO_{2,aq}$); 2) hydration and deprotonation of CO_2 to form HCO_3^- (+ minor CO_3^{2-}); and 3) precipitation of calcite. Mechanisms (1) and (2) comprise solubility trapping while mechanism (3) comprises mineral trapping. Furthermore, mechanism (1) is simply dissolution of the CO_2. In contrast, mechanism (2) is the acid-base titration of Na,Ca,K-silicates dissolving into water-CO_2 to form HCO_3^- + CO_3^{2-} ions that charge-balance the hard cations, Na, Ca, K. This solubility trapping is largely due to dissolution of feldspars, in particular, Na feldspars. Notably, although the details of these processes will depend upon the exact mineralogy of the sandstone reservoir, the overall trends noted here will be true for most systems.

The average concentrations of stored CO_2 in moles per m^3 sandstone by the three different mechanisms were calculated for the model with L_{AB} = 3 m to yield what are called here the *standard curves* shown in Figure 6. These were computed with the *standard* set of kinetic constants of mineral dissolution/precipitation (Table 4). Figure 6 shows that CO_2 sequestration was complete to within 97% of the maximum value by 3,500 a. After 3,500 a, the main mechanism by which HCO_3^- forms, i.e., albite transformation to kaolinite + quartz, ceases:

$$2\,\mathrm{CO_2} + 3\mathrm{H_2O} + 2\mathrm{Ab} \rightarrow 2\mathrm{Na^+} + 2\mathrm{HCO_3^-} + \mathrm{Kln} + 4\mathrm{Qtz} \qquad (21)$$

For t > 3,500, the main alteration reaction is the replacement of kaolinite by illite to form the equilibrium assemblage Qtz + Cc + Mc + Ill. During that last process, the CO_2 chemical potential inside the sandstone equilibrates to the chemical potential of CO_2 in the gas plume at the interface A. Thus, the last 3% of the total CO_2 is stored as HCO_3^- during the last stage of sandstone alteration as microcline dissolves to form aqueous $KHCO_3$. This last stage occurs under conditions of so-called “perfect mobile CO_2 behavior” (Korzhinskii, 1970).

For the baseline sandstone, the maximum amount of stored CO_2, $[CO_2]_{\max}$, equals 784 mole per m^3 of sandstone (Figure 6), or 34.5 kg CO_2 per sandstone m^3. This quantity defines the absolute capacity of the saline baseline sandstone reservoir for CO_2 sequestration. This maximum is comprised of 21% CO_2 dissolved as $CO_{2,aq}$, 49% dissolved as HCO_3^-, and 30% precipitated as calcite, i.e., 70% solubility trapping and 30% mineral trapping. The extent of sequestration as HCO_3^- is mainly determined by the amount of Na^+ in the initial sandstone in the soluble Na-containing mineral (here, oligoclase); in contrast, the extent of trapping in calcite is determined by the initial content of soluble Ca-silicates (here, oligoclase and smectite). These final solubility: mineral trapping ratios do not depend upon the reactive transport model, but rather can be readily calculated from the initial sandstone composition if the initial and final equilibrium states of the thermodynamic system are calculated. The reactive transport model determines the paths of evolution between initial and final states.

The efficiency of CO_2 redistribution from the CO_2 plume into the saline reservoir can be defined as the ratio of $[CO_2]_{\max}$ to the mass of SC CO_2 in reservoir pores at full saturation (= 1) by SC CO_2. Here $[CO_2]_{\max}$ equals 34.5 kg m^{-3}. The density of SC CO_2, ρ_{CO2}^{sc} = 760 kg m^{-3}, at 75°C and 30 MPa, means that the maximum mass of SC CO_2 per m^3 is $[CO_2]_{tot}^{sc} = \rho_{CO2}^{sc}\phi$ = 190 kg m^{-3} for the baseline sandstone with porosity ϕ = 0.25. The baseline sandstone efficiency ratio is, therefore, $[CO_2]_{\max} \big/ [CO_2]_{tot}^{sc}$ = 0.18.

3.4 KINETIC SENSITIVITY ANALYSIS

The kinetic sensitivity analysis is divided into two parts. In the first part the focus is on the impact of kinetic rate constants on stored CO_2 (in units of moles CO_2/ m^3 of brine-saturated sandstone). The second part concentrates on the time sequence of important controlling minerals, i.e., rates of appearance (albite) and disappearance (oligoclase, smectite, albite). The minerals appear and disappear to define mineral “waves” that either propagate from the plume boundary to the shale boundary or the reverse. To determine the sensitivity of the models to the choice of rate constants for smectite, oligoclase and albite, sensitivity tests were run for L_{AB} = 3 m for a sandstone at 75°C and 30 MPa. As discussed above, reactive-diffusive CO_2 sequestration in this model does not depend on L_{AB} for $L_{AB} < L^*_{AB} \cong 20$ m.

By summing the three curves in Figure 8, the total CO_2 stored in the brine portion of the reservoir is calculated as a function of time (bottom panel in Figure 8). Different choices of mineral rate constants were explored to determine how they change the total CO_2 stored (Figure 9). The results are reported by summarizing the *sensitivity factor*, $[CO_2]^{var} \big/ [CO_2]^{std}$, where $[CO_2]^{std}$ is the mass of CO_2 per m^3 of reservoir stored in the standard model (Table 4) and $[CO_2]^{var}$ is the same mass calculated with variations in the rate constants. The variations in kinetic constants sometimes do and sometimes do not change the path; of course, these variations never change the final value (Figure 7).

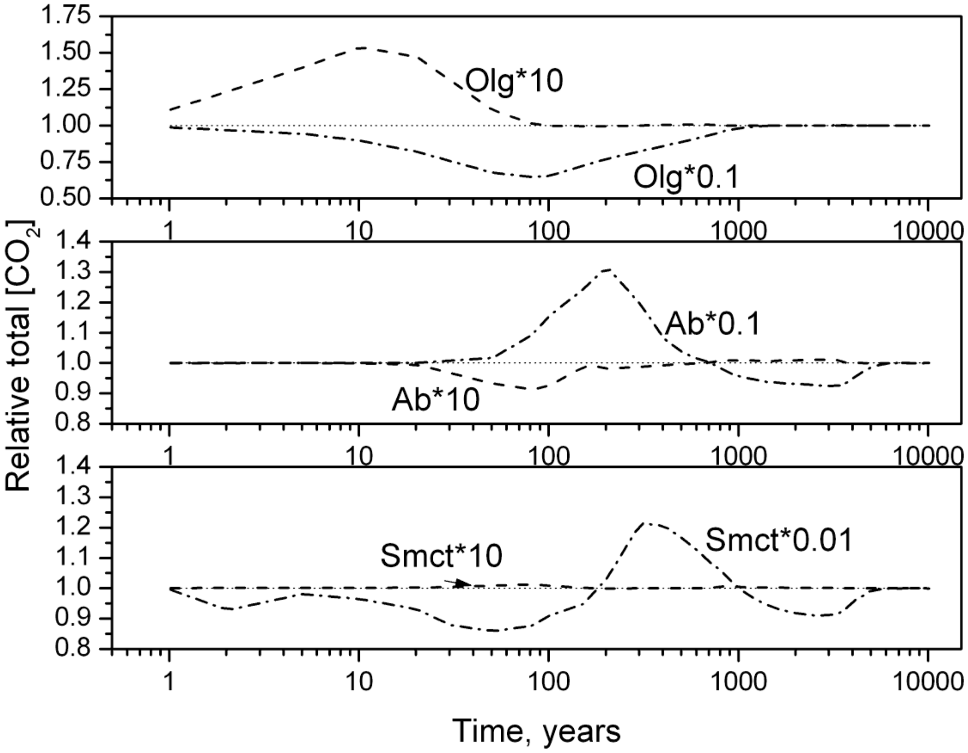

Figure 7: The effect of changes in the rate constants for oligoclase, albite and smectite on the relative total CO_2 stored in the sandstone (*sensitivity factor*, $[CO_2]^{var} \big/ [CO_2]^{std}$, see details in text) plotted versus time. In the Ab and Smct cases, the sequestration is most sensitive to a decrease in the rate constants rather than an increase. This is because a decrease moves the system into the regime of kinetic limitation whereas an increase causes the system to approach equilibrium. Note that the ordinate is scaled differently in the panels; for example, in this figure, the sensitivity factor for changing the oligoclase rate constant is the largest.

For example, for a 10 times increase in the smectite rate constant, the total sequestration curve does not change at all (compare the dashed and dotted lines in Figure 7, bottom). In contrast, a 100 times decrease in smectite rate constant (dash/dotted line) leads to a decrease in the total CO_2 stored over the interval from 10–150 a by a sensitivity factor of 0.85, to an increase in CO_2 stored during 150–1,000 a by a sensitivity factor of 1.2, and, finally, to a decrease in sequestration from 1,000–4,000 a by a factor of 0.9. The maximum deviation in stored CO_2 compared to the standard curve equals ~ 80 mole m^{-3} (Figures 6–7). Figure 7 also shows that changes in the rate constants for oligoclase and albite affect CO_2 storage more than that of smectite, especially in the interval 10–200 a.

The extent of CO_2 stored by the different mechanisms also changes with time when the rate constants for mineral reactions are changed (Figures 8–10). A 10 times decrease in the oligoclase rate constant increases the $CO_{2,aq}$ stored from 2–80 a (Figure 8). In contrast, a 10 times increase in the oligoclase rate constant leads to a decrease in stored $CO_{2,aq}$ in the 20–100 a interval (Figure 8). If the oligoclase rate constant is 10x faster, more of the CO_2 is precipitated as calcite from 10–100 a. These individual effects are larger than the summed total effect (Figure 7) because of compensation effects (Figure 8).

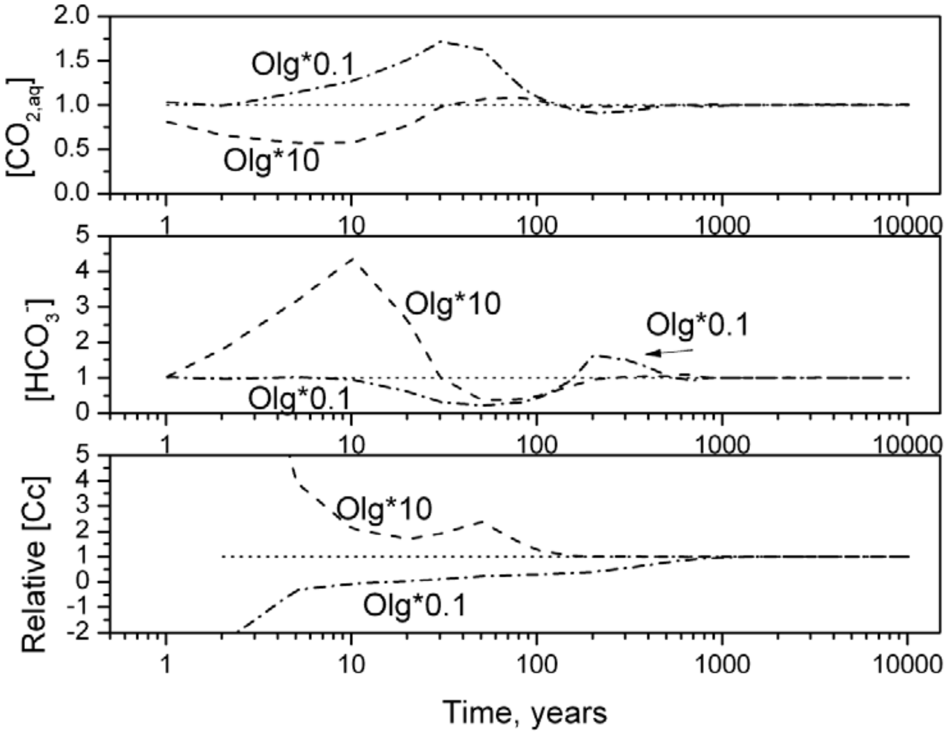

Figure 8: The effect of the oligoclase rate constant on CO_2 sequestration for the three mechanisms. The sequestration is most sensitive to a 10 times decrease in the rate constant after about 10 a.

These observed compensation effects are kinetic in nature and can be explained qualitatively. For example, consider a 10 times increase in the oligoclase (Olg) kinetic constant. In the time interval 0–10 a, it leads to higher aqueous concentrations of Na^+ and silica due to oligoclase dissolution; the higher [Na^+] leads to an increase of [HCO_3^-], and higher silica promotes more intensive smectite precipitation which decreases calcite precipitation (Figure 10). Note that here and throughout, [x] refers to concentration of species *x* in solution. In the time interval 10–60 a, albite precipitation decreases [HCO_3^-] and aqueous silica, which in turn decreases smectite precipitation. This then in turn promotes an increase in calcite precipitation (Figure 8).

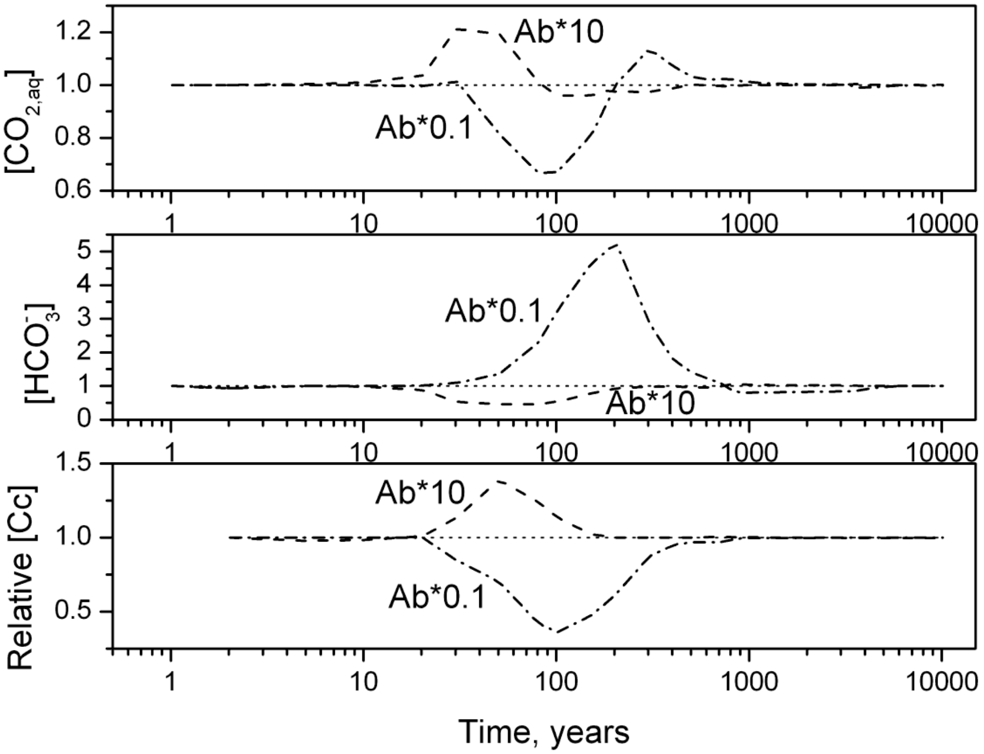

Figure 9: The effect of changes in the albite rate constant on CO_2 storage over time by the three different mechanisms. Storage is more sensitive to a 10 times decrease in the rate constant than an increase, starting from about 20 years on.

In contrast to oligoclase, a 10 times increase in the albite rate constant decreases the total CO_2 stored from 30–110 a (Figure 7), but the effect is not large. The effects of changes in the albite rate constant on CO_2 storage by the three mechanisms are broken out in Figure 9. Again, these independent effects are bigger than the total summed effect (Figure 7), because of strong compensation (Figure 9). For example, in the time interval 20–100 a, a 10 times decrease in the Ab kinetic constant leads to higher aqueous concentrations of Na^+ and silica; the higher [Na^+] leads to an increase of [HCO_3^-], and higher silica promotes more intensive smectite precipitation which decreases calcite precipitation (Figure 9).

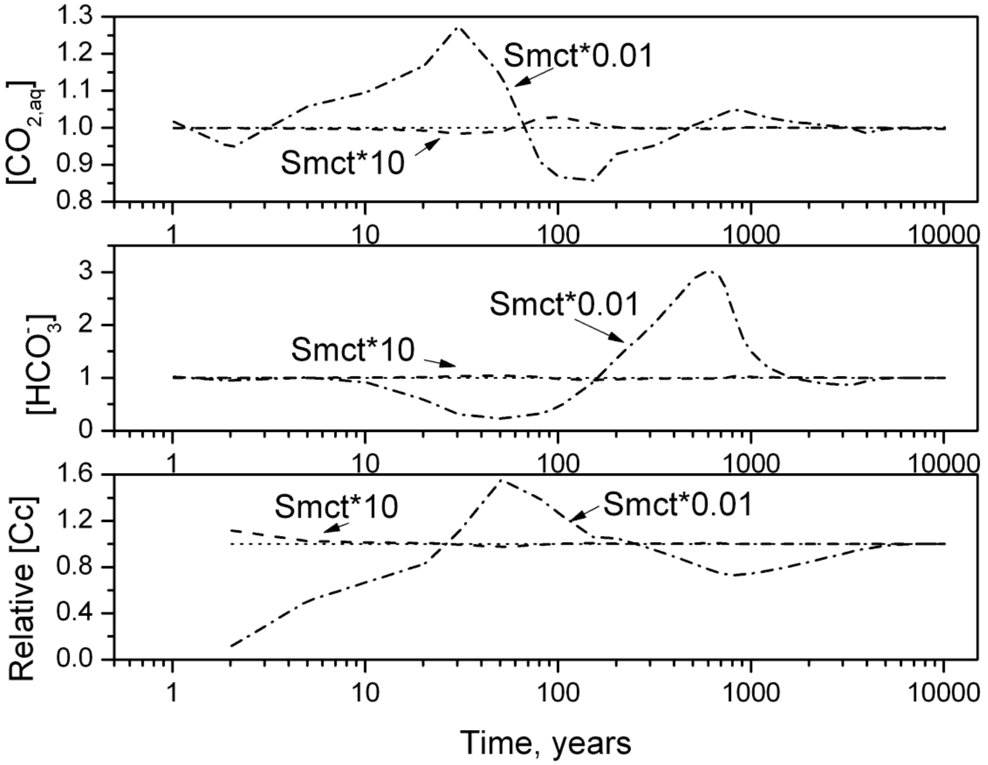

Figure 10: The effect of changes in the smectite rate constant on CO_2 stored versus time for the three sequestration mechanisms. Storage is sensitive to a 100 times decrease in the rate constant, starting at 10 a.

A decrease in the smectite kinetic constant significantly affects sequestration as HCO_3^- and as calcite (mineral trapping, Figure 10). However, these individual effects are each larger than the total summed effect (Figure 7) because of kinetic compensation (Figure 10). In fact, a slower smectite rate constant shifts the sequestration to calcite precipitation around the 100 a mark, but lowers the amount of calcite precipitated at 1,000 a.

The sensitivity analysis shows that CO_2 sequestration is sensitive to the mineral rate constants, decreasing in sensitivity in the following order: oligoclase > albite > smectite. Furthermore, the effect of the smectite rate constant is only significant if the rate constant decreases, whereas for the feldspars, either an increase or a decrease impacts the sequestration. In brief, the importance of the rate constant for albite is related to solubility trapping by formation of $HCO_3^-{}_{,aq}$ (i.e., albite dissolution releases aqueous Na) while the importance of the rate constant for smectite is related to mineral trapping by formation of calcite (i.e. smectite dissolution releases aqueous Ca). The rate constant for oligoclase is important for both solubility and mineral trapping because oligoclase releases both Na and Ca to solution.

3.5 TIME SEQUENCES OF MINERAL REACTION: SENSITIVITY TO RATE CONSTANTS

The sensitivity with respect to kinetics can also be explored by looking at mineral concentration profiles (Figures 11–12) for different times. At higher values of the smectite kinetic constant and for time < 80 a (Figure 11), smectite precipitates as an intensive wave that is maximized at x = 0. Precipitation reaches the maximum concentration at ~ 80 a. After 80 a, the smectite wave propagates backward as smectite dissolves. A 100 times decrease in the smectite kinetic constant suppresses this effect. In contrast to smectite, the oligoclase profiles (Figure 11) show only a dissolution wave that propagates in the forward direction.

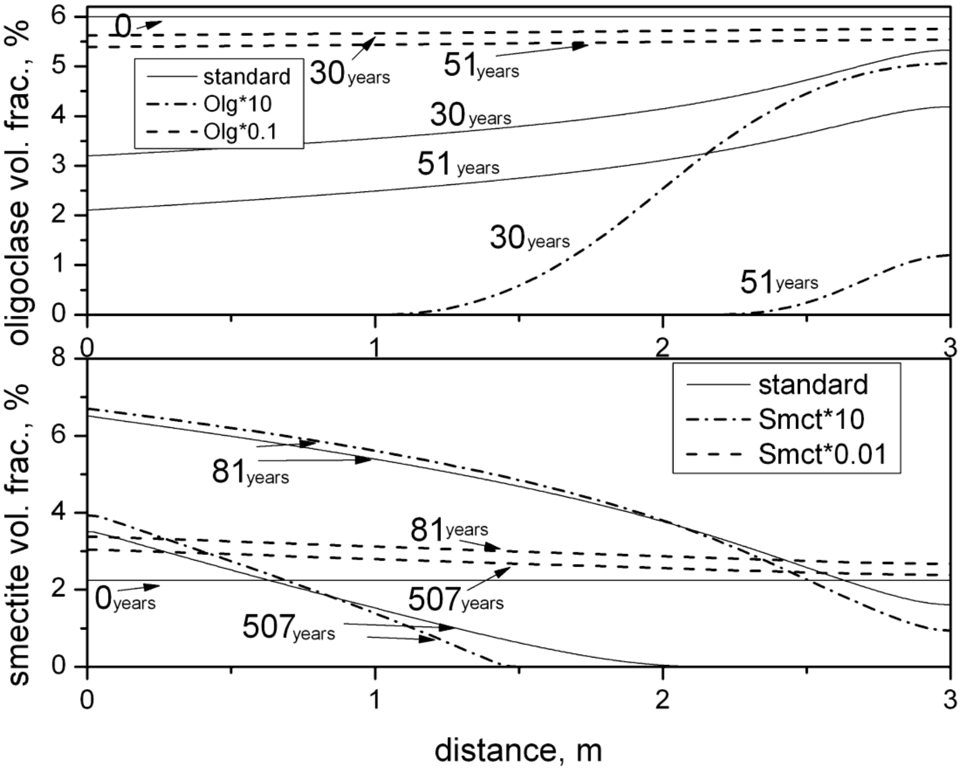

Figure 11: Plots of oligoclase (top) and smectite (bottom) volume fractions versus distance inside the 3-m thick sandstone layer for different values of the oligoclase and smectite kinetic constant. The numbers mark the profile times in years.

Smectite precipitation is promoted by the high concentration of dissolved silica that is caused largely by oligoclase dissolution, whereas smectite dissolution is conditioned by the decrease in alumina concentration caused by albite precipitation. A similar coupling with respect to dissolution/precipitation of smectite and feldspars through dissolved silica concentrations was observed in computations of mineral profiles in soils during continental weathering (Goddéris et al., 2010).

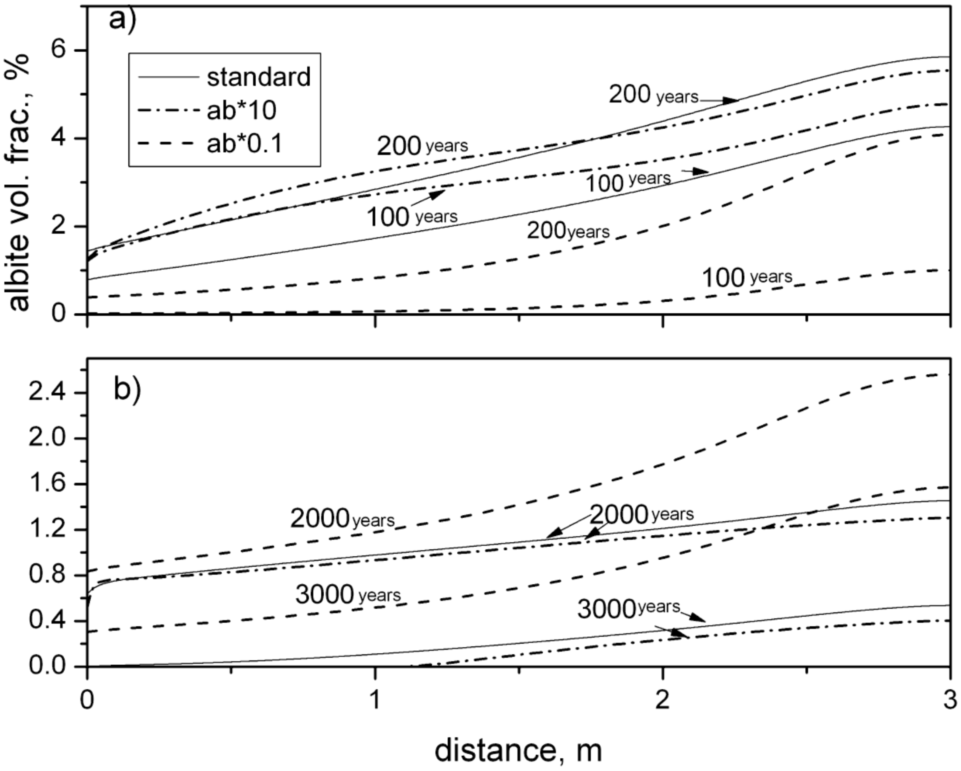

Figure 12: Plots of albite volume fractions versus distance inside the 3 m-thick sandstone layer plotted for different values of the albite kinetic constant. The numbers mark the profile times in years: a) albite precipitation waves; b) albite dissolution waves. Note that distance plotted horizontally on this figure corresponds to depth downward from interface A in Figure 2.

The albite profiles plotted in Figure 12 show that the albite precipitation waves propagate backward while the dissolution waves propagate forward. Of course, these directions are actually upward and downward respectively within the context of the actual system (Figure 1 and 2). In general, the gradient of mineral concentrations reflects the gradient of the chemical potential of CO_2 through the sandstone layer.

3.6 MINERAL REACTION NETWORKS

The reactive interaction among minerals is summarized in Figure 13. For example, an increase in the oligoclase kinetic constant is coupled positively to smectite and albite: as the reaction rate of oligoclase increases, the maximum concentration of both smectite and albite also increase. (Likewise, a decrease in the oligoclase kinetic constant decreases the maximum concentrations of smectite and albite.)

In contrast, an increase in the albite kinetic constant is coupled negatively to smectite: as the albite rate constant increases, the maximum predicted concentration of smectite decreases. Likewise, a decrease in the albite kinetic constant increases the maximum concentration of smectite. Furthermore, smectite and albite demonstrate the effect of a positive kinetic auto-response; an increase in the value of their kinetic constants leads to an increase in their maximum predicted concentrations (Figure 13b).

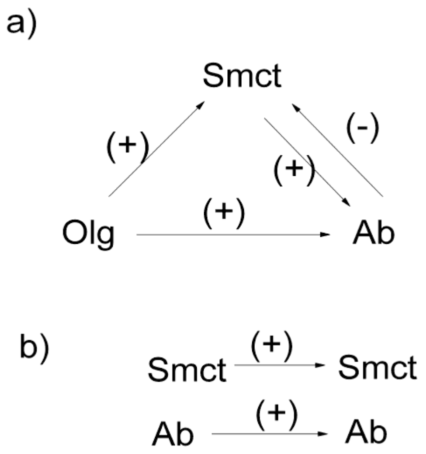

Figure 13: Interaction among minerals during CO_2 sequestration. The arrows show the direction of kinetic coupling, where (+) corresponds to positive kinetic coupling and (-) refers to negative kinetic coupling. a) The coupling between different minerals; b) a positive auto-response to smectite and albite kinetic constants is also observed.

The observed kinetic coupling among minerals is explained by the non-linearity of the kinetic law, i.e., Equation 15. The rate of mineral reaction is proportional to the product of the kinetic constant times the deviation from equilibrium. This deviation from equilibrium is a non-linear function of the dissolved concentrations of mineral components. These concentrations change in the complex reactive system when the kinetic constants are varied. The aqueous concentrations serve to couple responses among the various minerals.

4. SIMULATION OF REACTION AND DIFFUSION AT THE RESERVOIR (SANDSTONE)/CAPROCK (SHALE) INTERFACE DURING CO_2 STORAGE

4.1 SETUP OF THE REACTIVE PROBLEM

To initiate the simulation, the model was parameterized for the interface of sandstone containing supercritical (SC) CO_2 (5 % of rock volume) and brine (20% of rock volume) with shale containing only brine (5% of rock volume).

In general, it is assumed that for CO_2 sequestration, the gas will be injected into a subhorizontal layer of permeable rock (e.g., sandstone) overlain by a low-permeability rock (e.g., shale) (Benson and Cook, 2005). After injection, the supercritical CO_2 plume will first be stabilized physically, forming a plume entirely within the sandstone. Computations show that under favorable conditions, immobilization of SC CO_2 can occur within 25 years of CO_2 injection (Doughty, 2010), after which time the immobilized SC CO_2 is mostly trapped residually. In this case the CO_2 fills relatively disconnected clusters of pores. The plume in this case likely consists of a heterogeneous region of pores with the two immiscible phases, SC CO_2 and CO_2–saturated brine. The filling of the pores might have a complex geometry. For example, aqueous and CO_2 fluids will coexist within neighboring pores or even within the same pores in a homogeneous porous medium (Liu et al., 2010; Lu et al., 2009). The estimation of residual SC CO_2 phase as 5% of sandstone volume with a sandstone porosity of 25% would correspond to a residual CO_2 saturation of 20%. This is a reasonable value given that most estimations have been equal to or less than 30% (Szulczewski et al., 2012).

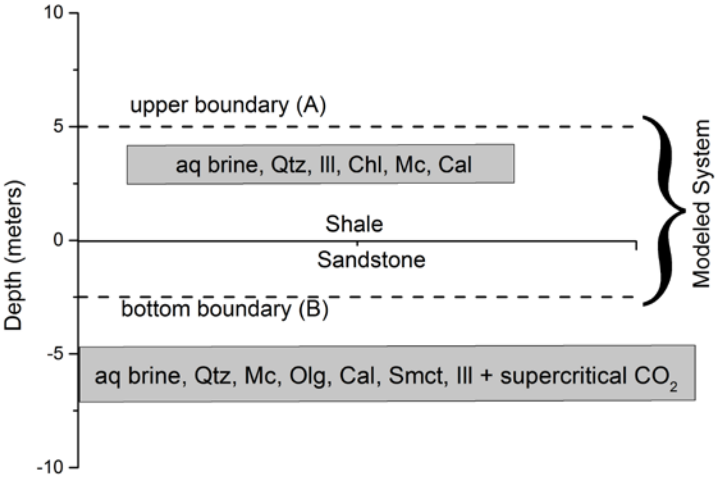

Figure 14: Setup of the reactive diffusion model for simulation of the contact between the reservoir (sandstone) and the caprock (shale). The schematic shows the bottom boundary (B), interface boundary (I), and upper boundary (A). Five percent of the bulk sandstone volume is initially filled by residual SC CO_2 phase. It makes the initial sandstone porosity equal to 20%.

Within the upper part of the plume, the CO_2 diffuses into the shale caprock (Gaus et al., 2005). The general setup of the reactive diffusion model is represented in Figure 1. The content of water in the supercritical CO_2 (SC CO_2) phase was assumed to be negligible as assumed in the first part of this work. In these calculations it was set to zero.

The model geometry was represented by two horizontal rock layers, a sandstone layer which is 2.5-m thick and a shale layer which is 5-m thick (Figure 14). The upper boundary (A) was modeled as a no-flux boundary for all species. The bottom boundary (B) was closed for all components except $CO_{2,aq}$ and $O_{2,aq}$. At boundary (B) the concentrations of $CO_{2,aq}$ and $O_{2,aq}$ were maintained constant. The boundary concentration (molality) of $CO_{2,aq}$ was set close to the value calculated after equilibration with the initial brine for the SC CO_2 phase at 75°C and 30 MPa ($m^{A}_{CO2,aq}$= 0.7434 mole kg^{-1}). The molality of $O_{2,aq}$ at the constant boundary was set equal to 7.427×10^{-9} mole kg^{-1}. This value is equivalent to 0.24 ppb dissolved O_2 and it corresponds to the low end of standard analytical determinations. This value was chosen because a small amount of O_2 can be mixed with CO_2 during injection. However, the numerical tests show that the simulations do not change for the case in which boundary (B) is maintained closed with respect to $O_{2,aq}$.

4.2 RESULTS FOR STANDARD KINETICS AND STANDARD SHALE TRANSPORT PROPERTIES

Initially the sandstone and shale pore fluids were calculated to be at chemical equilibrium (Table 1) with the sandstone and shale mineral assemblages (Table 2) as summarized in Table 8.

Table 8: Initial equilibrium speciation of sandstone and shale pore brines

	Sandstone	Shale
Chemical Entity	**Molality, mol kgw^{-1}**	
H^+	2.57×10^{-8}	3.78×10^{-7}
O_2°	6.63×10^{-63}	8.20×10^{-61}
Na^+	1.472	1.462
K^+	1.02×10^{-3}	$1.\ 5\times10^{-2}$
Mg^{++}	6.06×10^{-2}	6.06×10^{-2}
Ca^{++}	1.87×10^{-1}	1.86×10^{-1}
Fe^{++}	1.59×10^{-11}	3.64×10^{-14}
$Al(OH)_3^\circ$	3.48×10^{-10}	3.48×10^{-10}
SiO_2°	2.75×10^{-4}	2.75×10^{-4}
SO_4^{--}	1.59×10^{-3}	1.6×10^{-3}
Cl^-	1.968	1.969
CO_2°	$7.\ 5\times10^{-7}$	1.64×10^{-4}
OH^-	3.04×10^{-4}	2.07×10^{-6}
H_2°	5.14×10^{-9}	4.63×10^{-10}
$H_3SiO_4^-$	2.5×10^{-5}	1.7×10^{-6}
$NaCl^\circ$	1.33×10^{-1}	1.32×10^{-1}
KCl°	3.09×10^{-5}	4.55×10^{-4}
$MgCl^+$	1.75×10^{-3}	1.75×10^{-3}
$CaCl^+$	2.42×10^{-3}	2.4×10^{-3}
$CaCl_2^\circ$	9.8×10^{-4}	9.7×10^{-4}
$FeCl_2^\circ$	1.92×10^{-15}	4.39×10^{-18}
Fe^{+++}	2.43×10^{-26}	2.72×10^{-27}
$NaOH^\circ$	1.4×10^{-6}	9.46×10^{-8}
KOH°	1.84×10^{-9}	1.84×10^{-9}
Al^{+++}	2.79×10^{-16}	8.89×10^{-13}
$Al(OH)^{++}$	4.5×10^{-15}	9.75×10^{-13}
$Al(OH)_2^+$	6.37×10^{-13}	9.38×10^{-12}
$Al(OH)_4^-$	1.04×10^{-7}	704×10^{-9}
HCO_3^-	9.3×10^{-5}	1.38×10^{-3}
CO_3^{--}	6.8×10^{-6}	6.85×10^{-6}
HSO_4^-	1.11×10^{-9}	1.65×10^{-8}
$NaHSO_4^\circ$	8.74×10^{-10}	1.29×10^{-8}

Table 8: Initial equilibrium speciation of sandstone and shale pore brines (continued)

Chemical Entity	Sandstone	Shale
	Molality, mol kgw^{-1}	
$Na_2SO_4^{\circ}$	2.66×10^{-3}	2.64×10^{-3}
$NaSO_4^-$	1.15×10^{-3}	1.15×10^{-3}
$K_2SO_4^{\circ}$	7.26×10^{-12}	1.58×10^{-9}
KSO_4^-	8.31×10^{-7}	1.23×10^{-5}
pH	7.84	6.67
E_h (V)	-0.372	-0.255
V^w (dm^3 kgw^{-1})	1.018	1.018

Profiles of the concentrations of $CO_{2,aq}$, pH, and Eh in the pore brine are shown in Figure 17 after 10, 100, 1,000, and 5,000 years. Approximately 150 a are required for $CO_{2,aq}$ to reach the upper boundary of the shale (labeled A on Figure 14).

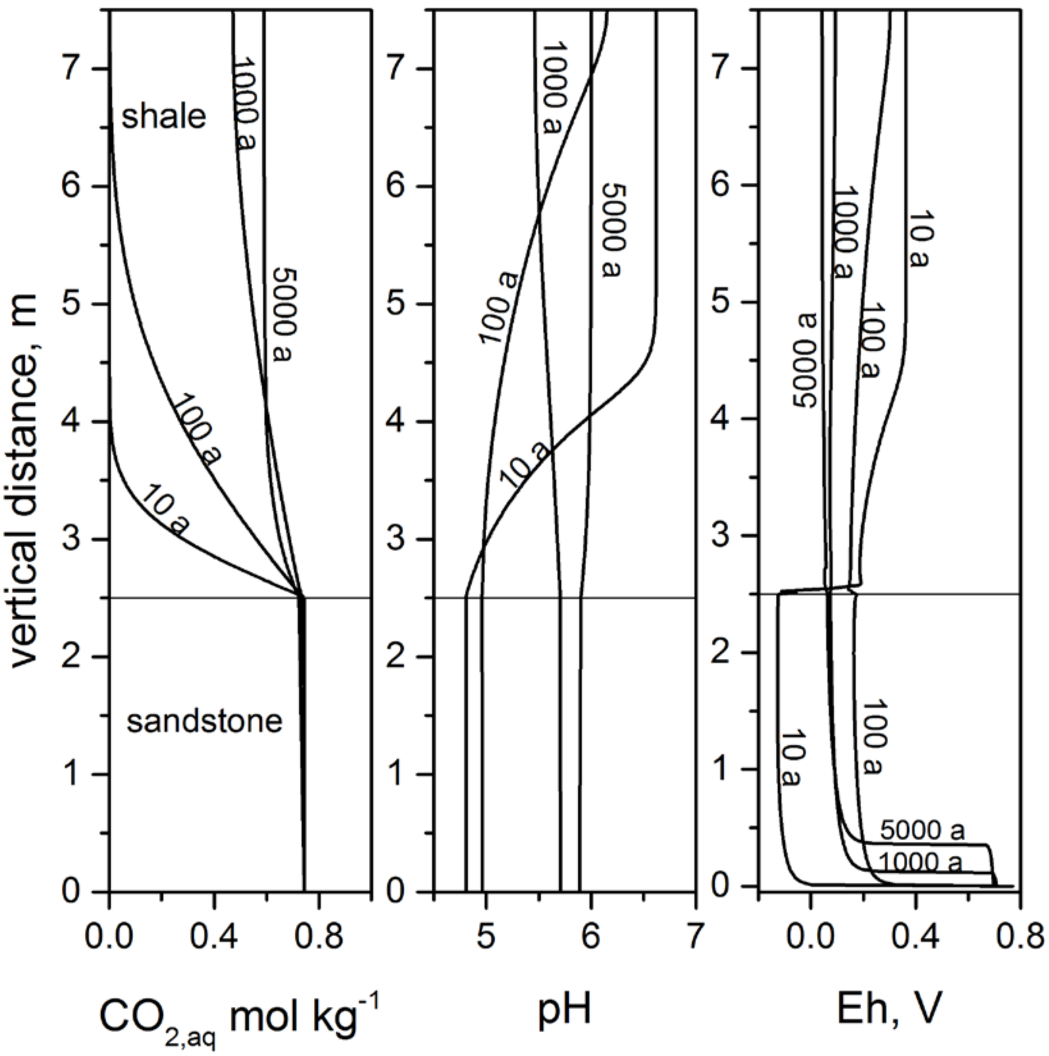

Figure 15: The profiles of distributions in vertical dimension through sandstone and shale for dissolved in brine $CO_{2,aq}$/mol kg^{-1} (left), pH (middle), and Eh/ V (right) at different times 10, 100, 1,000, and 5,000 years.

The mineralogy of the sandstone after alteration is very uniform. Therefore, the evolution in sandstone mineralogy is represented by changes in mineral abundances averaged across the entire sandstone unit. In contrast, the reaction process in shale varies significantly with distance from the boundary, with most alteration occurring within 1 m of the ss/sh contact. The extent of reaction is largest within a thin shale sub-layer at the ss/sh interface. The average mineral concentrations for these defined system sub-layers are plotted in Figure 16 and 17.

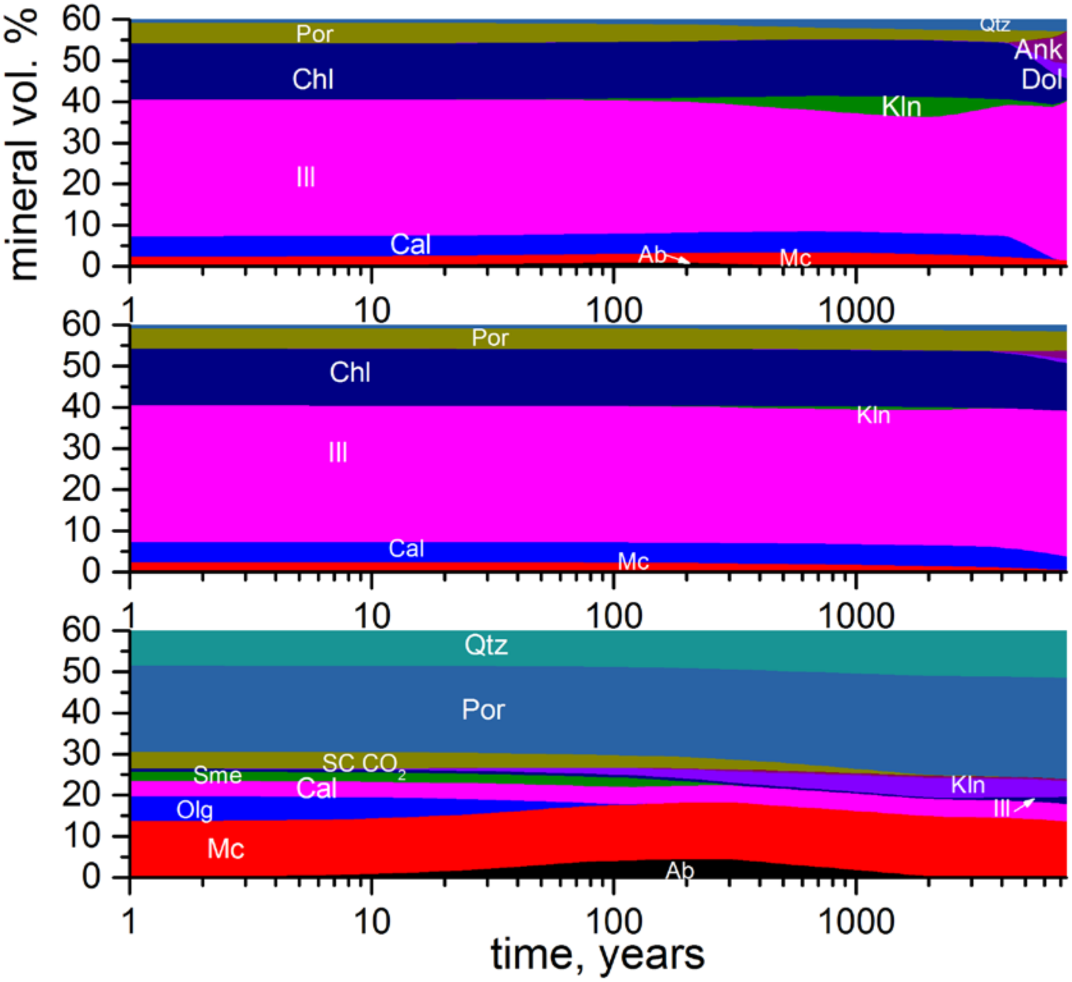

Figure 16: The evolution of the average mineral volume fractions in the shale at the ss/sh interface (top), in the shale in the 0–1 m sub-layer defined from the interface into the shale (middle), and in sandstone for the integral 0–2.5 m layer of sandstone (bottom).

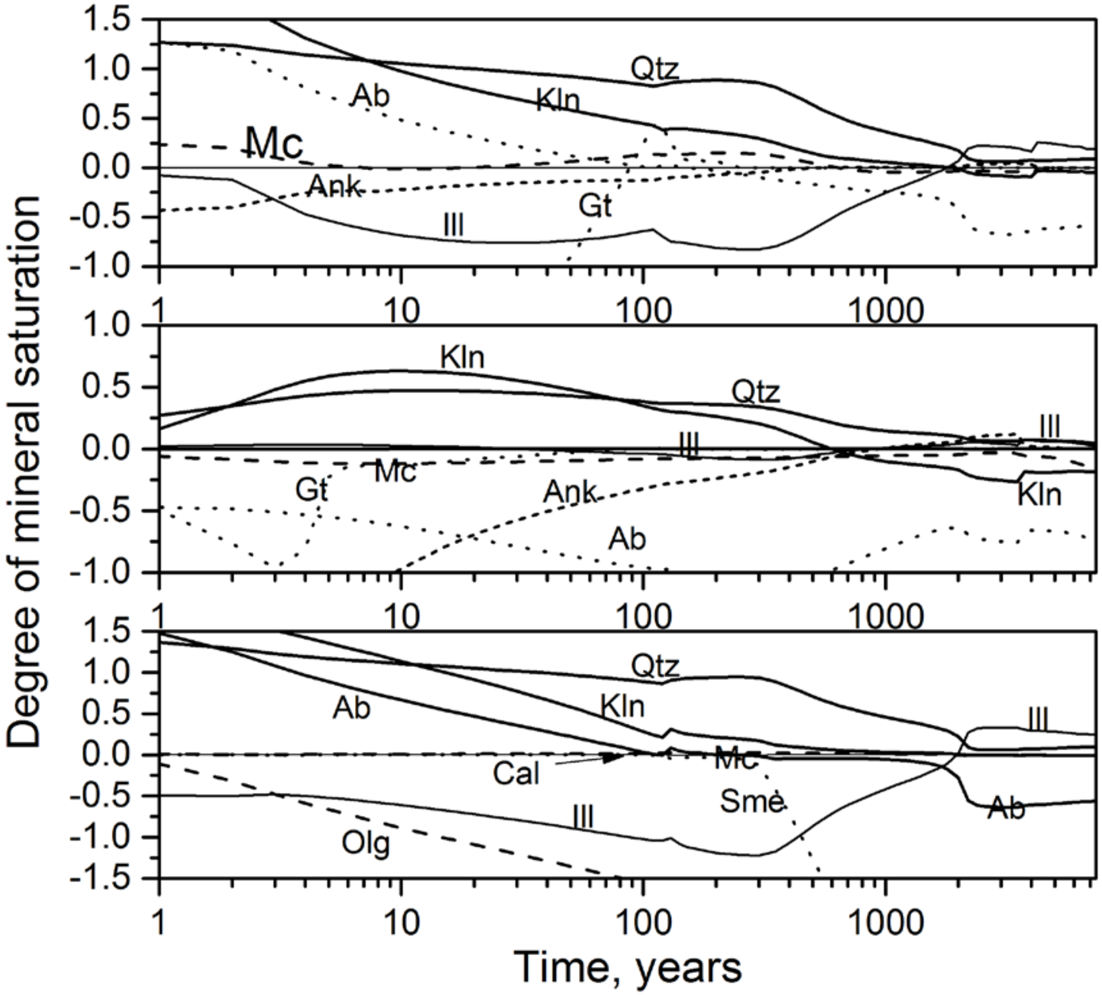

Figure 17: Average saturation indices, log(Q/K_{eq}), for minerals in shale at the ss/sh interface (top), in the shale for the 0–1 m sub-layer from the interface inward the shale (middle), and in sandstone for the integral 0–2.5 m layer of sandstone (bottom) plotted versus time.

The variations in average mineral volume fractions within the 2.5-m thick sandstone layer (bottom), within the 1-m thick shale sub-layer (middle) integrated from the ss/sh boundary inward shale, and for the 0.0125-m thick shale sub-layer at the ss/sh interface (top) are shown in Figure 16. The reaction is focused in a narrow zone at the ss/sh interface.

The time evolution of the average mineral saturation indices for the defined above three sub-layers of the modeled system are shown in Figure 17. The top (the thin ss/sh interface) and bottom figures (ss layer) have many similarities because the shale sub-layer (top) lies directly adjacent to the sandstone (bottom). In both cases the kaolinite and illite saturation curves show an inversion point—i.e. kaolinite precipitation switches to dissolution and illite dissolution switches to precipitation—at ~ 2,000 years. Before this point the pore brine is supersaturated in kaolinite and undersaturated in illite. After this point the brine is supersaturated by illite and undersaturated by kaolinite. This coupled behavior for Kln/Ill correlates with the decrease in quartz supersaturation (Figure 17, top and bottom) and the increase in potassium activity with time.

An important feature of the pore brine in the shale is the behavior of ankerite. In contrast to calcite and dolomite which are always at local equilibrium with pore brine, ankerite is strongly undersaturated during the first 600 years (Figure 17, top and middle), and then is close to local equilibrium until 2,000 years, and then is supersaturated during the next 2,000–3,500 years (Figures 19 and 20, top and middle). Precipitation of ankerite eventually completely seals the porosity at the ss/sh interface (7,416 years).

CO_2 is trapped in the sandstone by both mineral and solubility trapping. The system is controlled most directly by the reactions of oligoclase, smectite, and albite. Specifically, trapping of CO_2 is determined by dissolution of oligoclase and release of Ca, the replacement of smectite by calcite and dolomite, and by the transformation of albite to kaolinite. The first two reactions control concentrations of Ca in solution (which controls mineral trapping by controlling the solubility index of calcite) and the latter reaction controls the conversion of $CO_{2,aq}$ into HCO_3^- (solubility trapping). By ~ 2,000 years, albite disappears (Figure 16, bottom) and CO_2 solubility trapping reaches its maximum. In sandstone, although mineral trapping of CO_2 stops by 1,000 years and HCO_3^- solubility trapping essentially stops by 2,000 years, the very slow kinetics of kaolinite + microcline replacement by illite determines the rate of final equilibration to the assemblage, Mc+Ill+Cc+Dol+Qtz.

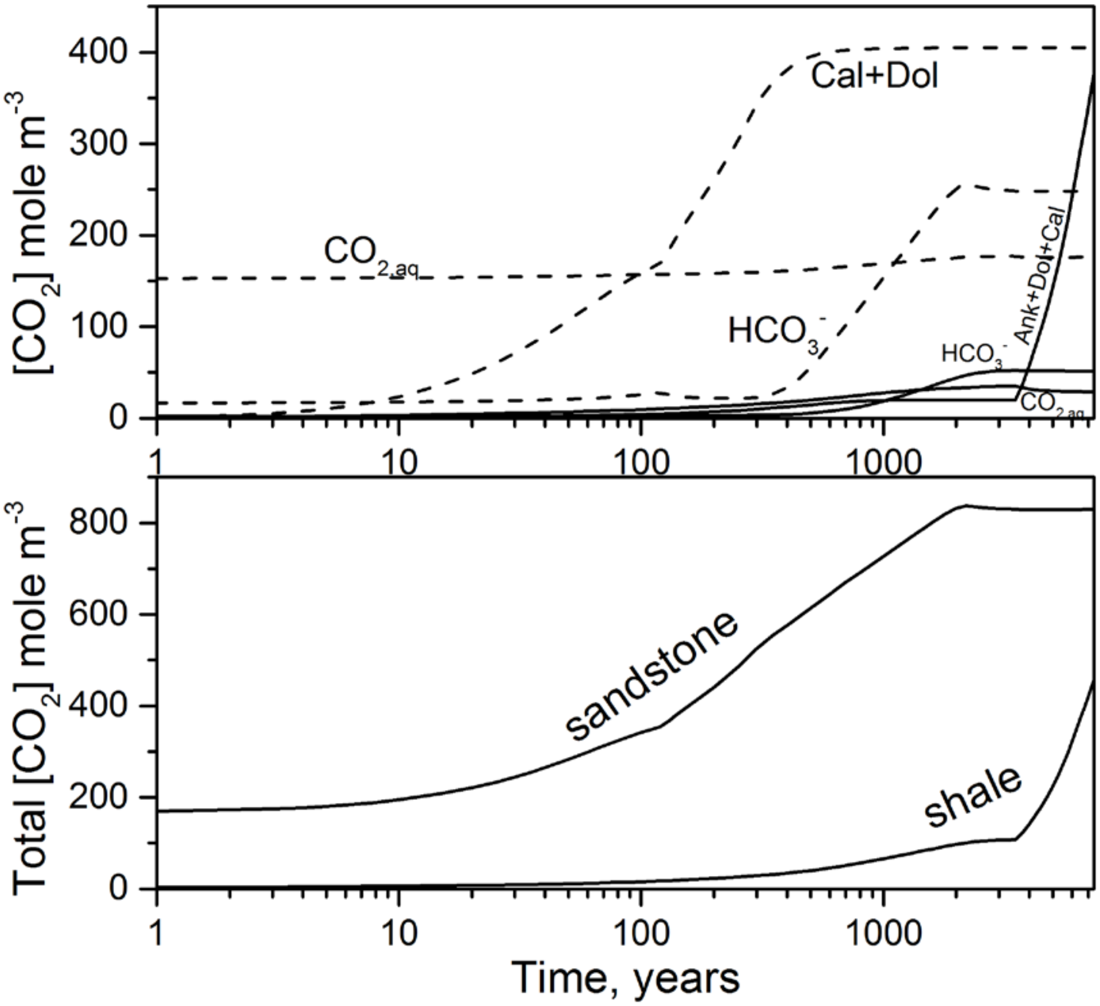

Figure 18: The average CO_2 accumulated per m^3 of the sandstone (2.5 m) and shale (5 m) layers versus time where dashed and solid lines correspond to sandstone and shale layers, respectively. Top graph: the lines show direct CO_2 dissolution into the aqueous brine, CO_2 dissolution with conversion into HCO_3^-, and CO_2 trapped as carbonates (ankerite, dolomite, calcite). Bottom graph: the lines correspond to total sums of accumulated CO_2 in sandstone and shale by these three mechanisms. The termination time (7,416 a) corresponds to the time when all the shale porosity is sealed at the ss/sh interface.

Different reactions take place in the shale layer. The average concentrations of CO_2 (mol per m^3) accumulated in the 0–5 m shale layer are plotted versus time in Figure 19 (top). The solubility trapping of CO_2 in the shale as $CO_{2,aq}$, HCO_3^- and, $CO_3^=$, is small in comparison to the sandstone because of the small porosity (Figure 19, top). Up to 3,500 years, the CO_2 that is trapped in the shale as a precipitate is mostly as dolomite. From 3,500 years to 7,416 years, intensive ankerite and dolomite precipitation is accompanied by calcite dissolution (Figure 19, top). The total CO_2

trapped in shale up until the termination time when the shale porosity is sealed at the ss/sh interface, is about two times less than the amount stored in the sandstone unit up to that time (Figure 19, bottom). Under the assumption that the whole sandstone layer is 100 m in thickness, the CO_2 trapped in the shale caprock would correspond to 1.3% of CO_2 stored in the sandstone reservoir.

4.3 REACTIVE ZONE IN SHALE

It is clear from Figure 16 that the reactions in shale seal the porosity at the ss/sh interface very close to the ss/sh contact. This reactive process happens because of the contrast in the sandstone and shale mineralogies, and especially because of the relatively high abundances of oligoclase and smectite in sandstone, and the relatively high chlorite content (> 5 %) in the shale. Porosity closure has often been noted at the interface of two rocks with mineralogical contrast during bimetasomatism (Zaraisky et al., 1986, 1989) and has been investigated previously (Balashov et al., 1991; Lichtner et al., 1998; Steefel and Lichtner, 1994).

For this problem, the important overall mineral-fluid reactions for sandstone and shale are summarized below. In sandstone there are three important acid-base reactions:

oligoclase dissolution

$$\begin{aligned}&\mathbf{Olg+1.2CO_{2,aq}+2.4H_2O\rightarrow}\\&\mathbf{0.2Ca^{2+}+0.8Na^{+}+1.2Al(OH)_{3,aq}+2.8SiO_{2,\mathit{aq}}+1.2HCO_3^{-}}\end{aligned}\qquad(22)$$

albite precipitation

$$\mathrm{Na^{+}+Al(OH)_{3,aq}+3SiO_{2,\mathit{aq}}+HCO_3^{-}\rightarrow Ab+H_2O+CO_{2,\mathit{aq}}}\qquad(23)$$

and albite dissolution to form kaolinite

$$\mathrm{Ab+CO_{2,aq}+1.5H_2O\rightarrow Na^{+}+0.5Kln+2SiO_{2,\mathit{aq}}+HCO_3^{-}}\qquad(24)$$

The important reactions that occur in both the sandstone and shale are as follows:

microcline dissolution

$$\mathrm{Mc+CO_{2,aq}+H_2O\rightarrow K^{+}+Al(OH)_{3,\mathit{aq}}+3SiO_{2,\mathit{aq}}+HCO_3^{-}}\qquad(25)$$

kaolinite replacement by illite and vise versa

$$3Kln+2K^{+}\ \rightarrow 2Ill+3H_2O+2H^{+}\qquad(26)$$

The main reaction in the shale is:

carbonation of chlorite and calcite dissolution

$$\begin{aligned}&\mathrm{Chl} + 4.5\mathrm{Cal} + 0.38\mathrm{SiO}_{2,aq} + 0.96\mathrm{K}^{+} + 0.96\mathrm{HCO}_3^{-} + 3.54\mathrm{CO}_{2,\mathrm{aq}} \rightarrow \\ &0.96\mathrm{Ill} + 3\mathrm{Ank} + 1.5\mathrm{Dol} + 0.12\mathrm{Gt} + 3.46\mathrm{H}_2\mathrm{O}\end{aligned} \qquad (27)$$

The onset of the last reaction at 3,600 years marks the beginning of formation of a reactive zone in the shale at the ss/sh interface. The spatial distributions of concentrations of $Al(OH)_{3,aq}$, Mg^{++}, Fe^{++} and Ca^{++} are represented as a function of time in Figure 19. After 3,500 years, Reaction 27 has not yet started and the sandstone brine still has greater concentrations of $Al(OH)_{3,aq}$, $Mg^{++}$and Ca^{++} than the shale, but the Fe^{++} molality is greater in the shale brine. At this time, the shale brine at the ss/sh interface is supersaturated with respect to ankerite (Figure 16b, top and middle).

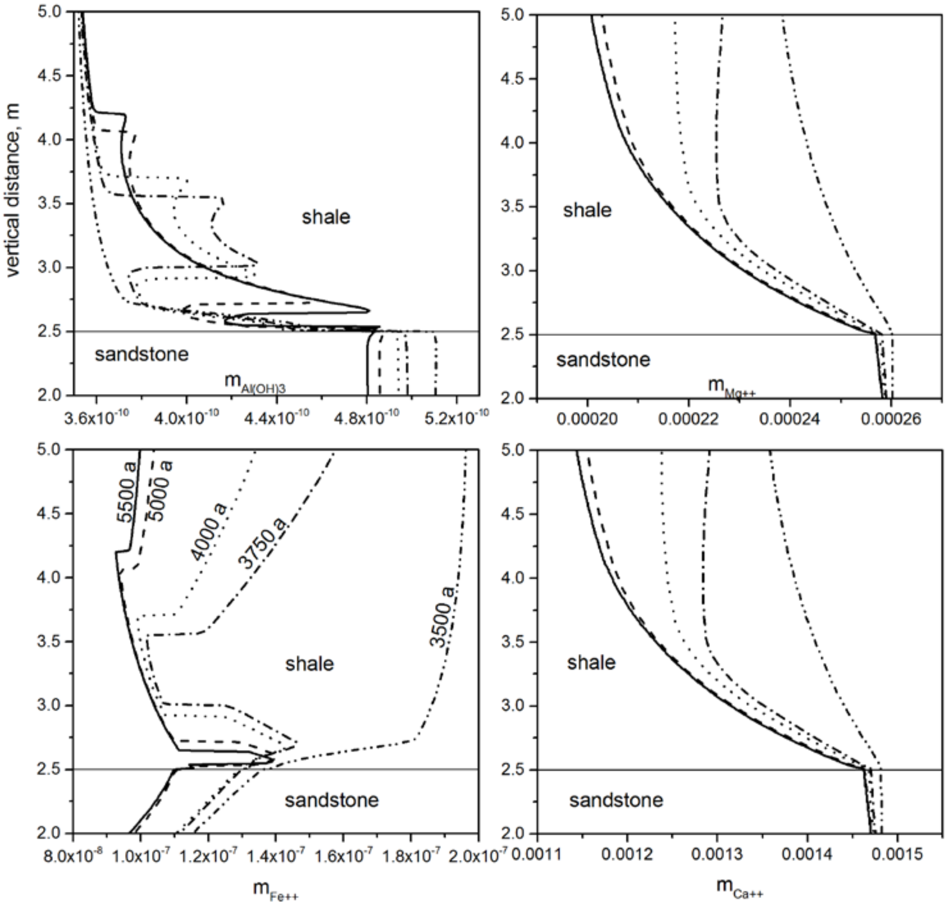

Figure 19: Plot of four primary aqueous species molalities ($Al(OH)_3$, Mg^{++}, Fe^{++}, Ca^{++}) versus vertical space coordinate for times 3,500, 3,750, 4,000, 5,000, and 5,500 a.

The volume change during Reaction 27 is positive and equal to 51.365 cm^3 per mole of Chl. However, this positive change can explain only 1.53% of the porosity decrease (initial 5% shale porosity) under the assumption that all the initial calcite in the shale (4.93 vol. %) reacts according to Reaction 27. Additional transport of Ca and Mg into the reactive zone of the shale is needed to explain the full porosity closure of the shale at the ss/sh interface (Figure 18).

Figure 19 shows counter diffusion occurring at the contact of the two rocks due to the different mineralogies. Reaction 27 is initiated by ankerite precipitation that started at a point 0.75 m in the shale inboard from the ss/sh interface (i.e., at vertical space coordinate 3.25 m, Figure 19). At 3,750 years, the reaction takes place within the interval 3–3.5 m and is marked by increasing $Al(OH)_{3,aq}$ and decreasing Fe^{++} concentrations (Figure 19). In this interval, ankerite is in local equilibrium with pore brine. The ankerite precipitation affects the spatial distributions of concentrations of Mg^{++} and Fe^{++} in a similar way. This is difficult to see in Figure 20 because the concentration of Mg^{++} is 1,000 times that of Fe^{++}. The rate of Reaction 27 is controlled by the kinetics of illite precipitation, and the transport of the reactive species in the brine is set by the reaction kinetics. This kinetic limitation is documented in Figure 18 for the case of Mg^{++} and Ca^{++} as a steepening of the concentration gradients in the interval between 3–3.5 m (Figure 19).

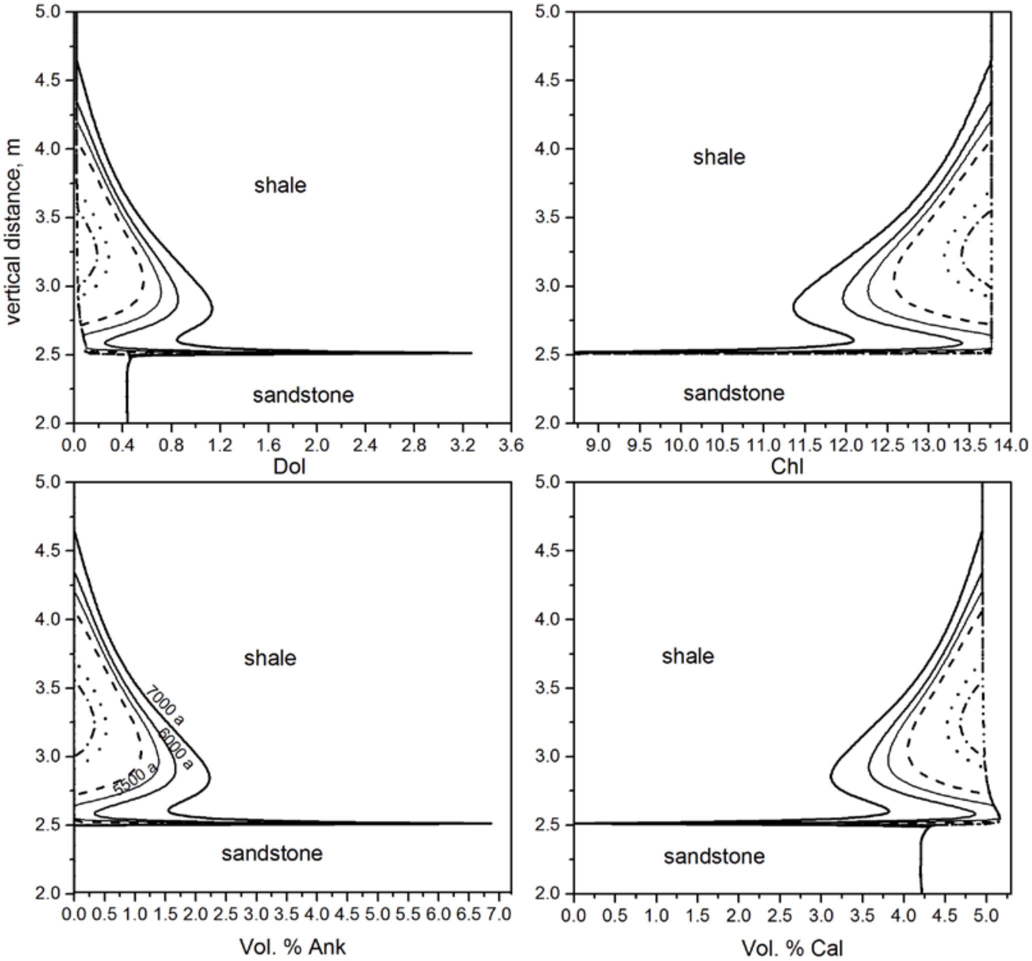

Figure 20: Mineral precipitation (ankerite, dolomite) and dissolution (chlorite, calcite) in the shale reactive zone between 3,500 and 7,000 years.

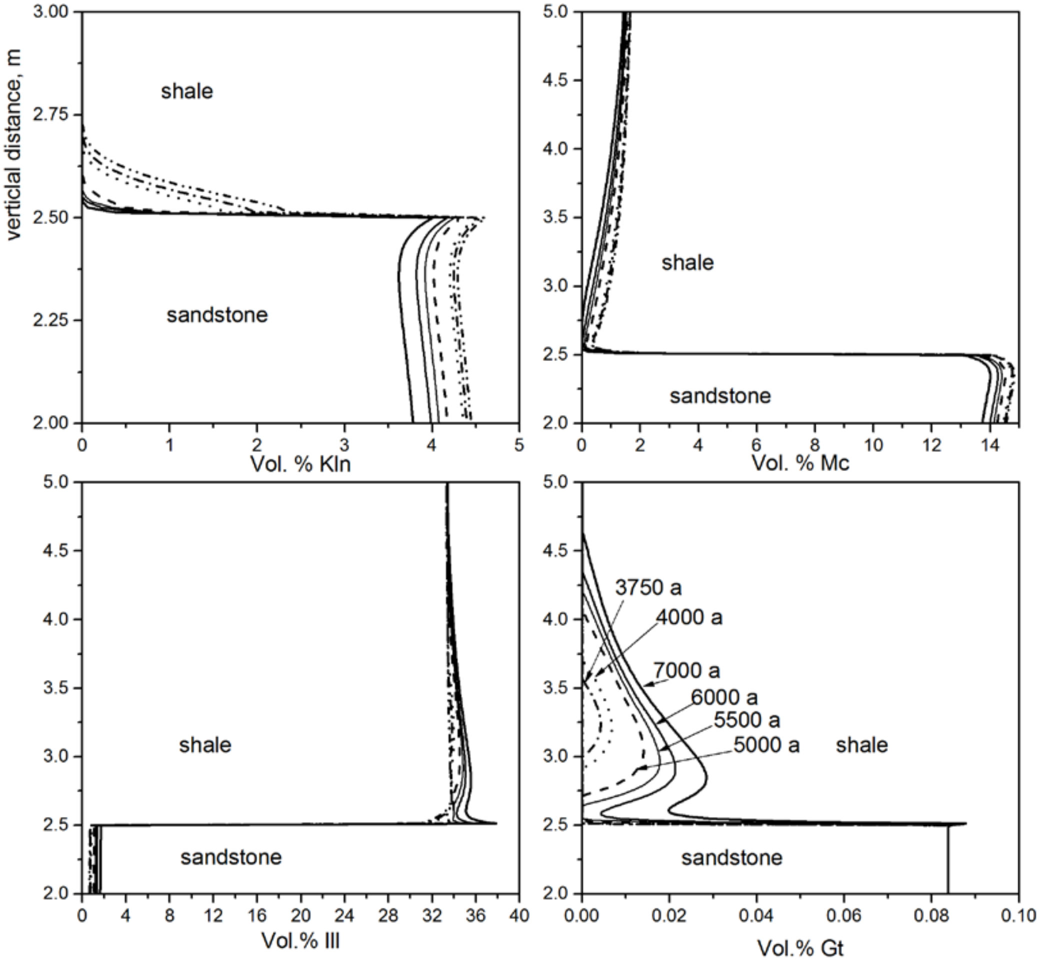

Figure 21: Mineral precipitation (illite, goethite) and dissolution (kaolinite, microcline) in the shale reactive zone and in the sandstone between 3,500 and 7,000 years.

The spatial distributions of minerals in the reactive zone are plotted as a function of time in Figures 20 and 21. From 4,000 years on, ankerite precipitates at the ss/sh interface on the shale side (Figure 20). This precipitation correlates with dolomite precipitation as well as chlorite and calcite dissolution (Figure 20), microcline dissolution and illite and goethite precipitation (Figure 21). The whole process proceeds after the Kln/Ill inversion at 2,000 years (Figure 21). Throughout, calcite, ankerite, dolomite, chlorite and goethite are all at local chemical equilibrium with brine, and microcline is very close to local equilibrium (Figure 17, 20, 21). Thus, the most important control on reaction progress is the kinetics of illite precipitation. The overall mineral reaction for the shale reactive zone can be expressed as the sum of Reactions 25 and 27:

$$\begin{aligned}&\mathrm{Chl}+4.5\mathrm{Cal}+0.96\mathrm{Mc}+4.5\mathrm{CO}_{2,\mathrm{aq}}\rightarrow\\&0.96\mathrm{Ill}+3\mathrm{Ank}+1.5\mathrm{Dol}+0.12\mathrm{Gt}+0.96\mathrm{Al(OH)}_{3,\mathrm{aq}}+2.5\mathrm{SiO}_{2,aq}+2.5\mathrm{H}_2\mathrm{O}\end{aligned} \tag{28}$$

The delay in onset of Reaction 27 is related to the delay in ankerite precipitation from the supersaturated fluid. This latter delay not only has a numerical basis in the model, but also is also related to the time dependence of the ankerite saturation index (Figure 16b, top and middle). Initially, ankerite is not present in the modelled system; however, as the system evolves it precipitates. To model minerals such as ankerite that precipitate but are not present at first, the mineral must be included in the initial system at a nominal concentration (here, 1 ppm in volume fraction units). According to Equation 18, the mineral specific surface area is calculated from the mineral volume fraction where the power changes from 2/3 to 5/3 for mineral volume fractions less than 1 ppm. In other words, the concentration of mineral grains at very small volume fractions is dependent on the mineral volume fraction. By using this algorithm for mineral appearance/disappearance, there was no delay in mineral precipitation for albite, kaolinite, dolomite, and goethite. The ankerite delay occurs because of its long period of strong undersaturation (600 years, Figure 19). During this period of undersaturation, its volume fraction drops well below 1 ppm, and a long time is required to reach the threshold 1 ppm fraction. Ankerite precipitation in the shale therefore begins at some distance from the ss/sh contact at a location where the threshold is reached first.

Although the model parameters of this mechanism are somewhat artificial, it makes physical sense that the ease of mineral precipitation depends on the initial concentration of a mineral (Steefel and VanCappellen, 1990; Lüttge et al., 2013). Second, ankerite formation in sedimentary rocks in some cases is delayed (Na et al., 2011), or reflects difficulty in nucleation (Milliken, 2002; Adabi and Rao, 2003). In some cases, dolomite may act as a precursor mineral (Ferry et al., 2009). Likewise, modeling here shows that dolomite precipitation takes place and always accompanies ankerite precipitation (Figure 21).

The bimodal ankerite precipitation resembles Liesegang banding (Lebedeva et al., 2004). For example, at 5,000 years and 5,500 years (Figure 22), two ankerite bands are predicted near and far from the ss/sh interface.

4.4 VARIATION OF THE TRANSPORT PROPERTIES OF THE SHALE POROUS MEDIUM

Rock porosity, effective rock diffusivity and permeability are important physical factors determining CO_2 storage. These parameters are reservoir-specific and can vary significantly within a reservoir. Fick's first law for diffusion through porous media for one dimension is

$$j=-F_{inv}D_{aq}\frac{\partial c}{\partial x} \tag{29}$$

where j is diffusion flux per 1 m^2 of rock cross section in units [mole $m^{-2}s^{-1}$], D_{aq} - diffusion coefficient in pore solution [m^2s^{-1}]. The geometrical effects of pore connectivity, effective pore cross section, and pore tortuosity are generally modeled using the inverse of the Archie formation factor F_{inv}. The dependence of F_{inv} on porosity (ϕ) can be represented as the Archie power law (Archie, 1942; Brace, 1977):

$$F_{inv} = \alpha\phi^{n_F} \tag{30}$$

In general, the mass balance and kinetic equations for reactive diffusion takes the form

$$\begin{aligned} &\phi\frac{\partial c}{\partial t} + \frac{\partial \rho_{\min}}{\partial t} = \frac{\partial}{\partial x}\left(F_{inv}D_{aq}\frac{\partial c}{\partial x}\right) \\ &\frac{\partial \rho_{\min}}{\partial t} = -I_{\min} \end{aligned} \tag{31}$$

where $\rho_{\min}$ comprises the concentration of the component of interest in minerals, and $I_{\min}$ follows from Equation 15.

Here this factor is approximated as $F_{inv} = \dfrac{\phi^{n_F}}{\theta_\tau}$, with tortuosity coefficient $\theta_\tau = \pi/2$ for packed spheres, n_F is equal to 1 for sandstone, and 1.5 for shale. The “standard” $n_F = 1.5$ is based on data for igneous rocks of low permeability (Zaraisky and Balashov, 1995; Balashov and Zaraisky, 1982). At a sandstone porosity of 0.25, and shale porosity of 0.05, the inverse factor equals 0.16 and 0.007 for sandstone and shale, respectively, with a ss/sh ratio 22.7. The F_{inv} value for shale is in a good correspondence with reported measurements around 0.004 for caprocks of 6% porosity (Fleury et al., 2009; Berne et al., 2010).

Equations 31 have important space/time scaling properties (Balashov and Lebedeva, 1989; Lichtner, 1993). Namely, if the linear transformation of *x*, *t* – variables (Lichtner, 1993)

$$\begin{aligned} x' &= ax \\ t' &= bt \end{aligned} \tag{32}$$

where *a* and *b* are positive real constants, is applied to the system of equations in Equations 31, and the initial and boundary conditions of Equations 31 are invariant to this transformation, then the solution of the system in Equations 31 $f(x,t) = \{c(x,t), \rho_{\min}(x,t)\}$ is invariant to the next scaling relation

$$f\left(x,t;k_{\min},F_{inv}D_{aq}\right) = f\left(x',t';\frac{k_{\min}}{b},\frac{a^2}{b}F_{inv}D_{aq}\right) \tag{33}$$

Imagine a sandstone contact with a semi-infinite shale layer and assume that the pore concentrations at the ss/sh boundary are constant. The use of Equations 33 in this semi-infinite case of ss/sh contact is straightforward. Applying this scaling relation Equations 33 at *a* > 0 and *b* = 1

$$f\left(x,t;k_{\min},F_{inv}D_{aq}\right) = f\left(ax,t;k_{\min},a^2F_{inv}D_{aq}\right) \tag{34}$$

From Equation 34 it immediately follows that for 0 < a < 1 the change in the inverse Archie factor (IAF) from IAF = F_{inv} to IAF = a^2F_{inv} will result in a contraction of the reactive zone in the shale by a value equivalent to the multiplier a. It is clear that this reactive zone contraction will not change the time of porosity sealing at the ss/sh interface (x = 0). The new IAF corresponds to decreased coefficient $a^2\alpha$ instead of α in Archie law (Equation 30).

In the computed model simulation of the ss/sh contact, the shale layer has a finite thickness L_{sh} . Thus, the boundary conditions of problem (Equation 31) at L_{sh} depend on the linear transformation (Equation 32): in other words, the scaling relation (Equation 34) is not rigorously maintained.

The standard definition of the characteristic dimensionless time for diffusion, $\overline{t} = \frac{D_{sh}t}{L_{sh}^2}$, shows that the multiplication of effective diffusion coefficient $D_{sh} = F_{inv}D_{aq}$ on the constant number a^2 is equivalent to L_{sh} division on number $\sqrt{a^2} = a$. This means that, for example, IAF can decrease by a factor of 9, or maintain IAF constant and increase the thickness of shale layer by a factor of 3 with the same resultant effect. Thus, multiplying IAF by $a^2 < 1$ will move the problem (Equation 31) with a finite L_{sh} closer to the limiting problem for the semi-infinite shale layer. In this case, the time for porosity closure at the ss/sh interface will tend to its constant value at the semi-infinite shale layer.

Changes in the value of n_F in (Equation 30) results in a more intrinsic and complicated influence on reactive diffusion —this is because porosity is itself a function of time and space. An increase in n_F will not only decrease the IAF according to Archie’s law (Equation 30) but will also increase mineral precipitation rates at the ss/sh interface.

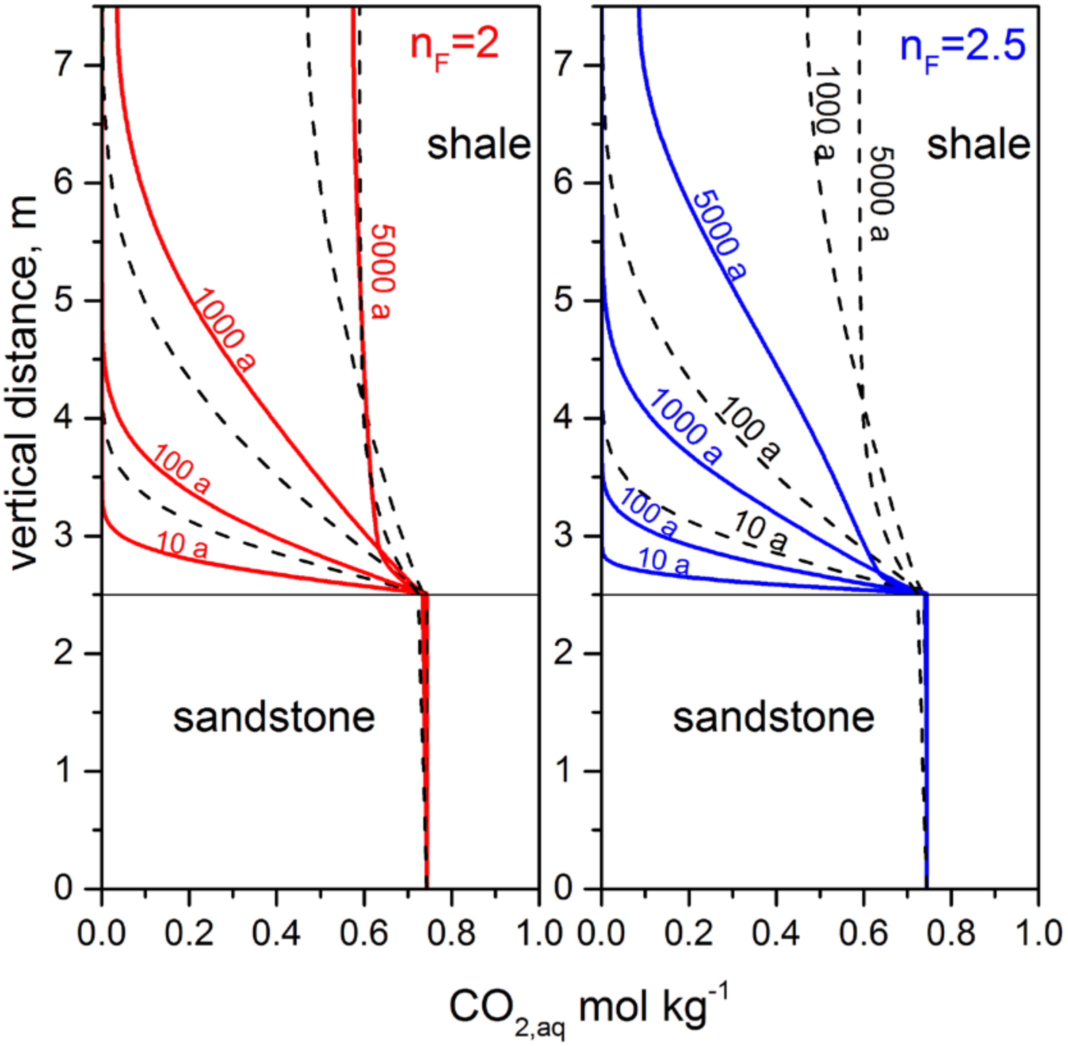

Figure 22: Profiles showing vertical distributions through the sandstone and shale for molecular $CO_{2,aq}$/mol kg-1 dissolved in brine for nF = 2 (left side), and nF = 2.5 (right side) for different times. The dashed lines correspond to the standard nF = 1.5.

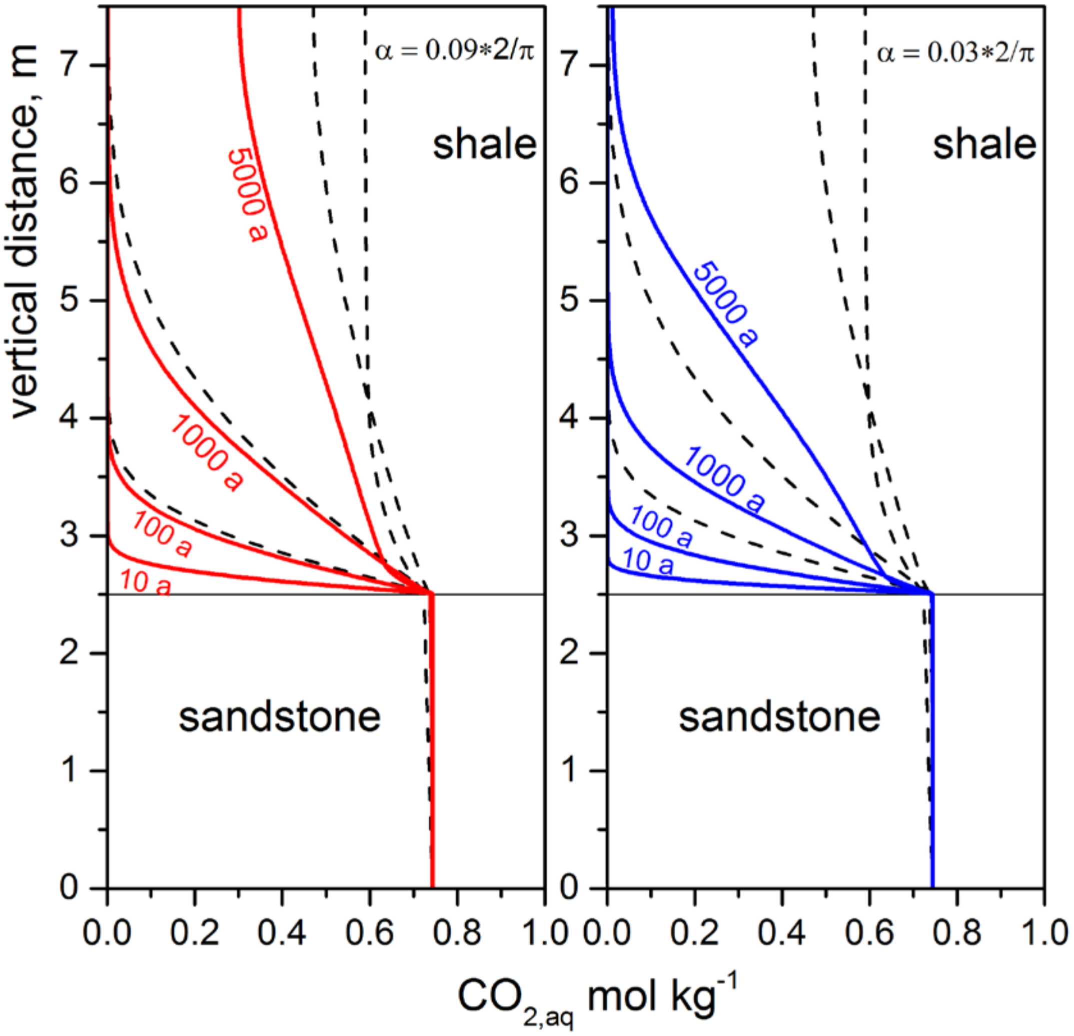

Figure 23: Profiles showing vertical distributions through the sandstone and shale for molecular $CO_{2,aq}$/mol kg-1 dissolved in brine at α = 0.09×2/π (left side), and α = 0.03×2/π (right side) for different times. The dashed lines correspond to the standard case, α = 2/π.

The effects of n_F and α in Equation 30 on the propagation of $CO_{2,aq}$ into the brine in the shale for various time intervals are represented in Figures 22 and 23, respectively. The dashed lines in these Figures correspond to the standard case with $\alpha =$ 2/π and n_F =1.5. All computed curves (Figures 22) show strong retardation of $CO_{2,aq}$ propagation into the shale with roughly equal effects for n_F =2 at $\alpha =$ 2/π and $\alpha =$ 0.09×2/π at n_F =1.5, and for n_F =2.5 at $\alpha =$ 2/π and $\alpha =$ 0.03×2/π at n_F =1.5.

As expected, the termination time of porosity sealing at the ss/sh interface increases when α decreases. By extrapolation, the termination time of complete sealing of porosity at the ss/sh interface for the semi-infinite shale layer equals ~ 17,000 years.

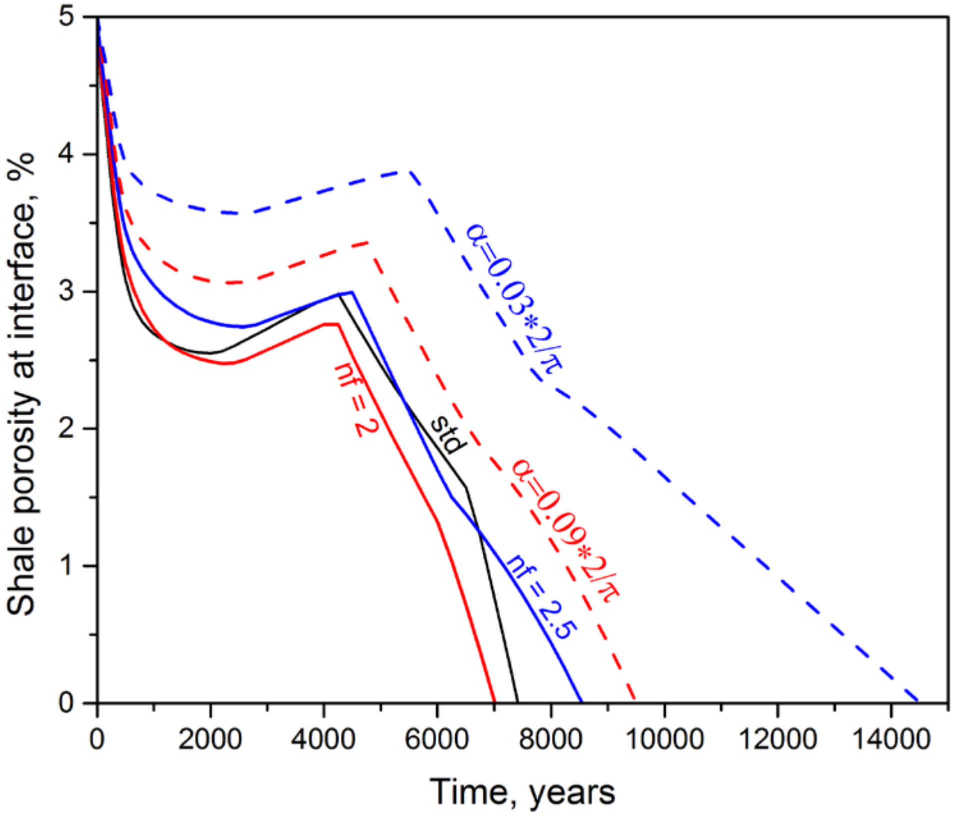

Figure 24: The porosity closure curves at varying parameters in Archie law for formation factor.

In accordance with above qualitative analysis the different times of porosity closure at ss/sh interface, namely, 7,416, 7,000 and 8,500 years, were observed at n_F varying as 1.5, 2 and 2.5, respectively (Figure 23). For uniform porosity 5% the effects for $n_F = 2$ and $n_F = 2.5$ correspond to new α -s at standard $n_F = 1.5$: 0.22×2/π and 0.05×2/π, respectively. Figure 21 shows that is indeed the way of ordering of $CO_{2,aq}$ propagation curves. With calcite full dissolution in shale at ss/sh interface the rate of ankerite precipitation decreases. The n_F increasing at constant α leads to greater focusing of reactive process at ss/sh interface. This is especially clear from shale porosity at ss/sh interface time dependencies at varying parameters (Figure 23) and from shale reactive zone dynamics in vertical space dimension (Figure 24). In Figure 24 the ankerite was used to mark the expansion of reactive zone in shale with time. In all cases mineral alteration in shale takes place in coherent way of Reactions 27–28. In either way of

n_F increase or α decrease the contraction of reactive zone in shale is observed comparatively to the standard case (Figure 24).

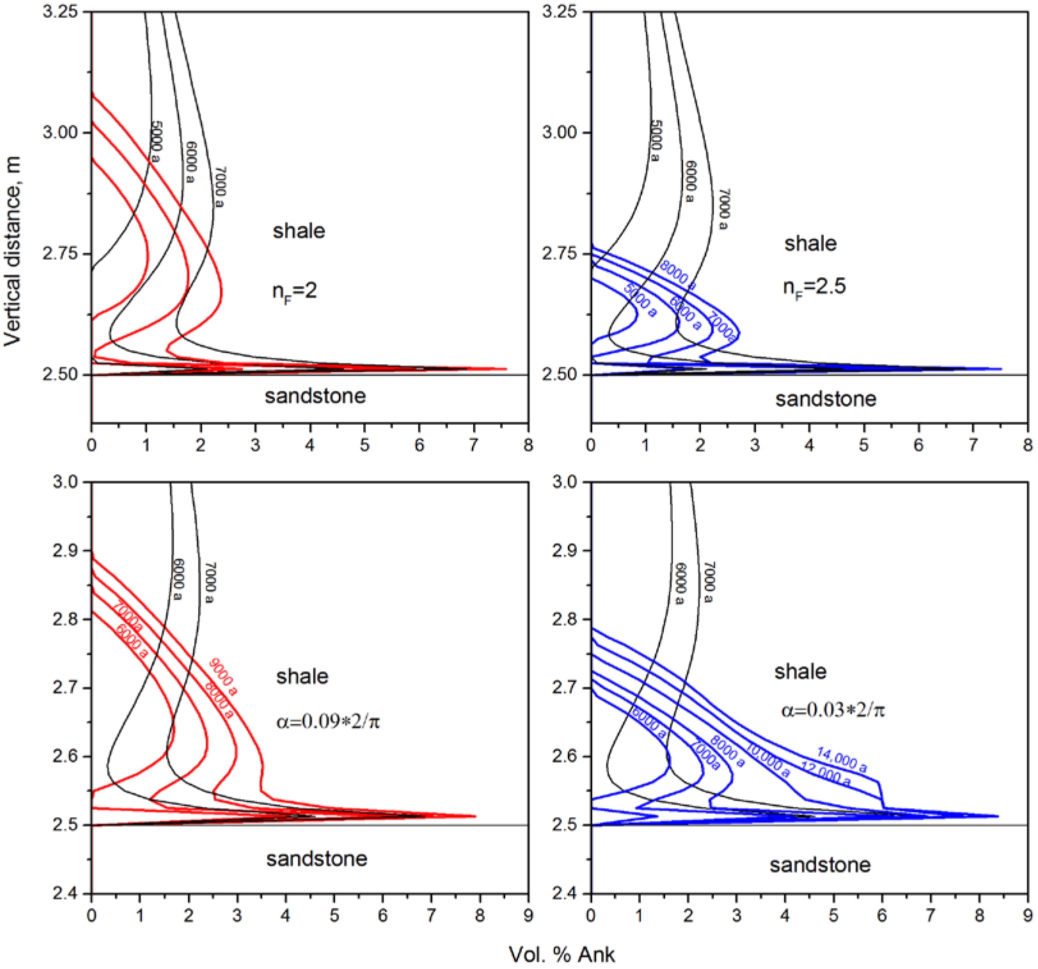

Figure 25: Transformation of shale reactive zone (tracked by ankerite profile) in result of parameter variation in Archie law for formation factor. Left top n_F = 2, right top n_F = 2.5; left bottom α = 0.09×2/π, right bottom α = 0.03×2/π. The standard lines correspond to α = 2/π, and n_F = 1.5

The responses of the CO_2 accumulation in shale to the shale porous medium parameters varying are represented in Figure 25. An essential decrease of CO_2 accumulated in shale (less than 50% of standard shale storage) to time of porosity closure at interface ss/sh was observed for all variations of α and n_F (Figure 25). Shale with low pores connectivity n_F =2.5 demonstrates the most favorable behavior in caprock role. Although the CO_2 accumulation is less in each of three different mechanisms of CO_2 shale storage, the largest effects are observed for mineral trapping.

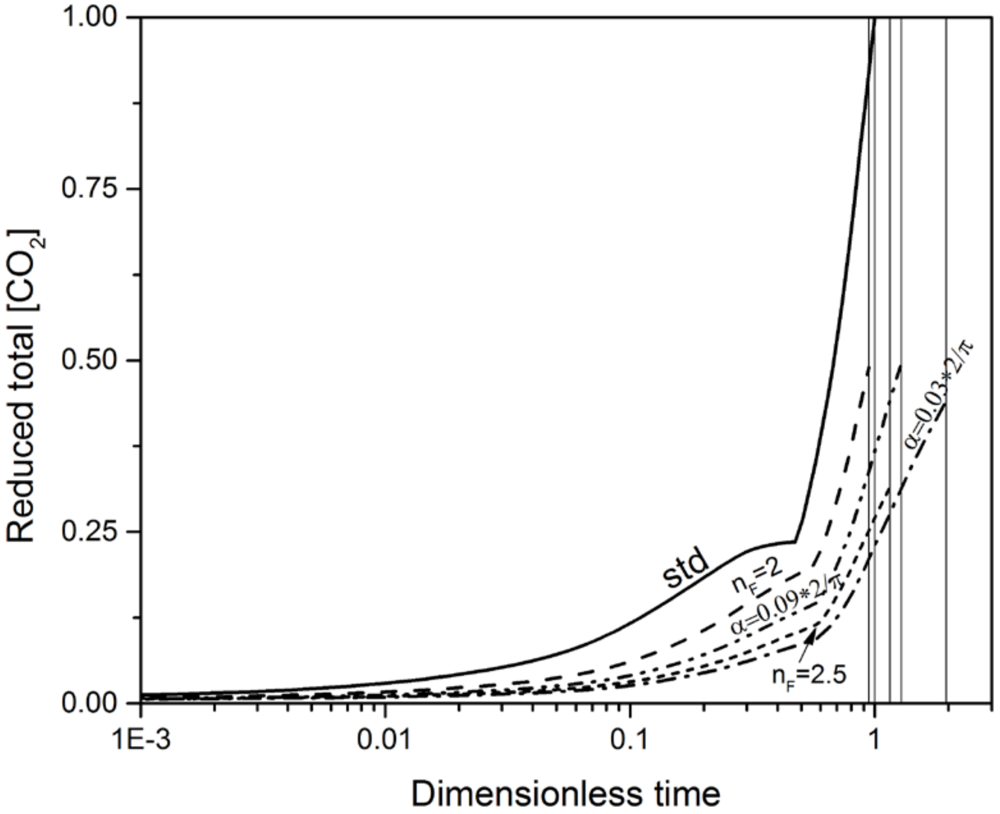

Figure 26: The time dependence of total relative CO_2 abundance accumulated in shale until terminal time at varied parameters of Archie law. Solid line, standard case $\alpha = 2/\pi$, $n_F = 1.5$; dash line, $\alpha = 2/\pi$, $n_F = 2$; dash-two-dots line, $\alpha = 0.09\times2/\pi$, $n_F = 1.5$; short dash line $\alpha = 2/\pi$, $n_F = 2.5$; dash-dot line $\alpha = 0.03\times2/\pi$, $n_F = 1.5$. In all cases the decrease of effective diffusion coefficient leads to decrease of CO_2 accumulation, and, consequently to the higher sustainability of ss/sh contact. The vertical lines show the different relative terminal times.

4.5 VARIATION IN MINERAL KINETICS

Five minerals are not maintained at local chemical equilibrium during reactions at the ss/sh interface (Figure 19): quartz, albite, microcline, kaolinite, and illite. Given that quartz is always maintained in excess and its kinetic constant is small and well constrained (Palandri and Kharaka, 2004), its kinetic constant was not varied. However, a sensitivity analysis was carried out to determine the effect of variations in the rate constants for feldspars and clay minerals as shown in Figure 28. Variations in the feldspar kinetic constants have only a minor influence on the evolution of porosity closure. In contrast, variation in the kaolinite constant demonstrates a profound effect: when the Kln kinetic constant is increased by a factor of 10 (Kln×10), porosity closure occurs at 107 years instead of 7,416 years.

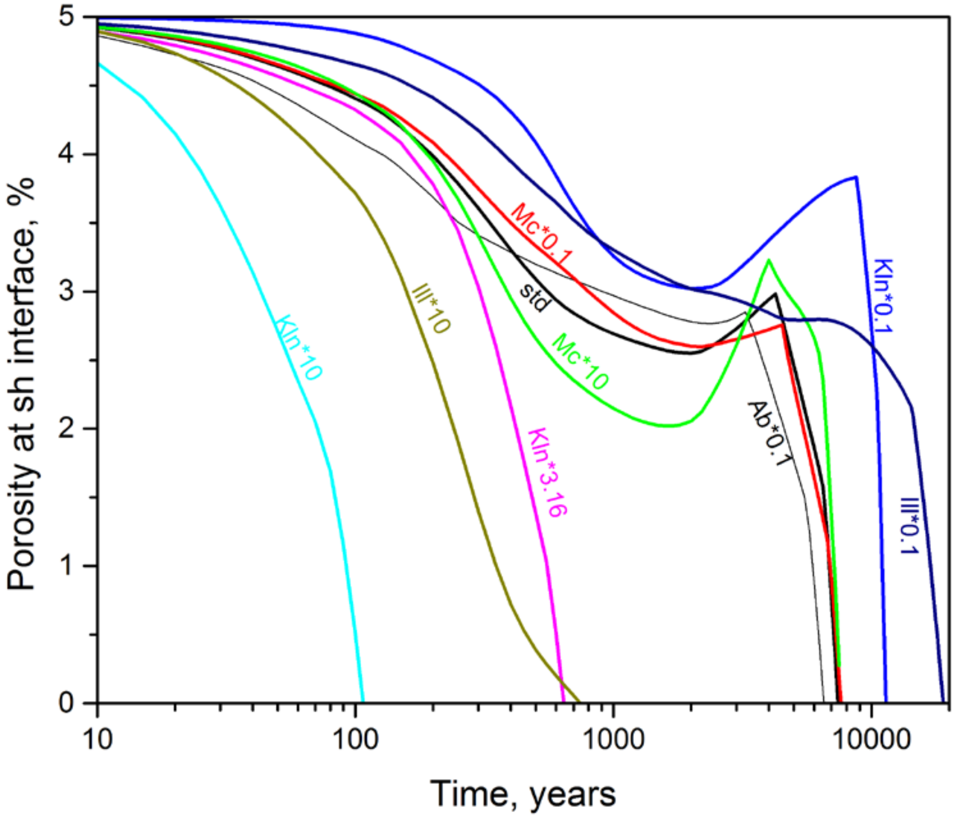

Figure 27: The shale porosity evolution in the point of contact with sandstone in simulations using varying mineral kinetic constants.

As shown in Figure 26, for most cases including the standard simulation, the initial decrease in shale porosity at the interface occurs because kaolinite precipitates and illite dissolves. This reaction (Reaction 26) continues until ~ 2,000 years, when illite precipitation and kaolinite dissolution begins and is accompanied by an increase in porosity. Eventually, ankerite precipitation becomes fast enough and Reaction 27 begins, leading to porosity closure (Figures 16b, 25). This general behavior with respect to porosity closure changes in simulations using higher kinetic constants for the clay minerals (discussed later).

To compare the results from the sensitivity tests, it is convenient to use a dimensionless time variable defined as

$$\bar{t} = \frac{t}{t_{std}} \qquad (35)$$

where t_{std} = 7,416 years is the standard termination time (STT), i.e. the time when the porosity at the ss/sh interface disappears for the standard simulation. The dimensionless quantities of stored CO_2 are defined as

$$\begin{aligned} \bar{S}_{CO_2,aq} &= \frac{[CO_{2,aq}]}{[CO_{2,aq}]_{std}} \\ \bar{S}_{HCO_3^-} &= \frac{[HCO_3^-]}{[HCO_3^-]_{std}} \\ \bar{S}_{CO_2,\min} &= \frac{[CO_{2,\min}]}{[CO_{2,\min}]_{std}} \\ \bar{S}_{CO_2,tot} &= \frac{[CO_{2,tot}]}{[CO_{2,tot}]_{std}} \end{aligned} \tag{36}$$

In the last equation, $[CO_{2,aq}]_{std}$ = 28.79 mol m^{-3}, $[HCO_3^-]_{std}$ = 51.16 mol m^{-3}, $[CO_{2,\min}]_{std}$ = 376.9 mol m^{-3}, and $[CO_{2,tot}]_{std}$ = $[CO_{2,aq}]_{std} + [HCO_3^-]_{std} + [CO_{2,\min}]_{std}$ = 456.85 mol m^{-3}. These values are concentrations of CO_2 dissolved in brine per m^3 of shale, HCO_3^- and $CO_3^=$ dissolved in shale brine, CO_2 trapped in carbonates, and total CO_2 stored in shale at the termination time, respectively, in the standard reactive simulation.

4.5.1 The Effects of Variations in the Feldspar Kinetic Constants

Variations in the Ab kinetic constant only affects CO_2 storage in the shale to a minor extent because Ab reactions mostly take place in the sandstone (Balashov et al., 2013). The main influence of variations in the Ab reaction kinetics in the progress of mineral reactions at the contact are related to the pH of the sandstone pore solution during Ab precipitation/dissolution. This effect is not significant with respect to the CO_2 accumulation in the shale.

In contrast to Ab, the kinetic constant for Mc has a greater effect on CO_2 storage in the shale because microcline participates in Reaction 28. When the microcline kinetic constant is decreased 10 times less than its standard value (Mc×0.1), Reactions 25 and 28 decrease in rate. This leads to an increase in the porosity closure time (1.025×STT) and a 40% decrease in CO_2 accumulation in the shale by this time.

4.5.2 The Effects of Variations in the Clay Mineral Kinetic Constants

4.5.2.1 Kaolinite Kinetic Constant

Taking into account the strong effect of the kaolinite kinetic constant on CO_2 propagation into the shale, calculations were completed for seven different values of the Kln kinetic constant. The ratios of the Kln kinetic constant (k_{Kln}) to its standard value (k_{Kln}^{std}) were 0.1, 0.316, 0.562, 1, 1.78, 3.16, 10 (i.e., $\log \frac{k_{\mathrm{Kln}}}{k_{\mathrm{Kln}}^{std}}$ = -1, -0.5, -0.25, 1, 0.25, 0.5, 1) as shown in Figure 26. The vertical lines in Figure 27 show the times where the porosity closes. The CO_2 accumulation line is practically the same (within 15%) for all values of the Kln kinetic constant (Figure 27). However, variation in the kaolinite kinetic constant causes a large range in the times of porosity closure (Figure 26) from 107.5 years at (Kln×10) to 11,370 years at (Kln×0.1). The maximum amount of CO_2 accumulation in the shale increases as the Kln kinetic constant decreases. At a kinetic constant Kln×0.1 this amount is 60% above the standard value (Figure 27).

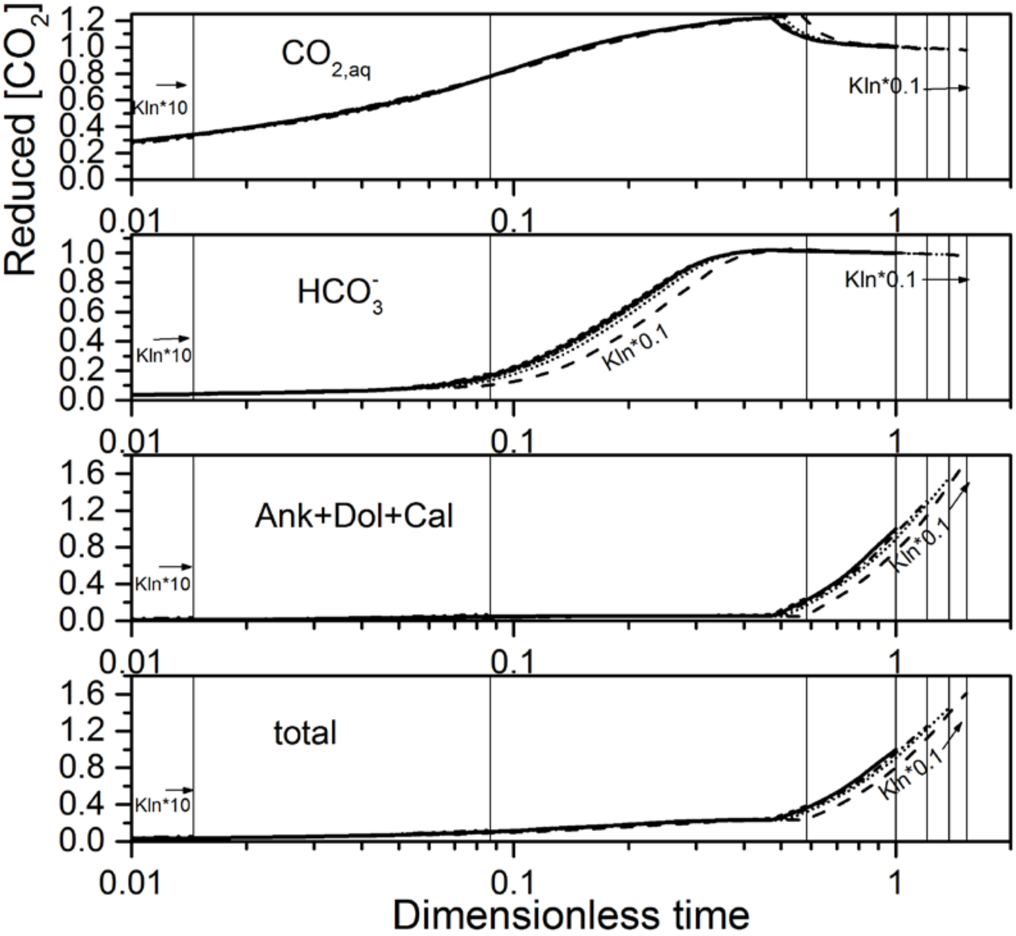

Figure 28: The time dependence of the relative abundance of CO_2 accumulated in the shale through different mechanisms of CO_2 sequestration (storage) calculated assuming different values of the Kln kinetic constant. From top to bottom: molecular CO_2 dissolved in brine; CO_2 dissolved in brine as HCO_3^- and $CO_3^=$; CO_2 trapped in carbonates, and total CO_2 trapped in shale. The vertical lines show the relative termination times for different values of the kaolinite relative kinetic constant, from left to right: 10, 3.16, 1.78, 1, 0.562, 0.316, and 0.1.

The effect of variation in the Kln kinetic constant on the mineral saturation evolution at the shale thin layer (0.0125 m) at the ss/sh interface is shown in Figure 27. Vertical lines in Figure 28 document the termination times of porosity closure for a Kln kinetic constant equal to Kln×10, for the standard value, and for Kln×0.1. For the standard Kln kinetic constant, Reaction 27 begins at ~ 4,000 years with ankerite precipitation, whereas at (Kln×0.1) the same reaction begins at ~ 8,500 years. In contrast, at Kln×10 the chlorite carbonation begins at ~ 5 years in accordance with other reaction:

$$\begin{aligned}&\mathrm{Chl} + 4.5\mathrm{Cal} + 0.38\mathrm{SiO}_{2,aq} + 4.5\mathrm{CO}_{2,\mathrm{aq}} \rightarrow \\ &1.44\mathrm{Kln} + 3\mathrm{Ank} + 1.5\mathrm{Dol} + 0.12\mathrm{Gt} + 2.5\mathrm{H_2O}\end{aligned} \qquad (37)$$

In this case at Kln×10 pore fluid is supersaturated by ankerite already in first few years of reactive process. Reaction 37 replaces Reaction 27 because at this time (~ 5 years) the pore interface fluid is supersaturated with respect to kaolinite and undersaturated with respect to illite (Figure 28). It is clear that kaolinite and illite are kinetically coupled with each other (Figure 28, middle). The increase of kaolinite kinetic constant “attracts” the saturation curve of this mineral to local equilibrium line, and “repulses” the illite saturation curve from equilibrium. In the opposite way, when kaolinite kinetic constant decreases its saturation curve deviates from equilibrium and illite saturation curve becomes very close to equilibrium line (Figure 28, middle). The quartz saturation curve is influenced by kaolinite kinetic constant intensively until 100 years (Figure 28, bottom), the fluid silica activity increases corollary with kaolinite kinetic constant. It happens because of acceleration of oligoclase dissolution in sandstone at the expense of kaolinite precipitation.

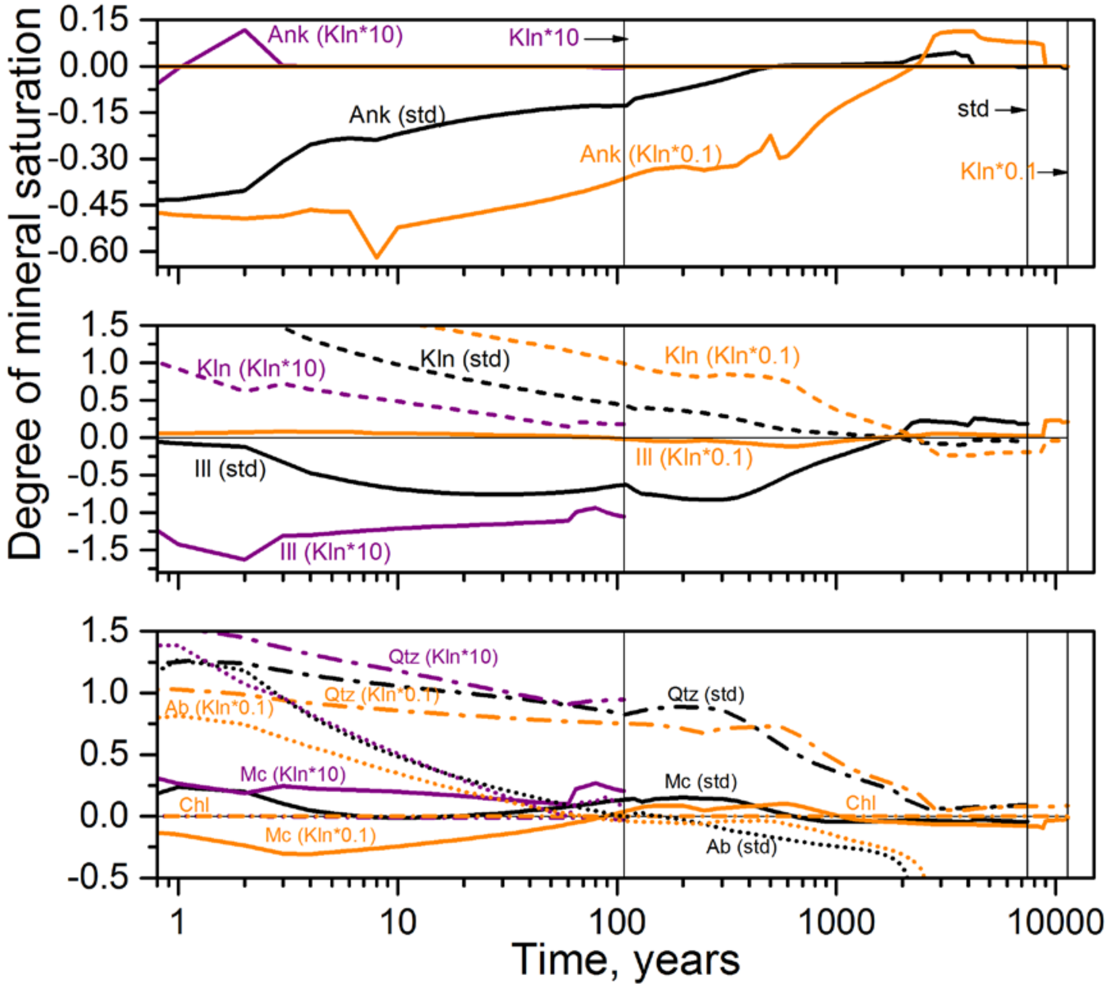

Figure 29: The evolution of mineral saturations in shale at interface ss/sh under conditions of kaolinite kinetic constant varying. The evolution of ankerite saturation is represented on top figure for the kaolinite kinetic constant 10 times greater than standard constant, the standard kinetic constant, and the kaolinite kinetic constant 10 times less than standard one. The calcite and dolomite saturations correspond to the zero line. The saturation time profiles for kaolinite (dash) and illite (solid) are plotted in middle figure. The saturation time profiles for quartz (long dash – dot), albite (dot), microcline (solid), and chlorite (dash-dot) are plotted in bottom figure. The vertical lines show the terminal times for different values of kaolinite relative kinetic constant, from left to right: 107.5, 7416, and 11,370 years for relative constant 10, 1, and 0.1, respectively.

The greater kaolinite kinetic constant leads to more intensive Kln precipitation, the system responds with more intensive illite dissolution, hence the greater illite undersaturation (Figure 28). Simultaneously, the silica activity increases because of reactions in the sandstone. Furthermore, because the K^+ activity stays constant, the alumina activity in the pore fluid decreases (Figure 29, left) to balance illite dissolution and kaolinite precipitation according to Reaction 37. Importantly, chlorite is always maintained very close to local chemical equilibrium with the pore fluid, and the decrease of alumina activity therefore leads to an increase in the Fe(II) activity in solution $a_{Fe^{++}}(a_{H^+})^{-2}$ (Figure 28, middle). The increase in $a_{Fe^{++}}(a_{H^+})^{-2}$ leads after 2 years to supersaturation of the fluid in ankerite, and during 5–107 years to continuous ankerite precipitation (Figure 28 and 29) finally with porosity closure at interface. Thus, at a high kaolinite kinetic constant, Reaction 37 is triggered by low alumina activity in pore solution.

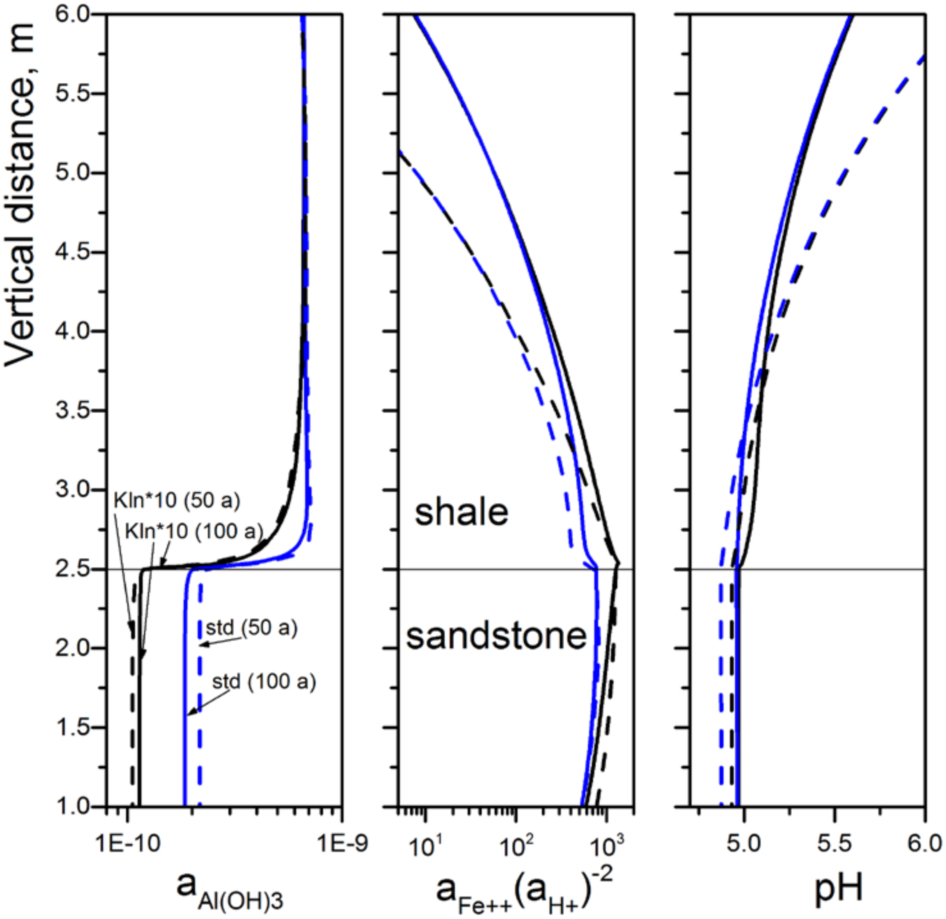

Figure 30: The activities of primary dissolved aqueous species ($a_{Al(OH)3}$ and principal iron (II) activity) and pH plotted versus vertical distance at ss/sh contact (50 and 100 years) for the case of high kaolinite kinetic constant (10 times the standard value) in comparison with standard kinetic case. The decrease of alumina activity in brine is accompanied by increase of iron (II) activity in brine.

A similar situation is observed for Kln×3.16. An important change occurs at 400–700 years when ankerite precipitation is triggered by lowering of silica activity instead of alumina activity with consequent increase of $a_{Fe^{++}}(a_{H^+})^{-2}$.

The case of a low value of the kaolinite constant (Kln×0.1) is similar to the standard simulation. Once again, an increase in the Fe(II) activity $a_{Fe^{++}}(a_{H^+})^{-2}$ occurs along with a decrease in the alumina activity and at 7,000 years the solution is supersaturated by ankerite (Figure 28, top).

The simulations showed that variations of the Kln kinetic constant lead to variations in alumina–silica activities in the shale pore solution at the ss/sh interface. At chlorite local equilibrium with pore solution these activity variations change the Fe(II) activity $a_{Fe^{++}}(a_{H^+})^{-2}$, which in turn influences the ankerite degree of saturation. The beginning of ankerite precipitation triggers the total carbonation Reactions 27 and 37.

4.5.2.2. Illite Kinetic Constant

The effects of variations in the illite kinetic constant on CO_2 accumulation in the shale are represented in Figure 30. The general scheme is similar to those described for the Kln kinetic constant. The effects manifest mainly in differences in the times of porosity closure. For example, the termination time at (Ill×10) is equal to 744.5 years, and at low kinetic constant (Ill×0.1) – 18,990 years. Additionally, CO_2 accumulation at (Ill×0.1) shows 30% lower values of CO_2 accumulation compared to the standard simulation at 7,416 years (Figure 30, bottom). This occurs at the expense of mineral trapping.

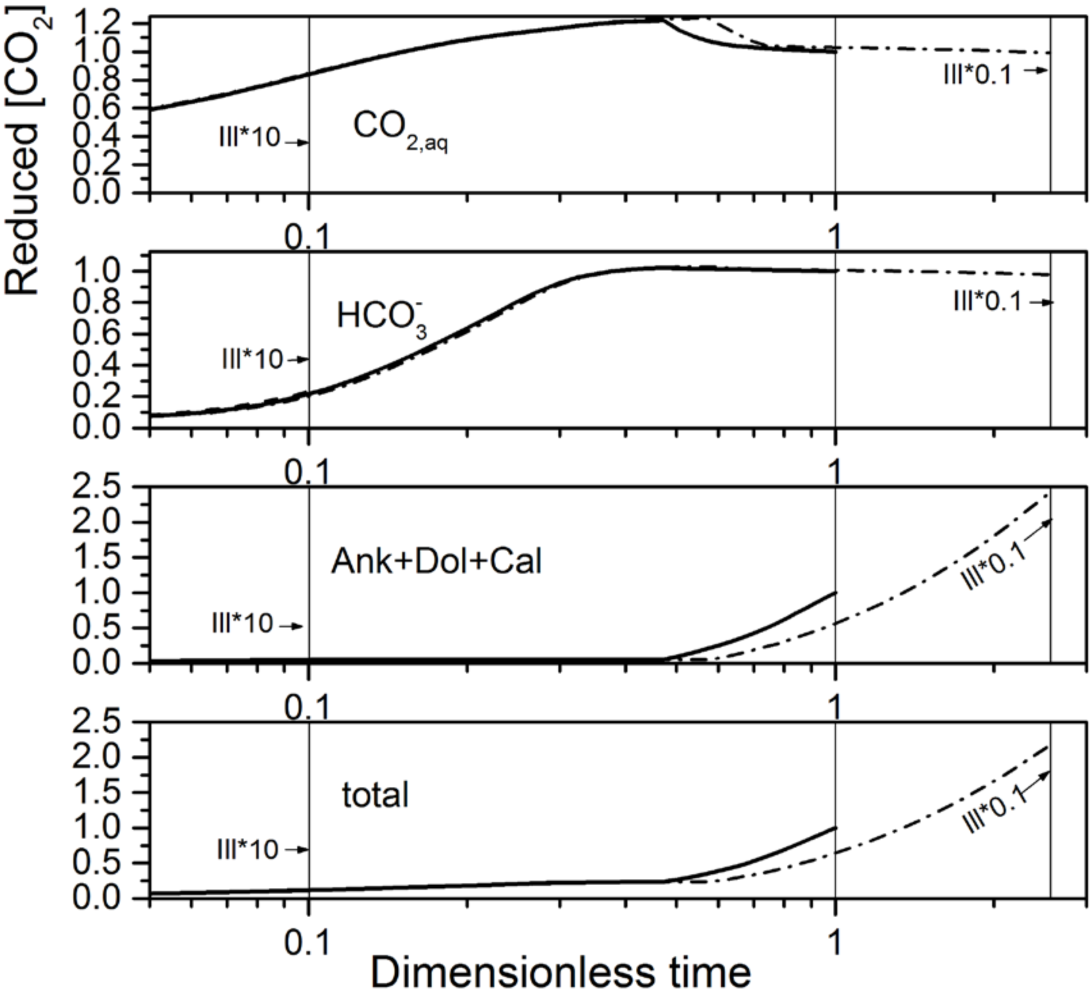

Figure 31: The time dependence of relative CO_2 abundance accumulated in shale through different mechanisms of CO_2 sequestration (storage) at various values of the illite (Ill) kinetic constant. From top to bottom: molecular CO_2 dissolved in brine; CO_2 dissolved in brine as ionic forms HCO_3^- and $CO_3^=$; CO_2 trapped in carbonates, and total CO_2 trapped in shale. The vertical lines show the relative termination times for different values of the illite relative kinetic constant, from left to right: 10, 1 and 0.1. The corresponding times in years are 744.5, 7,416 and 18,990, respectively.

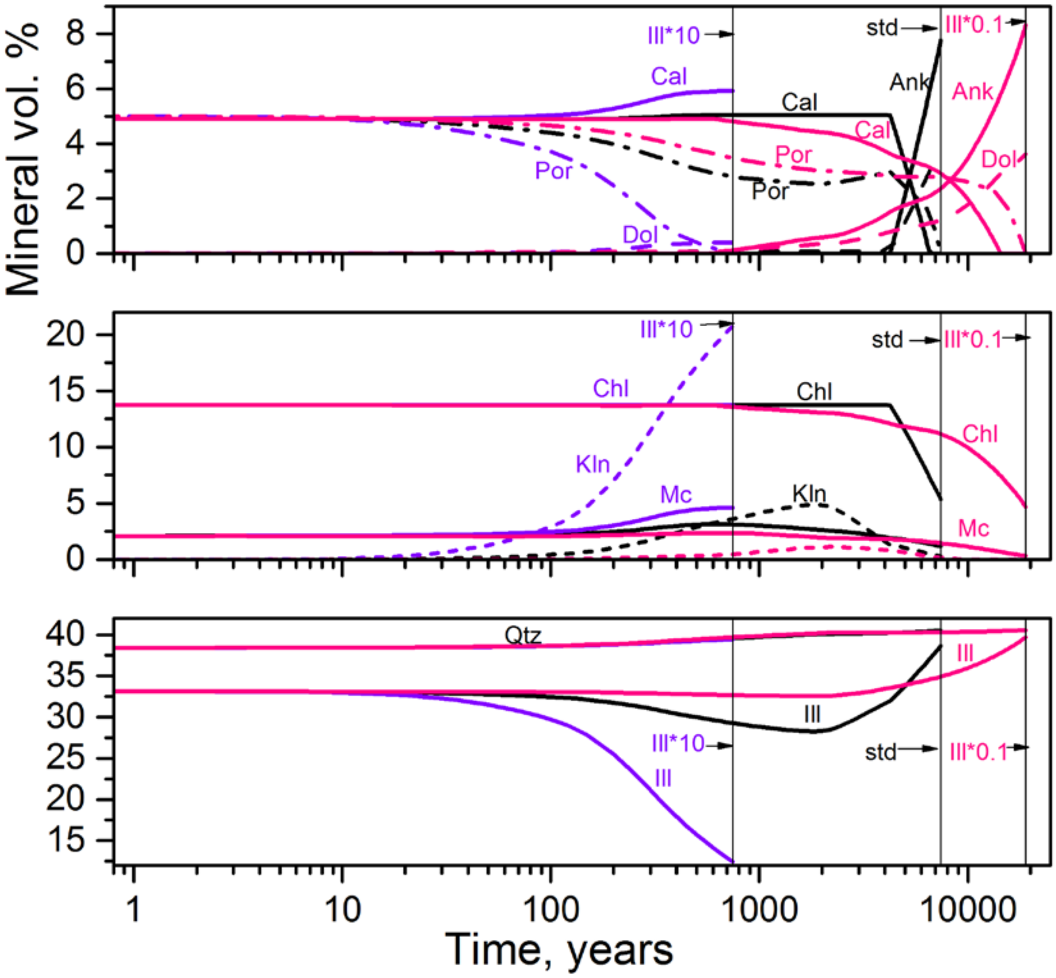

Figure 32: The evolution of mineral volume fractions in shale at the interface of ss/sh for simulations with various values of the illite kinetic constant. Top figure shows calcite precipitation/dissolution (solid line) and precipitation of ankerite (solid) and dolomite (dash) for a value of the illite kinetic constant which is 10 times greater than the standard constant. Also shown are simulations using the standard kinetic constant and an illite kinetic constant which is 10 times less than the standard value. The porosity evolution also is shown (dot dashed lines). Middle figure shows the chlorite dissolution (solid), kaolinite precipitation followed by dissolution (dash), and microcline precipitation/ dissolution (solid). Bottom figure depicts quartz precipitation and illite dissolution/ precipitation (solid).

However, a high illite constant promotes intense kaolinite precipitation in the shale at the interface (Figure 31, middle). This kaolinite precipitation is accompanied by calcite precipitation (Figure 31, top), microcline precipitation (Figure 30, middle), dolomite precipitation (Figure 31, top), and strong illite dissolution (Figure 30, bottom). Overall, the reactive process is described by Reaction 26 in the direction of Kln formation. Porosity is sealed at the interface by Kln precipitation. The pore solution is undersaturated by ankerite.

In contrast, for a low value of the illite kinetic constant (Ill×0.1), ankerite precipitation begins at ~800 years and promotes Reaction 37 (Figure 31, top). After Kln/Ill inversion at ~ 2,000 years this Reaction 37 is replaced by Reaction 27 with illite formation. Compared to the standard case, the rate of reaction is sluggish because of the low illite kinetic constant (Figure 31, bottom).

4.6 DISCUSSION

The second part of this work presented a multicomponent simulation of reaction and diffusion as CO_2 is injected at the ss/sh contact at 75°C and 30 MPa. Initially CO_2 was stored in the sandstone (5 vol. % of sandstone). The initial shale mineral composition contained 15 mass % of Fe-Mg chlorite. In the simulation the shale was modeled as a horizontal layer of 5-m thickness with bottom boundary in contact with the sandstone reservoir and with an upper no-flux boundary. A moderate value of the IAF was chosen, i.e., 7×10^{-3}. With standard values for the mineral reaction kinetic constants, complete porosity infilling occurs at the interface by 7,416 years.

At this time point, the sandstone reservoir is separated from the shale layer by an impermeable shale barrier. From a geoengineering point of view, this means that the sandstone reservoir with shale caprock is a very good storage reservoir for CO_2. This process can be defined as ***auto-sealing*** of the sandstone reservoir by the ss/sh contact. There are two important arguments to support auto-sealing rather than cracking of the caprock. First, porosity closure at the ss/sh interface is controlled by precipitation of carbonates (ankerite and dolomite) and clay minerals (illite, under standard kinetics, or kaolinite). Carbonates and clays are soft minerals that deform under stress by creep (Balashov and Yardley, 1998). Furthermore, second, the reactions here all take place under confined stress at ~ 2 km depth.

The diffusivity of the shale has a large influence on the rate of reaction process at the ss/sh interface. A decrease in the IAF to $(2–4)\times10^{-4}$ leads to a slowdown in the reactive process in the shale and leads to narrowing of the shale reactive zone.

The modeling showed that the minerals taking part in the ss/sh contact interaction are divided in two groups. Namely, minerals which react at local equilibrium—carbonates, chlorite and goethite; and minerals reacting in the kinetic regime—quartz, feldspars and clays. In addition, there are two important time periods in describing the kinetic behavior of kaolinite and illite. During the first period up to ~ 2,000 years, the shale pore solution at the ss/sh interface is supersaturated by Kln and undersaturated by Ill. Thus, Reaction 26 goes from right to left. With time at the ss/sh contact the solution becomes more alkaline and enriched by bicarbonate ion, and after 2,000 years it directs the Reaction 26 from left to right as the shale pore solution becomes supersaturated by illite, and undersaturated by kaolinite. The time of the Kln/Ill inversion was always around of 2,000 years.

For the CO_2 rich geochemical environment Black and Haese (2014) discussed the conflicting reports of whether chlorite inhibits a reactivity of other minerals as low soluble coating on mineral grains (Lu et al., 2012) or accelerates the diagenetic alteration through its replacement by carbonates (Watson et al., 2004; Luquot et al., 2012; Armitage et al., 2013). The results of this reactive modeling showed that both processes might be activated in dependence on the activities of alumina and silica in pore brine. In this study chlorite reacted close to local equilibrium with pore fluid, that was not because of its high kinetic constant (which is moderate one and close to the alkali feldspar constants), but because of it relatively high content and specific surface area in shale. Thus, the “breath” of high activities of alumina and silica from reactions in sandstone corresponded to low ferrous iron activity. Therefore, pore brine was undersaturated by ankerite. In this case chlorite demonstrated very inert behavior. In the opposite way, the low activities of alumina and silica led to increased ferrous iron activity in the pore brine and triggered chlorite carbonation (12–13).

The reactive processes at the ss/sh contact were most sensitive to the kinetic constants of kaolinite and illite. With a high value of the kaolinite kinetic constant (Kln×10), the sandstone reservoir auto-sealed within 107 years because of the chlorite carbonation Reaction 37. In contrast, a high illite kinetic constant (Ill×10) produces auto-sealing at 740 years due to intensive kaolinite precipitation in accordance with Reaction 26. Kln and Ill demonstrate kinetically coupled behavior: the increase in the kinetic constant of one of the minerals brings that mineral closer to equilibrium, simultaneously moving the other mineral away from equilibrium.

5. CONCLUSIONS

To build confidence in the ability to predict the mechanisms and rates of CO_2 sequestration in the subsurface, models of mineral-brine-CO_2 reactions are needed. Running such models requires kinetic and thermodynamic databases as well as data for reservoirs and formation fluids. Many reactive transport models are available and several researchers have modeled individual systems. To understand and evaluate the models, in the first part of this work a baseline sandstone reservoir is proposed that can be modeled by any such reactive transport code. If many researchers model CO_2 interactions for this baseline model, this would allow systematic comparisons between models in order to learn what behaviors are well-predicted or which behaviors are model-dependent. Furthermore, by focusing on reaction + diffusion (without advection), the important effects, if any, of the kinetics of mineral reaction can be isolated.

In the model, 97% of the maximum CO_2 sequestration, 34.5 kg CO_2 per m^3 of sandstone, is attained by 4,000 a even though the system does not achieve chemical equilibrium until ~25,000 a. The maximum represents about 20% CO_2 dissolved as $CO_{2(aq)}$, 50% dissolved as HCO_3^-, and 30% precipitated as calcite: 70% solubility trapping versus 30% mineral trapping. The extent of sequestration as HCO_3^- at equilibrium can be calculated from equilibrium thermodynamics without reactive transport modeling because it is mainly determined by the amount of Na^+ in the initial sandstone in a soluble mineral (here, oligoclase); in contrast, the extent of trapping into calcite is determined by the initial content of a soluble Ca-containing silicate (here, oligoclase + smectite). This powerful observation may be generally true for most lithologies and should be explored in other simulations for other systems.

The sensitivity studies reported here are consistent with the conclusion that variations in reaction rates mostly affect storage-reservoir behavior in the 10–1,000 a time frame. Although the modeling did not include advection, these conclusions about the importance of kinetics from 10–10,000 a should also be true for systems that include advection + diffusion because kinetic limitation should be even more important in advective systems.

The reactive diffusion modeling revealed that the kinetics of oligoclase, albite, and smectite are all significant for sequestration in the sandstone reservoir and thus are phases that should be considered for any second-generation models of CO_2 storage. The modeling furthermore demonstrates that the behavior of all components is interconnected. Therefore, predicting exact timescales for CO_2 trapping will not be possible given the impossibility of fully constraining all heterogeneities and mineral distributions in the subsurface. However, general observations about mineral behaviors should be possible.

In the second part of work, reactive transport at the contact of the CO_2 storage reservoir—i.e., the (sandstone)/caprock (shale) interface—has shown a high sensitivity to the kinetic constants of the clay minerals (kaolinite and illite) and to the shale transport properties. Chlorite plays a key major role in the development of the reactive zone in the shale. In most cases chlorite carbonation with formation of ankerite, dolomite, and illite (kaolinite) leads to autosealing of the ss/sh contact. An increase in the kinetic constants of the clay minerals results in a remarkable decrease in the autosealing times (a decrease of these constants works in the opposite way). A decrease in the shale diffusivity causes contraction of the shale reactive zone and an increase in the autosealing times.

This page intentionally left blank.

6. REFERENCES

Adabi, M. H.; Rao, P. Major and Minor Elements and their Relationship to Gold Mineralization, Beaconsfield Mine, Tasmania, Australia. *Iranian Int. J. Sci* **2003,** *4*, 37–56.

Archie, G. E. The electrical resistivity log as an aid in determining some reservoir characteristics. *Transactions of the American Institute of Mechanical Engineers* **1942,** *146*, 54–67.

Armitage, P. J.; Faulkner, D. R.; Worden, R. H. Caprock Corrosion. *Nat. Geosci.* **2013,** *6*, 79-80.

Arvidson, R. S.; Lüttge, A. Mineral Dissolution Kinetics as a Function of Distance from Equilibrium - New Experimental Results. *Chemical Geology* **2010,** *269*, 79–88.

Balashov, V. N.; Guthrie, G. D.; Lopano, C. L.; Hakala, J. A.; Brantley, S. L. Reaction and diffusion at the reservoir/ shale interface during CO_2 storage: impact of geochemical kinetics. *Applied Geochemistry* **2015,** *61*, 119–131.

Balashov, V. N.; Guthrie, G. D.; Hakala, J. A.; Lopano, C. L.; Rimstidt, J. D.; Brantley, S. L. Predictive modeling of CO_2 sequestration in deep saline sandstone reservoirs: Impacts of geochemical kinetics. *Applied Geochemistry* **2013,** *30*, 41–56.

Balashov, V. N.; Lebedeva, M. I., Macrokinetic Model of Origin and Development of a Monomineralic Bimetasomatic Zone, Ch. 8. In *Progress in Metamorphic and Magmatic Petrology, A memorial volume in honor of D.S.Korzhinskii*; Perchuk, L. L., Ed.; Cambridge University Press: Cambridge, 1991; pp 167–195.

Balashov, V. N.; Lebedeva, M. I. On Transition to Local Equilibrium during Development of Diffusion Bimetasomatic Zone. *Doklady Akad. Nauk SSSR* **1989,** *307*, 703–707.

Balashov, V. N.; Yardley, B. W. D. Modeling metamorphic fluid flow with reaction-compaction-permeability feedbacks. *American Journal of Science* **1998,** *298*, 441–470.

Balashov, V. N.; Zaraisky, G. P. Experimental and Theoretical Investigation of Decompaction of Rocks during Heating. In *Outlines of Physico-Chemical Petrology*; Nauka: Moscow, 1982; 10, pp 69–109.

Benson, S.; Cook, P. *Chapter 5: Undeground geological storage. IPCC Special Report on Carbon dioxide Capture and Storage;* Metz, B., et al. Eds.; Cambridge, U.K., 2005; pp 195–276.

Berne, P.; Bachaud, P.; Fleury, M. Duiffusion Properties of Carbonated Caprocks from the Paris Basin. *Oil & Gas Science and Technology* **2010,** *65*, 473–484.

Black, J. R.; Haese, R. R. Chlorite Dissolution rates under CO_2 saturated conditions from 50 to 120°C and 120 to 200 bar CO_2. *Geochimica et Cosmochimica Acta* **2014,** *125*, 225–240.

Blum, L.; Høye, J. S. Mean Spherical Model for Asymmetric Electrolytes. 2. Thermodynamic Properties and the Pair Correlation Function. *J. Phys. Chem. B* **1977,** *81*, 1311–1316.

Brace, W. F. Permeability from resistivity and pore shape. *Journal of Geopysical Research* **1977,** *82*, 3343–3349.

Brantley, S. L. Kinetics of Mineral Dissolution. In *Kinetics of water-rock interaction*; Brantley, S. L., Kubicki, J. D., White, A. F., Eds.; Springer, 2008; pp 151–210.

Brenan, K. E.; Campbell, S. L.; Petzold, L. R. *Numerical Solution of Initial-Value Problems in Differential- Algebraic Equations*. SIAM Press: Philadelphia, PA, 1995.

Chermak, J. A.; Rimstidt, J. D. Estimating the free energy of formation of silicate minerals at high temperatures from the sum of polyhedral contributions. *American Mineralogist* **1990a,** *75*, 1376–1380.

Chermak, J. A.; Rimstidt, J. D. Estimating the thermodynamic properties of silicate minerals at 298 K from the sum of polyhedral contributions. *American Mineralogist* **1989,** *74*, 1023–1031.

Chermak, J. A.; Rimstidt, J. D. Hydrothermal transformation rate of kaolinite to muscovite/illite. *Geochimica et Cosmochimica Acta* **1990b,** *54*, 2979–2990.

Collins, A. G. *Geohemistry of Oilfield Waters;* Elsevier: Amsterdam, 1975.

Dentz, M.; Tartakovsky, D. M. Abrupt-Interface Solution for Carbon Dioxide Injection into Porous Media. *Transp Porous Med* **2009,** *79*, 15–27.

Dickinson, W. R.; Suczek, C. A. Plate tectonics and sandstone compositions. *American Association of Petroleum Geologists Bulletin* **1979,** *63*, 2164–2182.

Doughty, C. Investigation of CO_2 Plume Behavior for a Large-Scale Pilot Test of Geologic Carbon Storage in a Saline Formation. *Transp. Porous Med.* **2010,** *82*, 49–76.

Duan, Z.; Sun, R. An improved model calculating CO2 solubility in pure water and aqueous NaCl solutions from 273 to 533 K and from 0 to 2000 bar. *Chemical Geology* **2003,** *193*, 257–271.

Ennis-King, J.; Paterson, L. Coupling of geochemical reactions and convective mixing in the long-term geological storage of carbon dioxide. *International Journal of Greenhouse Gas Control* **2007,** *1*, 86–93.

Ferry, J. M.; Stubbs, J. E.; Guan, Y.; Eiler, J. M. Ultrastep composition gradients within ankerite grains from regionally metamorphosed marls. *Geochimica et Cosmochimica Acta* **2009,** *73*, A372–A372.

Fleury, M.; Berne, P.; Bachaud, P. Diffusion of Dissolved CO_2 in Caprock. *Energy Procedia* **2009,** *1*, 3461–3468.

Gaus, I.; Azaroual, M.; Czernichowski-Lauriol, I. Reactive transport modelling of the impact of CO_2 injection on the clayey cap rock at Sleipner (North Sea). *Chemical Geology* **2005,** *217*, 319–337.

Godderis, Y.; Williams, J. Z.; Schott, J.; Pollard, D.; Brantley, S. L. Time evolution of the mineralogical composition of Mississippi Valley loess over the last 10 kyr: Climate and geochemical modeling. *Geochimica et Cosmochimica Acta* **2010,** *74*, 6357–6374.

Helgeson, H. C.; Kirkham, D. H.; Flowers, G. C. Theoretical prediction of the thermodynamic behavior of aqueous electrolytes at high pressures and temperatures: IV. Calculations of activity coefficients, osmotic coefficients, and apparent standard and relative partial molal properties to 600°C and 5 kb. *American Journal of Science* **1981,** *281*, 1249–1516.

Hnedkovsky, L.; Wood, R. H.; Balashov, V. N. Electrical Conductances of Aqueous Na_2SO_4, H_2SO_4, and their Mixtures: Limiting Equivalent Ion Conductances, Dissociation

Constants, and Speciation to 673 K and 28 MPa. *J. Phys. Chem. B* **2005,** *109*, 9034–9046.

Holland, T. J. B.; Powell, R. An improved and extended internally consistent thermodynamic dataset for phases of petrological interest, involving a new equation of state for solids. *Journal of Metamorphic Geology* **2011,** *29*, 333–383.

Holland, T. J. B.; Powell, R. An internally consistent thermodynamic data set for phases of petrological interest. *Journal of Metamorphic Geology* **1998,** *16*, 309–343.

Holland, T.; Powell, R. Plagioclase feldspars: Activity-Composition relations based upon Darken's quadratic formalism and Landau theory. *American Mineralogist* **1992**, 77, 53-61.

Hosterman, J. W.; Whitlow, S. I. *Clay Mineralogy of Devonian Shales in the Appalachian Basin*; Geological Survey Professional Paper 1298; U.S. Government Printing Office: Washington, DC, 1983; pp 1–31.

Johnson, J. W.; Oelkers, E. H.; Helgeson, H. C. SUPCRT92: A software package for calculating the standard molal thermodynamic properties of minerals, gases, aqueous species, and reactions from 1 to 5000 bar and 0 to 1000 °C. *Comp. Geoscience* **1992,** *18*, 899–947.

Kang, Q.; Lichtner, P. C.; Viswanathan, H. S.; Abdel-Fattah, A. I. Pore Scale Modeling of Reactive Transport Involved in Geologic CO_2 Sequestration. *Transp Porous Med* **2010,** *82*, 197–213.

Kaszuba, J. P.; Viswanathan, H. S.; Carey, J. W. Relative stability and significance of dawsonite and aluminum minerals in geologic carbon sequestration. *Geophysical Research Letters* **2011,** *38*, L08404.

Köhler, S. J.; Dufaud, F.; Oelkers, E. H., An experimental study of illite dissolution kinetics as a function of pH from 1.4 to 12.4 and temperature from 5 to 50°C. *Geochimica et Cosmochimica Acta* **2003,** *67*, 3583–3594.

Korzhinskii, D. S. Mobility and inertness of components in metasomatosis. *Izv. Acad. Nauk SSSR, Ser. Geol.* **1936,** 1, 58–60.

Korzhinskii, D. S. *Theory of Metasomatic Zoning*; Clarendon Press, 1970.

Kostelnik, J.; Carter, K. M. Unraveling the stratigraphy of the Oriskany Sandstone: A necessity in assessing its site-specific carbon sequestration potential. *Environmental Geosciences* **2009,** *16*, 187–200.

Lebedeva, M. I.; Fletcher, R. C.; Balashov, V. N.; Brantley, S. L. A reactive diffusion model describing transformation of bedrock to saprolite. *Chemical Geology* **2007,** *244*, 624–645.

Lebedeva, M. I.; Vlachos, D. G.; Tsapatsis, M. Bifurcation Analysis of Liesegang Ring Pattern Formation. *Physical Review Letters* **2004,** *92*, 088301-1–088301-4.

Li, L.; Peters, C. A.; Celia, M. A. Applicability of Averaged Concentrations in Determining Geochemical Reaction Rates in Heterogeneous Porous Media. *American Journal of Science* **2007,** *307*, 1146–1166.

Lichtner, P. C. Continuum Formulation of Multicomponent - Multiphase Reactive Transport. In *Reactive Transport in Porous Media, Reviews in Mineralogy, vol. 34*; Lichtner, P. C.; Steefel, C. I.; Oelkers, E. H., Eds. Mineralogical Society of America, 1996; 34, p 1–81.

Lichtner, P. C. Scaling Properties of Time-Space Mass Transport Equations and the Local Equilibrium Limit. *American Journal of Science* **1993,** *293*, 257–296.

Lichtner, P. C.; Pabalan, R. T.; Steefel, C. I., Model Calculations of Porosity Reduction Resulting from Cement-Tuff Diffusive Interaction. In *Scientific Basis for Nuclear Waste Management XXI Book Series: Materials Research Society Symposium Proceedings;* McKinley, I. G., McCombie, C., Eds.; 1998; Vol. 506, pp 709–718.

Liu, Y.; Wang, L.; Yu, B. Sharp Front Capturing Method for Carbon Dioxide Plume Propagation during Injection into a Deep Confined Aquifer. *Energy Fuels* **2010,** *24*, 1431–1440.

Lowson, R. T.; Brown, P. L.; Comarmond, M.-C. J.; Rajaratnam, G. The Kinetics of Chlorite Dissolution. *Geochimica et Cosmochimica Acta* **2007,** *71*, 1431–1447.

Lowson, R. T.; Comarmond, M.-C. J.; Pajaratnam, G.; Brown, P. L. The Kinetics of the Dissolution of Chlorite as a Function of pH and at 25°C. *Geochimica et Cosmochimica Acta* **2005,** *69*, 1687–1699.

Lu, C.; Lee, S.-Y.; Han, W. S.; McPherson, B. J.; Lichtner, P. C. Comments on “Abrupt-Interface Solution for Carbon dioxide Injection into Porous Media” by M. Dentz and D. Tartakovsky. *Transp Porous Med* **2009,** *79*, 29–37.

Lu, J.; Kharaka, Y. K.; Thordsen, J. J.; Horita, J.; Karamalidis, A.; Griffith, C.; Hakala, J. A.; Ambats, G.; Cole, D. R.; Phelps, T. J.; Manning, M. A.; Cook, P. J.; Hovorka, S. D. CO_2-Rock-Brine interactions in Lower Tuscaloosa Formation *Chemical Geology* **2012,** *291*, 269–277.

Luquot, L.; Andreani, M.; Gouze, P.; Camps, P. CO_2 Percolation Experiment through Chlorite/Zeolite-rich Sandstone (Pretty Hill Formation - Otway Basin - Australia). *Chemical Geology* **2012,** *294–295*, 75–78.

Lüttge, A.; Arvidson, R. S.; Fisher, C. A Stochastic Treatment of Crystal Dissolution Kinetics. *Elements* **2013,** *9*, 183–188.

Marcus, Y. *Ion Solvation*; Wiley, 1985.

Marini, L. Geological Sequestration of Carbon Dioxide. In *Developments in Geochemistry 11*; Elsevier: Amsterdam, 2007.

McKibben, M. A.; Barnes, H. L. Oxidation of Pyrite in Low Temperature Acid Solutions: Rate Laws and Surface Textures. *Geochimica et Cosmochimica Acta* **1986,** *50*, 1509–1520.

Milliken, K. Petrography of Ankerite Cement, Grain Replacement, and Fracture Fill in Foreland Sandstones of the Central Rocky Mountains, March 10-13. In *AAPG Annual Meeting*, AAPG Search and Discovery Article #90007 2002: Houston, TX, 2002.

Na, L.; Li, L.; Xiyu, Q.; Huidong, Y.; Lijuan, W.; Shuang, Z. Genesis of authigene carbonate minerals in the Upper Cretaceous reservoir, Honggang Anticline, Songliao Basin: A natural analog for mineral trapping of natural CO_2 storage. *Sedimentary Geology* **2011,** *237*, 166–178.

NETL ATLAS, *Carbon Sequestration Atlas of the United States and Canada*, 3rd ed.; U.S. Department of Energy, National Energy Technology Laboratory, 2010.

Odom, I. E. Nature of feldspar-grain size relations in some quartz-rick sandstones. *Journal of Sedimentary Petrology* **1976,** *46*, 862–870.

Oelkers, E. H.; Helgeson, H. C. *Geochimica et Cosmochimica Acta* **1990,** *54*, 727–738.

Palandri, J. L.; Kharaka, Y. K. *A compilation of rate parameters of water-mineral interaction kinetics for application to geochemical modeling*; Open File Report 2004-1068; U.S. Geological Survey: Menlo Park, CA, 2004.

Pettijohn, F. J., Potter, P. E., Siever, R. *Sand and Sandstone;* Springer-Verlag: NY, 1987.

Petzold, L. R. A description of DASSL: A differential/algebraic system solver. In *IMACS Trans. on Scientific Computation, v.1*; Stepleman, R. S., Ed.; 1982; Vol. 1.

Pham, V. T. H.; Lu, P.; Aagaard, P.; Zhu, C.; Hellevang, H. On the potential of CO_2–water–rock interactions for CO_2 storage using a modified kinetic model. *International Journal of Greenhouse Gas Control* **2011,** *5*, 1002–1015.

Pokrovskii, V. A.; Helgeson, H. C. Thermodynamic properties of aqueous species and the solubilities of minerals at high pressures and temperatures: the system Al_2O_3-H_2O-NaCl. *American Journal of Science* **1995,** *295*, 1255–1342.

Rimstidt, J. D.; Brantley, S. L.; Olsen, A. A. Systematic Review of Forsterite Dissolution Rate Data. *Geochimica et Cosmochimica Acta* **2012,** *99*, 159–178.

Rimstidt, J. D.; Newcomb, W. D. Measurement and Analysis of Rate Data: The Rate of Reaction of Ferric Iron with Pyrite. *Geochimica et Cosmochimica Acta* **1993,** *57*, 1919–1934.

Rockström, J.; Steffen, W.; Noone, K.; Persson, A.; Chapin, III, F. S.; Lambin, E. F.; Lenton, T. M.; Scheffer, M.; Folke, C.; Schellnhuber, H. J.; Nykvist, B.; de Wit, C. A.; Hughes, T.; van der Leeuw, S.; Rodhe, H.; Sörlin, S.; Snyder, P. K.; Costanza, R.; Svedin, U.; Falkenmark, M.; Karlberg, L.; Corell, R. W.; Fabry, V. J.; Hansen, J.; Walker, B.; Liverman, D.; Richardson, K.; Crutzen, P.; Foley, J. A. A safe operating space for humanity. *Nature* **2009,** *461*, 472–475.

Sengers, J. V.; Watson, J. T. R. Improved international formulations for the viscosity and thermal conductivity of water substance. *J. Phys. Chem. Ref. Data* **1986,** *15*, 1291–1314.

Sharygin, A. V.; Grafton, B. K.; Xiao, C.; Wood, R. H.; Balashov, V. N. Dissociation constants and speciation in aqueous Li_2SO_4 and K_2SO_4 from measurements of electrical conductance to 673 K and 29 MPa. *Geochimica et Cosmochimica Acta* **2006,** *70*, 5169–5182.

Sharygin, A. V.; Wood, R. H.; Zimmerman, G. H.; Balashov, V. N. Multiple Ion Association versus Redissociation in Aqueous NaCl and KCl at High Temperatures. *J. Phys. Chem. B* **2002,** *106*, 7121–7134.

Shindo, Y.; Fujioka, Y.; Takeuchi, K.; Komiyama, H. Kinetics on the dissolution of CO_2 into water from the surface of CO_2 hydrate at high pressure. *Int. J. Chem. Kinet.* **1995,** *27*, 569–575.

Stauffer, P. H.; Viswanathan, H. S.; Pawar, R. J.; Guthrie, G. D. A system model for geologic sequestration of carbon dioxide. *Environmental Science and Technology* **2009,** *43*, 565–570.

Steefel, C. I.; Lichtner, P. C. Diffusion and Reaction in Rock Matrix Bordering a Hyperalkaline Fluid-Filled Fracture. *Geochimica et Cosmochimica Acta* **1994,** *58*, 3595–3612.

Steefel, C. I.; VanCappellen, P. A New Kinetic Approach to Modeling Water-Rock Interaction - the Role of Nucleation, Precursors, and Ostwald Ripening. *Geochimica et Cosmochimica Acta* **1990,** *54*, 2657–2677.

Szulczewski, M. L.; MacMinn, C. W.; Herzog, H. J.; Juanes, R. Lifetime of carbon capture and storage as a climate-change mitigation technology. *PNAS* **2012,** *109*, 5185–5189.

Thompson, J. B., Jr. Geochemical reaction and open systems. *Geochimica et Cosmochimica Acta* **1970,** *34*, 529–551.

Trevena, A. S.; Nash, W. P., Chemistry and provenance of detrital plagioclase. *Geology* **1979,** ***7***, 475–478.

Wagner, W.; Pruss, A. The IAPWS formulation 1995 for the thermodynamic properties of ordinary water substance for general and scientific use. *J. Phys. Chem. Ref. Data* **2002,** *31,* 387.

Watson, M.; Boreham, C. J.; Tingate, P. R. Carbon Dioxide and Carbonate Cements in the Otway basin: Implications for Geological Storage of Carbon Dioxide. *APPEA J.* **2004,** *44*, 703–720.

White, A. F.; Brantley, S. L. The Effect of Time on the Weathering of Silicate Minerals: Why Do weathering Rates Differ in the Laboratory and Field? *Chemical Geology* **2003,** 202, 479–506.

Wildgust, N.; Gorecki, C. D.; Bremer, J. M. An overview of the IEA Greenhouse Gas R&D Programme regional geologic storage capacity studies. *Energy Procedia* **2011,** 4, 4835-4840.

Williamson, M. A.; Rimstidt, J. D. The Kinetics and Electrochemical Rate-Determining Step of Aqueous Pyrite Oxidation. *Geochimica et Cosmochimica Acta* **1994,** *58*, 5443–5454.

Zaraisky, G. P.; Balashov, V. N. Thermal decompaction of rocks, Ch. 10. In *Fluids in Crust: Equilibrium and Transport Properties*, Shmulovich, K. I., Yardley, B. W. D., Gonchar, G.G., Eds.; Chapman & Hall: London, 1995; pp 253–284.

Zaraisky, G. P.; Balashov, V. N.; Lebedeva, M. I. Macrokinetic Model of Metasomatic Zoning. *Geokhimiya* **1989,** 10, 1386–1395.

Zaraisky, G. P.; Zharikov, V. A.; Stoyanovskaya, F. M.; Balashov, V. N. *Experimental Investigation of Bimetasomatic Skarn Formation*; Nauka: Moscow, 1986; p 232.

Sean Plasynski
Executive Director
Technology Development & Integration Center
National Energy Technology Laboratory
U.S. Department of Energy

John Wimer
Associate Director
Strategic Planning
Science & Technology Strategic Plans & Programs
National Energy Technology Laboratory
U.S. Department of Energy

Traci Rodosta
Strategic Planning
Science & Technology Strategic Plans & Programs
National Energy Technology Laboratory
U.S. Department of Energy

Mark Ackiewicz
Director
Division of Carbon Capture and Storage
Office of Fossil Energy
U.S. Department of Energy

Cynthia Powell
Executive Director
Research & Innovation Center
National Energy Technology Laboratory
U.S. Department of Energy

NETL Technical Report Series